Investigation on high temperature deformation mechanism and strengthening of V-4Cr-4Ti alloys

ZHENG PENGFEI

DOCTOR OF PHILOSOPHY

Department of Fusion Science
School of Physical Sciences
The Graduate University for Advanced Studies

2012

ABSTRACT

Strengthening mechanisms already developed for steels and other alloys, such as work hardening, precipitation hardening, nanoparticle dispersion strengthening and grain refining strengthening have been examined for low activation V－4Cr－4Ti alloy in the present study. It is revealed that work hardening followed by precipitation hardening is more effective than work hardening after precipitation hardening to improve the creep resistance at high stress. Nanoparticle dispersion strengthening is very effective to strengthen the alloy. Grain size refining enhances the hardness and tensile strength, however does not improve the creep property. The guiding principle for improvement of creep strength was obtained, based on the control of microstructures.

Research of structural materials for blanket is an important part in the fusion research area. Recently, low activation V－4Cr－4Ti alloy has been identified as an attractive candidate for self－cooled liquid lithium blanket to be operated at around 700℃ in fusion reactors. In order to obtain improved energy conversion efficiency by higher temperature operation, the V－4Cr－4Ti alloy needs to be strengthened further. For purpose of effective strengthening, the high temperature deformation mechanism of the V－4Cr－4Ti alloy needs to be investigated.

In the present study, the starting idea for strengthening V－4Cr－4Ti alloy is to increase its yield stress for resisting the dislocation motion and thus resists the deformation of the material. Various strengthening mechanisms have been introduced for combinations aiming to get improved high temperature strength. (1) Work hardening combined with precipitation hardening and (2) nanoparticle dispersion strengthening coupled with grain size refining are the two sets of combined strengthening methods in the present study. The combination (1) is applied on the reference V－4Cr－4Ti alloy plate, NIFS－HEAT－2, using thermo－mechanical treatments (TMT). The combination (2) has been carried out by fabricating a new V－4Cr－4Ti alloy via mechanical alloying (MA). In the MA process, Y is introduced as a scavenger for gaseous impurities. TiC, SiC and Ti_3SiC_2 are used as dispersion particles.

For the combination of work hardening with precipitation hardening, the order of work hardening after precipitation hardening is designated as SAACW, and the order of work hardening followed by precipitation hardening is designated as SACWA. A standard heat treatment, STD, is introduced as the reference. Mechanical test results show that work hardening combined with precipitation hardening in either order can lead to remarkable increase in yield

stress of the V-4Cr-4Ti alloy (NIFS-HEAT-2) at room temperature (RT), 700°C and 750°C. However, they are different in creep behavior. SAACW behaves similar to STD, while SACWA are different from them. The creep rate of SACWA at the stress < 180MPa is higher than that of SAACW and STD. In contrast, at the stresses > 180MPa, SACWA has lower creep rate than that of SAACW and STD. Creep activation energy indicates that SACWA has a dislocation climbing creep mechanism in the whole testing stress region. SAACW and STD share the dislocation climbing creep mechanism mainly at stresses <180MPa, then turns to dislocation-glide creep mechanism at stresses >180MPa. Microstructural analysis shows that dislocations in SAACW and STD after creep deformation are of a/2<111> type, while crept SACWA owns higher number density of dislocations not only in a/2<111> type but also possibly in a<100> type which was introduced by the prior cold working.

It is considered that a<100> type dislocations in SAACW are not strongly decorated by the precipitates, because the dislocations were introduced after the precipitation, so that they mostly disappeared soon after the creep deformation starts. In contrast, SACWA has precipitates distributing along the dislocations introduced by the prior cold working, because those dislocations supply the precipitation sites. The pinning is considerably strong to resist the coarsening of precipitates as well as to possibly resist the decrease in a<100> type dislocation density. Accordingly, the special pinning draws a resisting capability over the threshold stress for dislocation glide. As a result, SACWA keeps dislocation climbing throughout the examined stresses.

SACWA and STD have also been evaluated in Li exposure. The present study uses static liquid lithium at 650°C for about 250hrs exposure.

The stabilization of precipitates by dislocations in SACWA sustains in this Li exposure. Both SACWA and STD have been strengthened by the Li exposure due to trapping of impurities, such as C and N from liquid Li. On the other hand, O transfer from V matrix to Li causes softening to the alloy. Such mass transfers are due to the chemical affinity of those impurities for lithium competing with V, Cr and Ti. It is evident that the hardened ranges were equivalent to the diffusion ranges for C and N. The strengthening due to C and especially N mass transfers can decrease the creep rate of V-4Cr-4Ti alloy, because of the increased number density of precipitates. However, the contaminations are considered to just have the capability of inducing limited hardening range near the surface area of a blanket wall. The diffusion range of N, for example, at 100,000 hr is estimated as 1.55 mm, smaller than the typical blanket wall thickness which is 5mm.

The second combination of nanoparticle dispersion strengthening with grain size refining via MA has been successfully achieved. The present study, for the first time, performed MA for the candidate V-4Cr-4Ti system. The strengthening is found to increase with increasing

MA time. After the parametric survey, 40hrs is determined as the minimum process time required for MA of V – 4Cr – 4Ti alloy with Y and TiC additions. This is mainly determined by the dissolution of Ti. In the MA process study, it is found that the dissolution of Y into the V matrix is faster than that of Cr, and the dissolution of Cr is faster than that of Ti. Different dissolution capability is also found for the carbides. In detail, TiC behaves similarly to SiC. They dissolve faster than Ti_3SiC_2 into the V matrix.

Hardness and tensile strength have been increased by the long time MA, because of the more complete solid solution hardening, improved nanoparticle dispersion strengthening, and enhanced grain size refining. Transmission electron microscope (TEM) observation shows that the V – 4Cr – 4Ti alloy has obtained high density of TiN and Y_2O_3 nanoparticles. These two species of nanoparticles are considered as the main strengthening agents in improving the nanoparticle dispersion strengthening. An annealing at 1200°C for 1hr reveals that the Y_2O_3 owns higher thermal stability than TiN. The grain size of mechanically alloyed V – 4Cr – 4Ti – 1.5Y – 0.3TiC alloy is 0.37 μm after annealing, which is much smaller than that of NIFS – HEAT – 2 in STD state (17.8 μm). These ultra fine grains can account for the strengthening due to grain size refining.

The refined grains generally degrade the creep resistance due to the grain boundary sliding creep. The creep resistance of the mechanically alloyed V – 4Cr – 4Ti – 1.5Y – 0.3TiC alloy is degraded under 280MPa compared with that of NIFS – HEAT – 2 in either STD or SACWA state. It is thought that the creep deformation under this stress region is dominated by grain boundary sliding. On the other hand, in creep test at 100MPa, the creep resistance of the mechanically alloyed V – 4Cr – 4Ti – 1.5Y – 0.3TiC alloy is higher than or at least equal to that of NIFS – HEAT – 2 in both SACWA and STD states. It is considered that the high number density of nanoparticles in grain interior effectively resisted the dislocation motion under 100MPa.

Based on the above discussions, the stabilization of precipitates by dislocations in SACWA is considered to be the reason of enhancing the resistance against dislocation glide creep at stress above 180MPa. While, these dislocations in SACWA also increases the dislocation climbing creep under lower stress as 100MPa which is assumed as the design stress for blanket structure. Therefore, more introductions of precipitates without high density of dislocations would be desirable. In the case of strengthening V – 4Cr – 4Ti alloy via MA, the collisions between the alloy powder and milling balls caused the dissolutions of alloying elements and carbides for solid solution hardening along with nanoparticle dispersion strengthening, and also caused refined grains. These refined grains can lead grain boundary sliding creep to the alloy and degrade its creep resistance under high stress. In such situation, high number density of thermally stable nanoparticles without the coexistence of refined grains would be favored.

In conclusion, the present study has successfully strengthened the V－4Cr－4Ti alloy with various mechanisms. Creep resistance has been enhanced by combined strengthening. A guiding principle for strengthening V－4Cr－4Ti alloy aiming to high temperature application has been obtained. This principle is to introduce high number density of precipitates/nanoparticles as well as low number density of dislocations and less grain boundaries.

Table of Contents

CHAPTER 1
Introduction

1.1 History and Status of Worldwide Energy Exhaustion

As human society develops, energy consumption increases. From the time of the first industrial revolution, it has been possible to relate energy consumption to economic growth [1]. Power generation, metallurgy, and lighting initially required the highest percentage of energy consumption. Robust energy conservation technologies were developed to increase energy efficiency; however, the developing industrial scale increased energy demands. Figure 1-1 plots the worldwide energy consumption from 1850 to 2005 [2]. Energy consumption clearly increased sharply in the past 60 years, and this trend is expected to continue. According to the United States Energy Information Administration, world energy consumption in all of forms is projected to reach 7.15×10^{20}J (i.e., 1.7×10^{10} tons of oil) by 2030 [3], which is a 44% increase over the current amount.

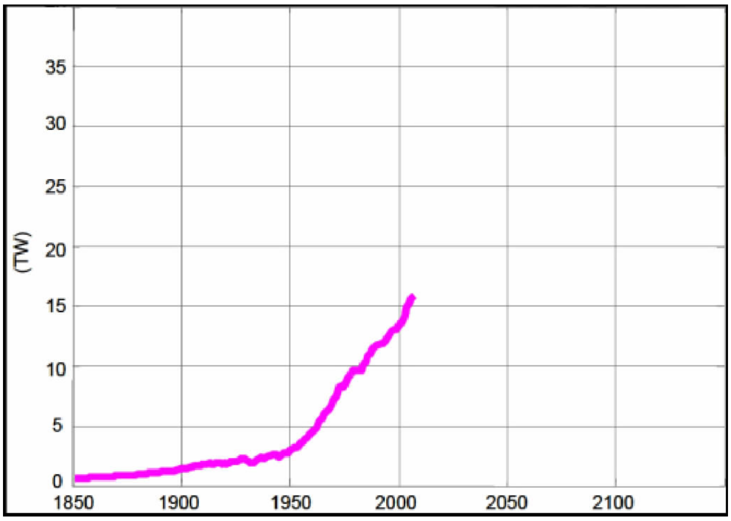

Fig. 1-1 Worldwide energy consumption from 1850 to 2005 [2]

Of all forms of energy, fossil fuels (e.g., gas, oil, and coal) are the most used. Currently, most fuels are consumed in electricity production, engine power production, and heat production, with electricity occupying more than half of the energy consumption. Figure 1-2 indicates the energy structure of electricity production in 2010 [4]. Fossil fuels together account for 68% of electricity production, and almost all engine power and heat production use fossil fuels.

However, fossil fuels are unrenewable resources. Renewable energy sources provide 18% of all energy production, with hydro accounting for 15% and other sources accounting for 3%. The current source of nuclear energy, fission power, can also be considered unrenewable, although some ^{239}Pu can be bred by nuclear transformation from ^{238}U.

Figure 1-3 estimates the remaining times of the four main unrenewable energy reserves available worldwide at the present energy consumption rate [5]. The most pessimistic estimation is 76 years. Therefore, an energy crisis will occur in the near future, and new forms of energy will be necessary to maintain industrial development and economic growth. Wide use of renewable energy sources seems to be a solution; however, this solution is based on a disregard for cost.

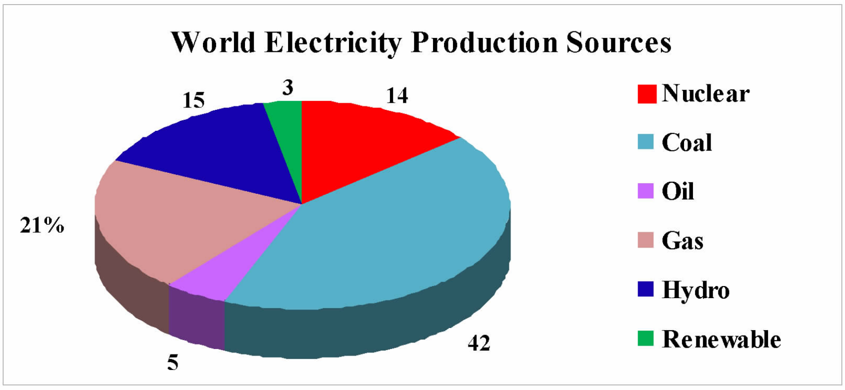

Fig. 1-2 Energy structure of the world in 2010 [4]

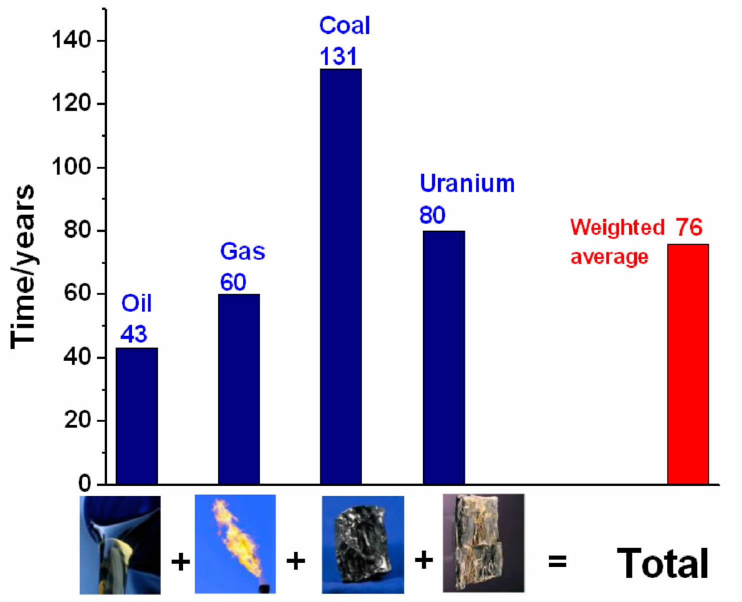

Fig. 1-3 Estimated remaining time for fossil fuels (including oil, gas, and coal) and uranium reserves available worldwide at the present energy consumption rate [5]

In reality, wide use of the present renewable energy sources is not reasonable because the low energy density of these sources can hardly be increased or it requires a large area to provide the energy consumed. According to ref. [6], the land requirement of conventional power plants is modest, in the range of 200 to 1000m^2/MW. In contrast, most renewable energy sources have land requirements of 4,000 to 90,000m^2/MW. One report [5] indicated that wind energy and solar energy have such low energy densities that the land needed by wind is 60,000km^2 and that needed by solar energy is 20,000km^2 to match annual nuclear energy production, not including the instability of weather. Thus, other forms of renewable energy requiring less land are preferable.

1.2 Status of Nuclear Energy

The ideal solution for the upcoming energy crisis is another form of nuclear energy, controlled fusion energy. Controlled fusion is similar to conventional electricity sources. Because the land requirement is roughly $300 m^2/MW$ [7], controlled fusion is an attractive energy source for the upcoming energy crisis, from the energy density perspective. In addition, fusion energy is inexhaustible and safe.

Nuclear fusion is the most common energy source in the universe. Almost all stars have nuclear fusion. On the Earth, fossil fuels come from ancient plants and animals. Photosynthesis is the basic form of energy storage for those plants; then it is transferred to the animals. In other words, most energy resources on the Earth came indirectly from the nuclear fusion in the Sun.

Man's first direct use of nuclear energy was nuclear fission, and it has been a part of modern energy consumption since the mid-1950s [8]. Currently, 14% of electricity is generated by nuclear fission power plants. The USA, France, and Japan have the most nuclear power plants in the world. The demand for new nuclear power plants is expanding in most industrial countries. However, some accidents have occurred at nuclear power plants (e.g., Three Mile Island (USA, 1979), Chernobyl (former Soviet Union, 1986) and Fukushima (Japan, 2011)), and the public is concerned about the effects of radioactive pollution on people and the natural environment. The radioactivity of fission fuels and other transmutation products is strong and long-lasting. Thus, the wide use of controlled fusion energy is highly desirable.

Controlled nuclear fusion consumes D_2 and T_2 or ^3He. The fusion reactions of primary interest are [9, 10]:

$D + {}^3He = {}^4He\,(3.66 MeV) + p\,(14.64 MeV)$;

$D + T = {}^4He\,(3.52 MeV) + n\,(14.08 MeV)$.

The more promising reaction for a fusion power plant is D-T fusion because of the relatively moderate temperature required ($5 \times 10^7 K$), compared with that required for D-^{3}He ($3.5 \times 10^8 K$) [11]. Tritium is short-lived: the half-life of tritium is 12.5 years [12]. However, the neutrons produced in D-T fusion provide a means of closing the fuel cycle if the neutrons are captured by lithium nuclei. Consequently, tritium can be produced within the fusion plant itself by the reactions [13]:

$n + {}^6Li = T + {}^4He + 4.8 MeV$;

$n + {}^7Li = T + {}^4He + n' - 2.5 MeV$.

To minimize neutron surplus, fusion researchers seek reactions in which the production of neutrons is reduced. The most suitable choices appear to be D-^{3}He, p-^{6}Li, and p-^{11}B reactions [14,15]:

$$p + {}^6Li = \eta + {}^7Be + 11.3MeV;$$

$$p + {}^{11}B = 3{}^4He + 8.7MeV.$$

The final goal of fusion research is to obtain a condition in which the charged fusion products, alpha particles (^{4}He) for a deuterium-tritium (D-T) reaction, provide plasma with the necessary power to compensate for energy loss and to maintain plasma temperature at the required level [16].

Deuterium can be largely distilled from sea water, ^{6}Li is also abundant in the ocean, and Moon soil is rich in He^3. They can satisfy energy consumption at the current rate for billions of years [17]. Another advantage of nuclear fusion is that the reaction product, He, is a low-activation element. Moreover, the fusion power plant is very safe because the nuclear reaction happens in vacuum, which can be stopped automatically when vacuum vessel is broken [18].

However, controlled fusion energy requires still further advancement, since the reaction needs ultra-high plasma density, ultra-high plasma temperature, and long-term confinement. Achieving self-sustained plasma burning and constructing fusion reactors are the two most important issues. At present, worldwide efforts are focusing on plasma control and engineering technologies. Recently, an experimental fusion reactor, the International Thermonuclear Experimental Reactor (ITER), is being constructed through international cooperation to demonstrate the feasibility and integration of essential issues for controlled fusion reaction [19]. In the future, a demonstration fusion reactor (DEMO reactor) will be constructed to resolve engineering issues [20]. Figure 1-4 depicts the structure of the ITER [21]. This project was proposed in 1988, constructed under the global framework of cooperation among the main industrial countries beginning in 2007, and is expected to be completed in 2037 [22].

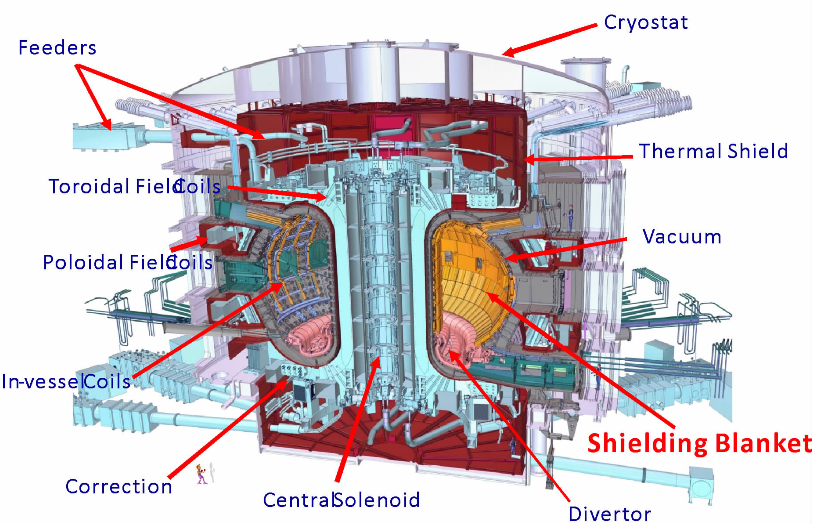

Fig. 1-4 Structure of ITER [21]

Controlled fusion reactions require two important parameters [23]. One is the central ion temperature at which the fuels are charged into plasma and have enough kinetic energy for two light nuclei to collide and form a heavier nucleus. The other is the fusion triple product of $n_i \tau_\varepsilon T_i$, where n_i is the peak ion density, τ_ε is the overall plasma energy confinement time, and T_i is the peak ion temperature. Usually, a self-sustaining fusion reaction needs an ion temperature exceeding 1×10^8K (10keV) and a fusion triple product value of 7×10^{21}keV. s. m^{-3}. With the advances in fusion research of the past five decades, the world is now achieving ITER ignition [21] (Fig. 1-5).

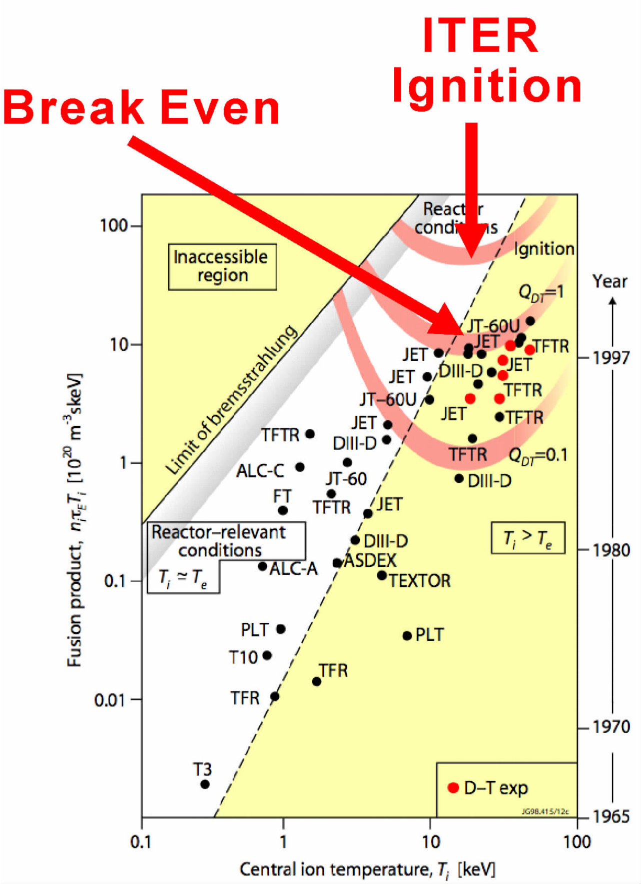

Fig. 1-5 Progress in fusion reactor performance [21]

Thus, there is much hope of achieving stable engineering operation.

Since the ITER project focuses mainly on the feasibility of self-sustained fusion reaction, more efforts are needed for economic engineering operation after successful control of plasma burning. Actually, in parallel with the construction of ITER, the next step of fusion reactor design, DEMO, has also attracted much interest around the world. Research on another type of fusion reactor, the helicon, has made much progress in recent decades [24]. The structure of a famous helical reactor, FFHR2, which is being constructed as a step in achieving DEMO, is depicted in Fig. 1-6.

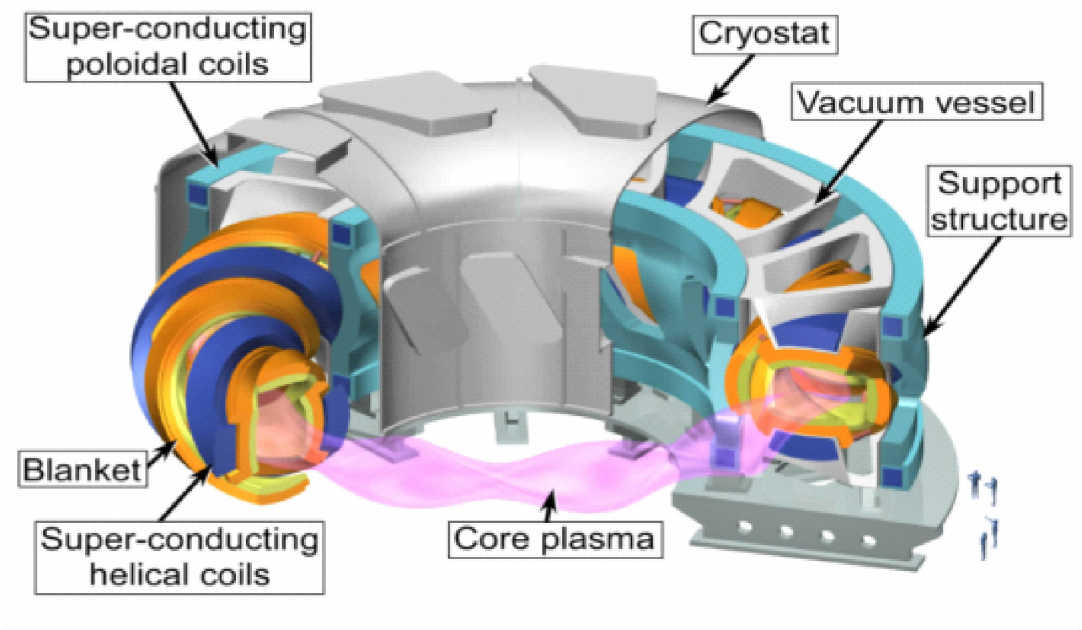

Fig. 1-6 Structure of a helical reactor (FFHR2) [25]

DEMO, the successor of ITER, will achieve an energy output of 2000MW [26] and have an energy density that exceeds that of even large fission power plants [27]. Commercial reactors are expected to be in service around 2050 [28] if material issues are resolved. At that stage, commercial fusion power plants will be available to satisfy worldwide energy demands.

Table 1-1 lists the parameters of ITER, DEMO, and future commercial reactors.

Table 1-1 General parameters for the performance of fusion devices [29]

	ITER	**DEMO**	**Commercial Plant**
Fusion Power, GW	0.5-1	2-4	3-4
Neutron wall loading (first wall), MW/m^2	0.5-1	2-3	2-3
Integrated wall load (first wall)			
In MWy/m^2	~0.3-1	3-8	10-15
In displacements per atom (dpa)	3-10	30-80	100-150
Operation mode	Pulsed	Quasi-continuous	

The DEMO can be a tokamak type or helical type. Both types of reactor are included in the magnetic confinement concepts. There are many concepts for fusion reactors [30], and some use inertial confinement (Fig. 1-7). However, whichever concept is used, materials are needed to construct the body of the fusion reactors [31, 32].

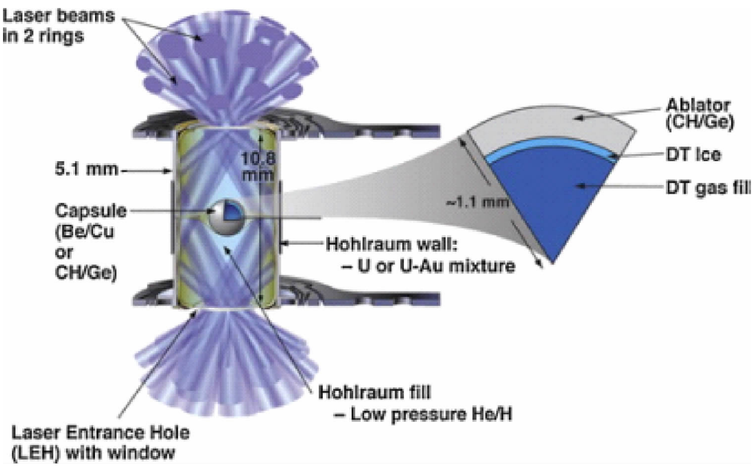

Fig. 1-7 Concept of inertial confinement for controlled nuclear fusion [33]

1.3 Requirements for Structural Materials in Fusion Reactors

The structural material near the first wall of a commercial fusion reactor is one of the most important issues because the high flux of neutrons may seriously degrade the material [34, 35]. However, plasma burning should be confined in an environment with extreme conditions including ultra-high temperature, vacuum, and magnetic field. The material issues at present are attributed mainly to the critical requirements of the magnet system, divertor, and first wall/blanket system. The blanket has multiple roles: (i) converting kinetic energy of neutrons into heat, (ii) evacuating the heat to generate a cycle in order to supply electricity, (iii) producing the tritium necessary for continued fusion reactions, (iv) protecting the magnets from neutron and gamma radiation, and (v) maintaining low density of impurities in plasma (for the first wall). However, the blanket has the most difficulty in application. Unfortunately, no currently available commercial material can perfectly satisfy all the requirements for the blanket in a fusion reactor.

The general requirements for the structural material of a blanket are as follows.

(1) Low induced activation, because high-activation materials cause serious radioactive pollution in the environment.

(2) Good physical properties in the magnetic field to ensure stable plasma control.

(3) Acceptable industrial capability in fabrication, joining, and maintenance to ensure lower construction cost and to save time in component replacement.

(4) Good compatibility with cooling fluids, to ensure the reliability and life of the components in contact with corrodible agents.

(5) Satisfactory mechanical properties at high temperature (HT) to enable the design of components to improve energy-conversion efficiency.

In detail, those requirements are (a) low activation from 14MeV neutrons, (b) resistance to 14MeV neutron-induced displacement damage, (c) early and simple recycling potential, (d) low swelling or void formation, (e) resistance to helium and hydrogen produced by nuclear reactions, (f) high heat conductivity independent of radiation damage level, (g) low corrosion by liquid coolant/breeder (e. g., Li and Li-Pb), and (h) high strength at elevated temperatures and acceptable ductility [36]. Thus, the selection of material should take priority.

First, the selection of material is based on the limit of low activation for each element in the periodic table. Only a handful of elements have acceptable radiological safety performance and low levels of long-term induced activation (Fig. 1-8) [37]. These elements were qualified using reduced activation materials exposed to intense fluxes of fusion neutrons [38-40]. The number of options was further reduced upon consideration of the high-performance requirements for fusion: high thermal efficiency (high operating temperatures), acceptable lifetime in an intense radiation field with high thermo-mechanical stresses, high reliability and maintainability, and chemical compatibility with tritium breeder materials (liquids or ceramics) along with associated coolants [41].

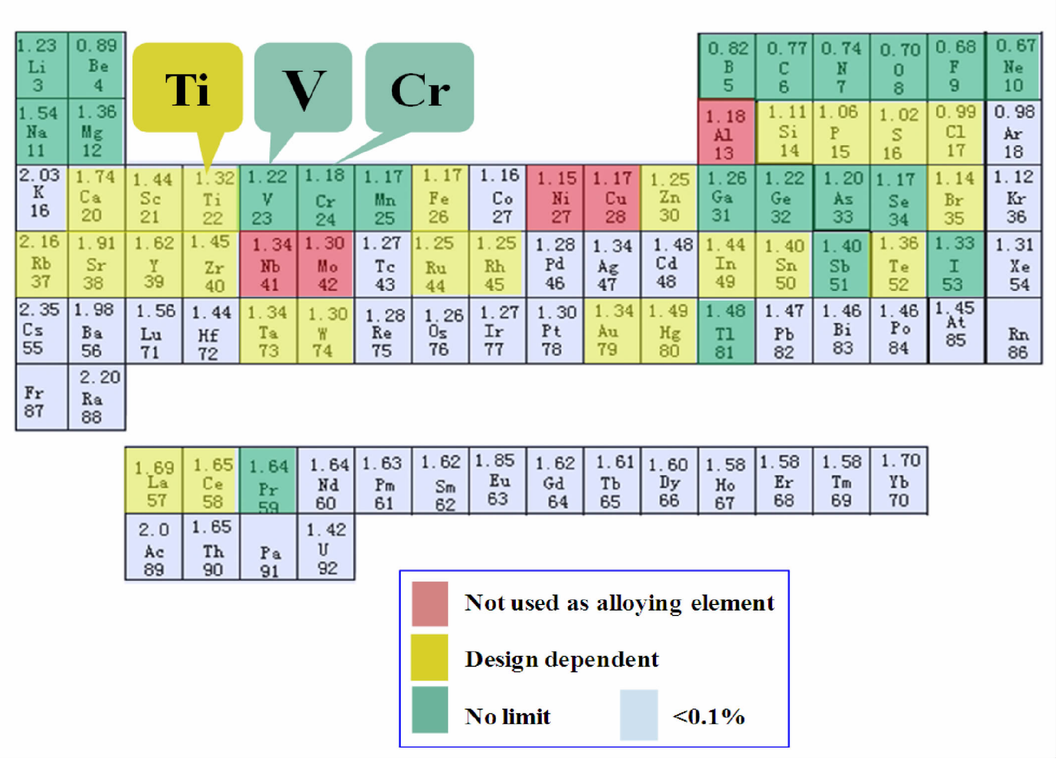

Fig. 1-8 Elements for fusion structural materials [37]

1.4 Development Strategy for Structural Materials

According to long-term evaluation of the nuclear, physical, chemical, and mechanical properties and the reliability of possible fusion structural materials, reduced activation ferritic/martensitic steel (RAFM), vanadium alloys, and SiC composites (SiC_f/SiC) are attractive structural materials for blankets [42]. Vanadium alloys with compositions of the V-Cr-Ti system have recently been identified as the leading candidates for liquid lithium blankets [43, 44]. For comparison, Table 1-2 lists the material conditions of the main blanket designs in Japan and the USA. Liquid metals and molten salts are widely considered to be both breeders and coolants. ARIES-RS, which uses Li, seems to be promising, due to its high operation temperature and simple structure [45].

Table 1-2 Reactor design and combination of blanket materials in Japan and the USA [25].

Reactor design	**SSTR** [46]	**FFHR** [47, 48]	**DREAM** [49]	**ARIES-RS** [50]	**ARIES-AT** [51]
Structural materials	RAFM	RAFM	SiC_f/SiC	Vanadium alloys	SiC_f/SiC
Breeder	Solid breeder	Flibe *	Solid breeder	Li	Pb-17% Li
Coolant	Water	Flibe *	He gas	Li	Pb-17% Li
Coolant temperature	285/325℃	450/550℃	600/900℃	330/610℃	650/1100℃

SSTR: Steady state tokamak reactor (JAEA)

FFHR: Helicon reactor (NIFS)

DREAM: Advanced tokamak reactor (JAEA)

ARIES-RS, ARIES-AT: Reversed shear tokamak reactor, Advanced tokamak reactor (USA, UCSD)

Flibe * is $LiF + BeF_2$.

Industrial capability is an important factor that limits the application feasibility of these three structural materials. Figure 1-9 classifies blanket concepts by attractiveness and development risk of RAFM steel, vanadium alloys, SiC_f/SiC composites, and other possible candidate materials [52]. Attractiveness is based on operation temperature and thus energy-conversion efficiency. According to this figure, ferritic steel is currently the most feasible choice, with vanadium alloys following.

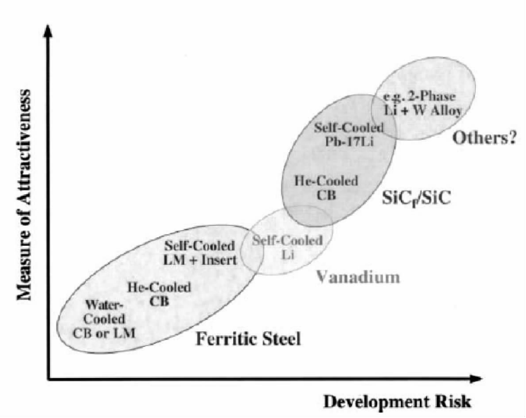

Fig. 1-9 Classification of blanket concepts based on attractiveness and development risk [52]

Ferritic/martensitic steel is furthest along the development path, with well-developed technology and broad industrial experience with such alloys in fossil and nuclear energy technology [53]. This steel is based mainly on modification of the compositions in Fe-(8-12)Cr-(1-2)Mo by replacing Mo, Ni, and Nb with W, V, and Ta in order to obtain low-activation properties. Research groups worldwide have characterized some well-known ferritic/martensitic steel (e. g., ORNL 9Cr-2WVTa [54], EUROFER 97 [55], F82H [56], JLF-1 [57], CLAM [58], and CLF-1 [59]). Its thermophysical and mechanical properties, and compatibility with major cooling and breeding materials are good [60]. Its sensitivity to swelling and helium embrittlement is acceptably low [61]. The technologies for joining ferritic/martensitic steel require less atmosphere control and are more feasible than those for the vanadium alloys and SiC$_f$/SiC composites [35]. A major issue of ferritic/martensitic steel is that its ferromagnetism may change plasma stability [62]. Moreover, its upper operation temperature, 550℃ [34], is the lowest among the three.

Development of SiC$_f$/SiC composite materials presents the most difficult challenge among the three groups of materials [63]. The SiC$_f$/SiC composite has the highest potential operation temperature and the highest strength. The corrosion resistance of this material is also good [64]. However, its greatest shortcoming is its very limited industrial capability for large-scale fabrication and the difficulties in joining [35]. Moreover, for sustaining a vacuum environment, the SiC$_f$/SiC composite has the worst hermetic sealing capability [65]. Thus, in the future, SiC$_f$/SiC composite will have to be further investigated to realize its application [53].

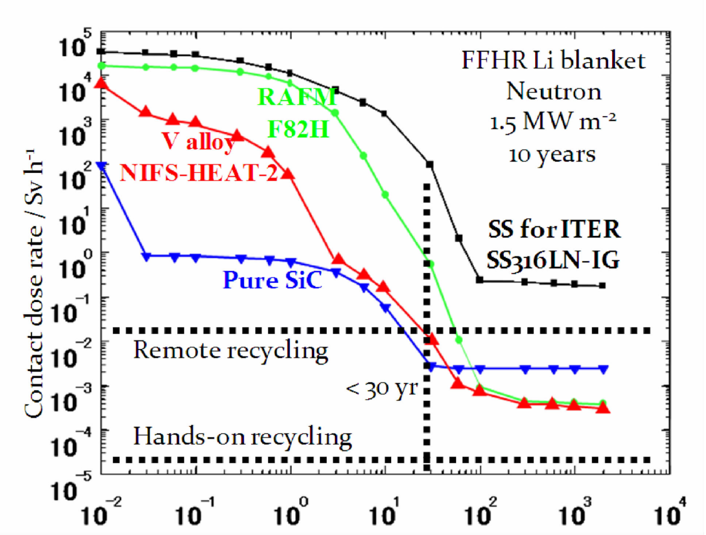

Fig. 1-10 Dose rate after shutdown for different structural materials [67]

Dose rate after shutdown has been investigated for different structural materials to evaluate the low-activation properties of structural materials. Figure 1-10 plots the dose rate of an FF-HR blanket as an example. Here, the RAFM steel is F82H [66], and the vanadium alloy is NIFS-HEAT-2 [67] with compositions of V-4Cr-4Ti. The reference material is a type of austenitic steel, SS316-LN-IG [68], with a high Mo concentration, to be used in ITER. Based on this evaluation, after operation at 1.5MW/m^2 for 10 years, pure SiC and vanadium alloy can be remotely recycled within 30 years. Regarding other physical properties, RAFM steel is ferromagnetic and SiC components are brittle compared with those of V-4Cr-4Ti alloy. Thus, the V-4Cr-4Ti alloy is very attractive from the application viewpoint.

1.5 Statues of Vanadium Alloys

Studies of metals as structural materials are more mature than those of ceramics. No schedule for the application of SiC_f/SiC components can be determined at present. Because the radioactivity levels of vanadium alloys are lower than those of ferritic/martensitic steels, the vanadium alloys may be suitable for advanced fusion reactor designs that utilize high wall loads and high power density. It has been repeatedly pointed out that vanadium alloys have recycling and reuse potential [69].

Mechanical properties: Vanadium alloys based on V-Cr-Ti compositions have a favorable combination of physical properties and high creep strength for long-term operation at temperatures up to 700℃ [70]. Swelling and ductility loss due to irradiation-induced defects are also low for vanadium alloys [71].

Chemical properties: The high compatibility of vanadium alloys with liquid Li potentially results in high thermal efficiency due to high operation temperatures. Moreover, the Li/V blanket needs neither an additional neutron multiplier nor a ceramic breeder, both of which must be replaced periodically.

Research in the 1990s satisfactorily resolved many key issues associated with the feasibility of utilizing vanadium alloys in fusion reactor structures [72]. An initial property database on a number of vanadium alloys was developed in the USA [73].

For systematic research on optimizing compositions of vanadium alloys, researchers at Argonne National Laboratory tried modifying the contents of each alloying element (Table 1-3) to determine the most promising composition. Cr and Ti are popular because Cr can increase the creep resistance of the alloy, and Ti is most effective for suppressing irradiation-induced swelling [74]. It was found that increasing strength is obtained by increasing Ti and especially Cr concentrations. The mechanism of solid solution hardening is simple [75]. Figure 1-11 plots Cr as an example, indicating that the ultimate tensile strength for the alloy with higher Cr content is higher at all testing temperatures.

A research group at Argonne National Laboratory also investigated the effect of Cr content on DBTT. Results indicate that up to 4wt.% Cr, the vanadium alloy maintains the lowest DBTT in various conditions, regardless of whether it is annealed in vacuum, irradiated, or hydrogenated (Fig. 1-12) [78]. Further research [79] indicated that the Cr concentration should not exceed 7wt.% because the DBTT of vanadium alloys increases sharply by 150℃ up to near room temperature (RT) (Fig. 1-13), which is very dangerous for structural materials.

Table 1-3 Chemical compositions of vanadium and vanadium alloys for optimization. [76]

Nominal composition	ANL. I. D.	Concentration (wt. %)			Concentration (ppm)			
		Cr	Ti	Fe	O	N	C	Si
V	BL 51	—	—	—	570	49	56	370
V-1Ti	BL 60	—	1.0	—	230	130	235	1050
V-3Ti	BL 62	—	3.1	—	320	86	109	660
V-3Ti-1Si	BL 45	—	2.5	0.01	345	125	90	9900
V-5Ti	BL 46	—	4.6	—	300	53	85	160
V-10Ti	BL 12	—	9.8	0.63	1670	390	450	245
V-18Ti	BL 15	—	17.7	0.04	830	160	380	480
V-14Cr	BL 5	14.1	—	0.06	330	69	200	50
V-14Cr-1Ti	BL 26	14.1	1.0	0.06	560	86	140	50
V-5Cr-3Ti	BL 54	5.1	3.0	—	480	82	133	655
V-4Cr-4Ti	BL 47	4.1	4.3	—	350	220	200	870
V-5Cr-5Ti	BL 63	4.6	5.1	—	440	28	73	310
V-8Cr-6Ti	BL 49	7.9	5.7	—	400	150	127	360
V-9Cr-5Ti	BL 43	9.2	4.9	0.02	230	31	100	340
V-14Cr-5Ti	BL 24	13.5	5.2	0.05	1190	360	500	390
V-15Cr-5Ti	BL 41	14.5	5.0	0.02	330	96	120	400
V-10Cr-9Ti	BL 44	9.9	9.2	0.04	300	87	150	270
V-7Cr-15Ti	BL 10	7.2	14.5	0.09	1110	250	400	400

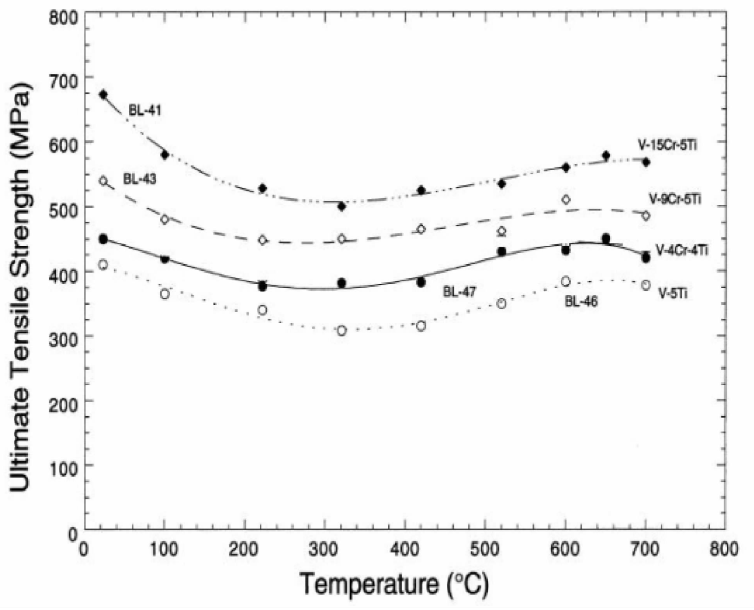

Fig. 1-11 Dependence of ultimate tensile strength on Cr concentrations for vanadium alloys [77]

A similar trend of DBTT shift for Ti is plotted in Fig. 1-14 [78]. Vanadium alloys with 1wt.% to 5wt.% Ti have the lowest DBTT with or without irradiation. Hydrogenation may affect the DBTT; however, 5wt.% Ti still brings benefits to the lower DBTT property.

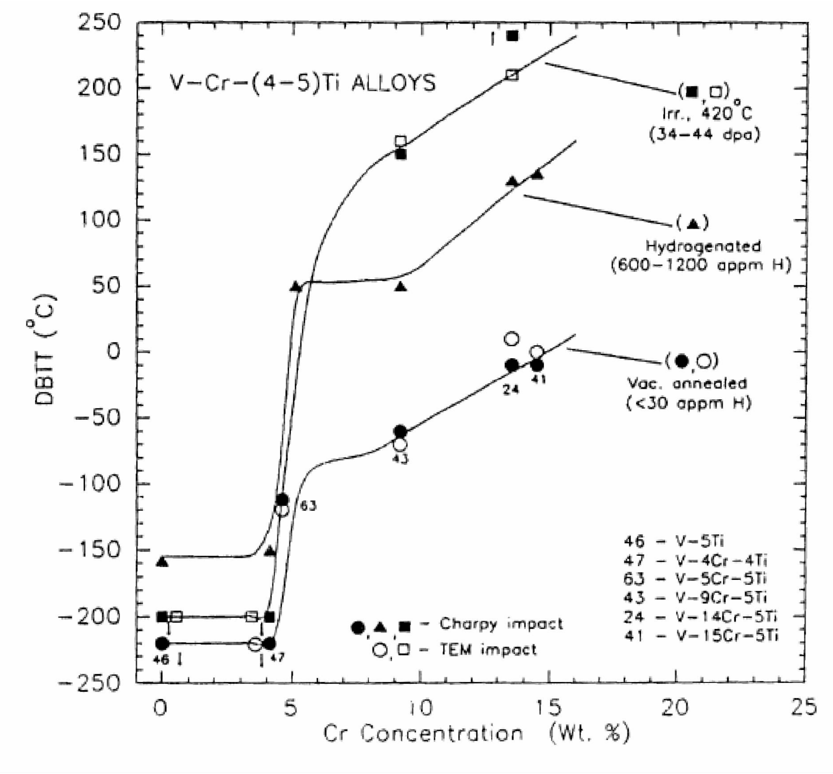

Fig. 1-12 Dependence of DBTT shift on Cr concentrations for vanadium alloys [78]

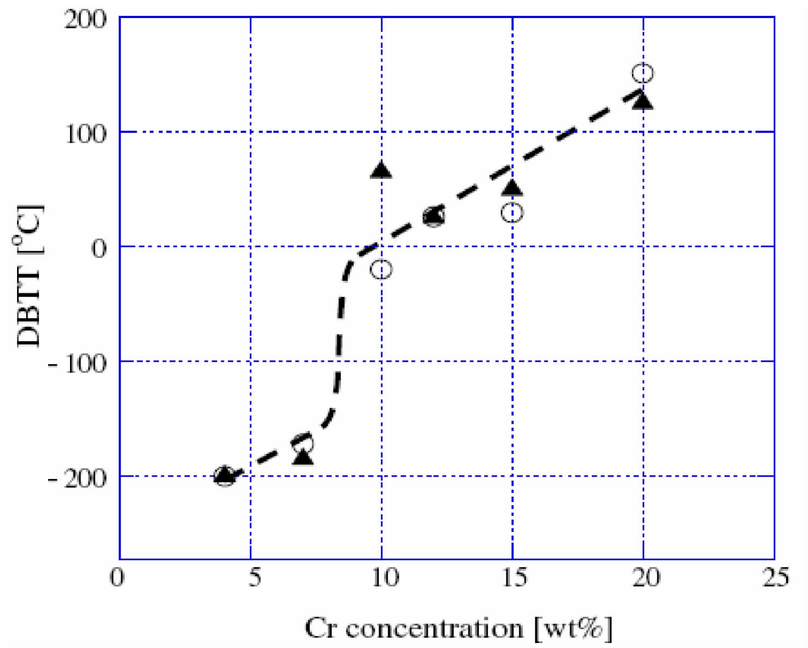

Fig. 1-13 Updated dependence of DBTT shift on Cr concentrations for vanadium alloys [79]

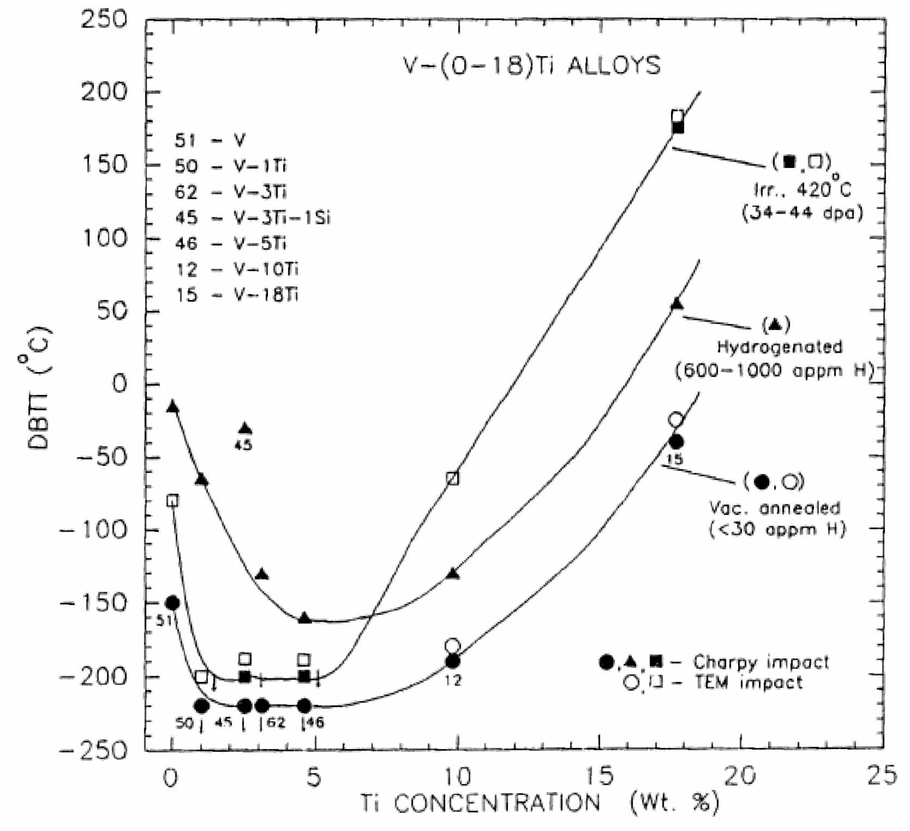

Fig. 1-14 Dependence of DBTT shift on Ti concentrations for vanadium alloys [78]

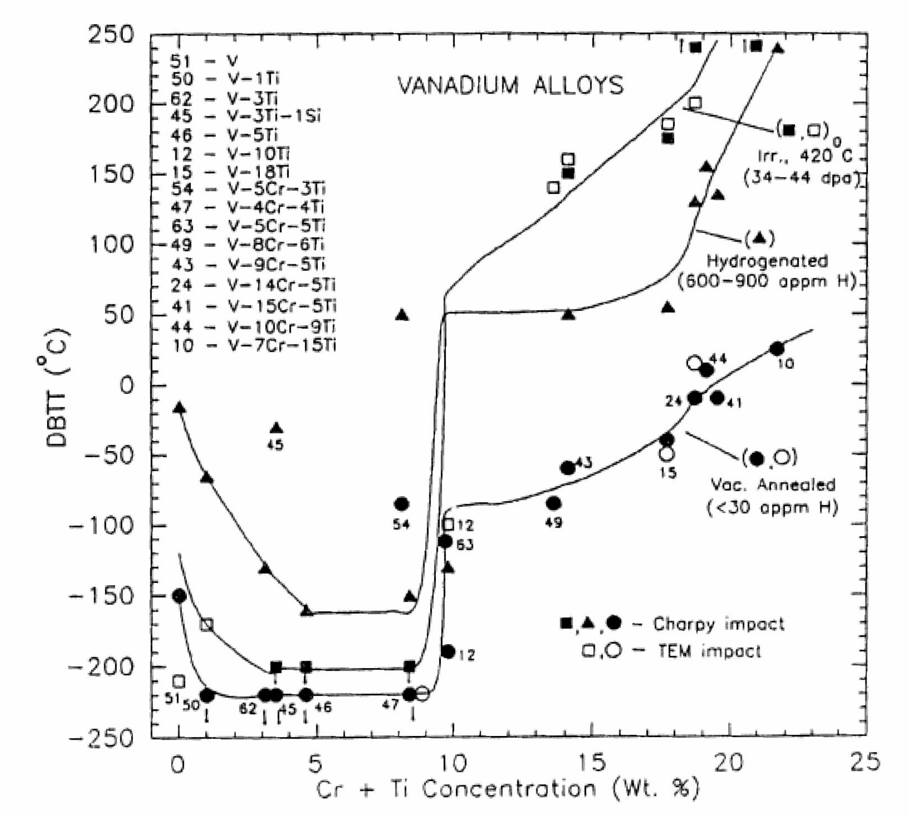

Fig. 1-15 Dependence of DBTT shift on Cr + Ti concentrations for vanadium alloys [78]

Figure 1-15 plots the dependence of DBTT for vanadium alloys on the combined (Cr + Ti) concentration in an alloy. These results suggest that the minimum DBTT for unirradiated, hydrogenated, or neutron-irradiated V-Cr-Ti alloys is obtained for a vanadium alloy containing 0 to 4wt.% Cr and 1 to 5wt.% Ti, or a combined (Cr + Ti) concentration less than 10wt.%. Additional irradiation effects on DBTT change versus (Cr + Ti) concentrations are plotted in Fig. 1-16 [77].

V-4Cr-4Ti might not exhibit the lowest DBTT according to the fitting in Fig. 1-16. However, considering that Cr is transmuted mainly into V under neutron irradiation after sufficient long-term service in the reactor, the Cr concentrations decrease, and then the DBTT for pre-V-4Cr-4Ti alloy is expected to obtain a near minimum DBTT.

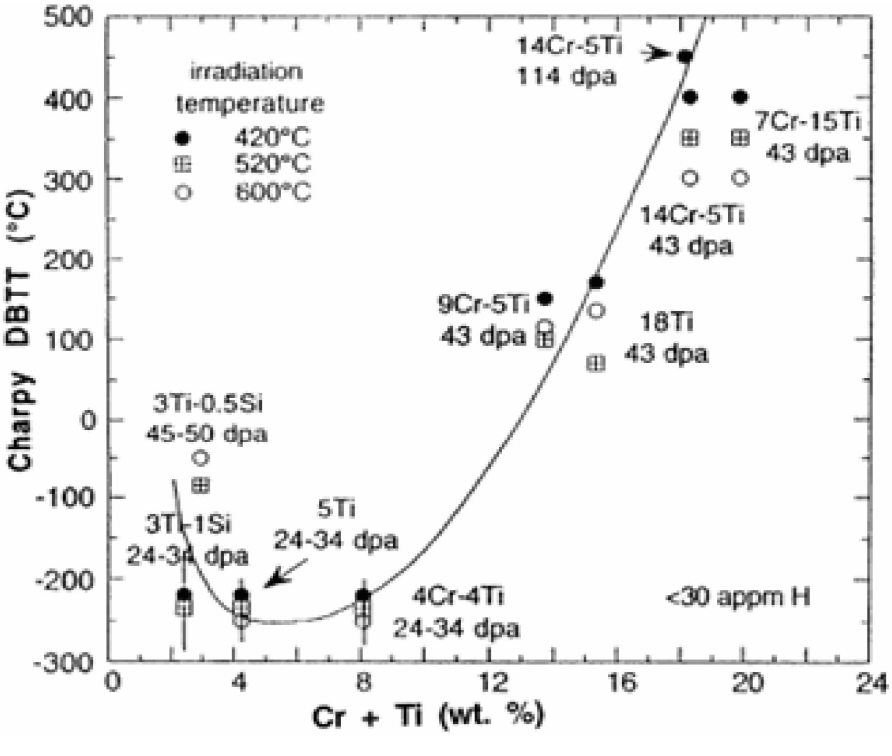

Fig. 1-16 Dependence of DBTT shift on Cr + Ti concentrations for irradiated vanadium alloys [77]

Based on the above and other considerations, vanadium alloy with compositions of V-4Cr-4Ti was identified as the leading material among all the candidate vanadium alloys.

As a result, efforts have been made in Japan (NIFS) [66] and Russia [80] to produce 30 to 200kg V-4Cr-4Ti ingots with improved purity. Decreasing the C, O, and N concentrations is a main issue in large-scale alloy fabrication. Most recently, China (SWIP) and France (CEA) have joined in large-scale highly pure V-4Cr-4Ti alloy fabrication [81, 82]. The chemical compositions for large-scale ingots are listed in Table 1-4. CEA-J57 is meant for fission applications in order to fabricate fuel cladding in Generation IV fission power plants [82].

Table 1-4 Chemical compositions of V-4Cr-4Ti alloys fabricated in Japan, the US, China, and France [67, 81-85]

ID	C	O	N	B	Si	P	S	As	Sn	Sb
NIFS-HEAT-1	56	181	103	7	280	16	9	1	<1	<1
NIFS-HEAT-2	67	148	122	5	270	7	3	<1	<1	<1
US832665	170	330	100	3.7	785	33	16.5	1.4	0.24	0.17
US832864	37	357	130	—	273	<30	—	—	—	—
SWIP-30	130	270	20	—	590	—	20	—	—	—
CEA-J57	70	290	110	10	280	<30	8	—	<10	<10
	V	Cr	Ti	Nb	Zr	Ca	Co	Ag	Al	
NIFS-HEAT-1	Bal.	4.12	4.13	1.4	<10	3	2	<0.05	119	
NIFS-HEAT-2	Bal.	4.02	3.98	0r.8	2.5	12	0.7	<0.05	59	
US832665	Bal.	3.25	4.05	60	<46	<0.26	0.30	0.078	355	
US832864	Bal.	3.8	3.8	106	—	4	—	—	193	
SWIP-30	Bal.	3.81	3.92	—	<10	67	—	—	100	
CEA-J57	Bal.	3.76	3.93	<10	—	<10	<10	—	190	
	Mn	Fe	Ni	Cu	W	Mo	Ta	Na	Mg	
NIFS-HEAT-1	<1	80	13	4	<1	23	58	17	<1	
NIFS-HEAT-2	<1	49	7	2	<1	24	13	<1	<1	
US832665	0.21	205	9.6	0.84	25	315	<19	0.01	0.17	
US832864	—	228	—	<50	—	<50	—	<2	<1	
SWIP-30	—	53	82	—	—	35	10	50	22	
CEA-J57	7	145	17	<50	35	75	<10	40	<10	

Considering that other low-activation metallic elements can also strengthen vanadium, some efforts have contributed to the fabrication of advanced vanadium alloys in the past decade. For example, 6 to 8wt.% W was added to vanadium with or without Ti [86]. Results indicate that W strengthens more than either Cr or Ti [86]. Interestingly, the effects of W on recovery and recrystallization are similar to that of Cr, and the addition of W did not influence the H embrittlement of V-Ti alloy. However, the addition of W did not remarkably facilitate precipitation hardening [86]. Current studies focusing on the modification of alloying elements in melted vanadium alloy have not been given priority. Most experiments in the US and Japan have been carried out using V-4Cr-4i alloys fabricated in the 1990s and 2000s (e.g., US832665 and NIFS-HEAT-2).

Recently, mechanical alloying (MA) has been applied to fusion structural materials, including vanadium alloys [87-109]. The pinning of dislocations by dispersed nanoparticles greatly increases the strength of the materials at both RT and HT. The main interest in mechanically alloyed vanadium alloys is the enhanced thermal creep resistance. V, V-Cr, V-Ti, and V-W systems have been introduced in MA study, with Y as the scavenger for impurities such as O and N. Though data are limited, creep results indicate that mechanically alloyed vanadium alloys have suitable tensile and creep strength at HT. The main role of nanoparticles in the site formed or added in starting powders is to strengthen the MA vanadium alloys. However, the effects of refined grains on creep rate is an issue, since more grain boundaries supply more sinks for atom diffusion, accelerating creep deformation with possible grain boundary sliding mechanism due to the smaller grain sizes. It is necessary to anneal the material for coarsened grains and then obtain a lower creep rate. Figure 1-17 [109] plots creep curves for MA vanadium alloys compared with those for melted V-4Cr-4Ti alloy (NIFS-HEAT-2). The mechanically alloyed vanadium alloy with 1200℃ annealing is stronger than the melted V-4Cr-4Ti alloy, even with its 0.58μm original grains. When annealed at higher temperatures, the grains coarsen to 0.90μm at 1300℃, 1.46μm at 1400℃, and 2.16μm at 1500℃. Accordingly, the creep rate decreases and the fracture lifetime is greatly extended, although the coarsened grains are still smaller than those of NIFS-HEAT-2 (17.8μm) [109]. Particles near the grain boundaries should resist grain deformation during creep.

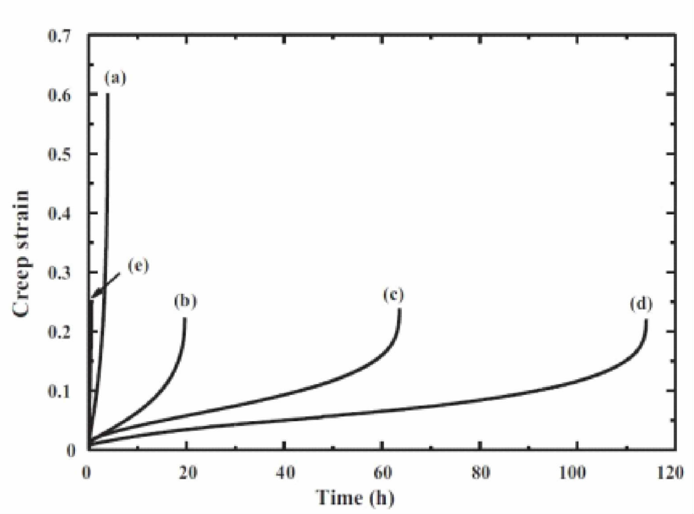

Fig. 1-17 Creep (1073K and 250MPa) curves of mechanically alloyed V-1.4Y-7W-9Mo-0.7TiC alloy after annealing at different temperatures, compared with melted V-4Cr-4Ti alloy. Grain sizes are (a) 0.58μm, (b) 0.90μm, (c) 1.46μm, and (d) 2.16μm. (e) V-4Cr-4Ti (NIFS-HEAT-2, with standard heat treatment) with a grain size of 17.8μm [109]

Moreover, since grain boundaries and interphase boundaries can act as efficient sinks for point defects produced by neutron irradiation, alloys possessing ultra-fine grains and fine-scale particles may be more resistant to radiation-induced embrittlement [88]. Thus, MA is expected to have multiple benefits for vanadium alloys in the fusion reactor environment. However, V-4Cr-4Ti has not been introduced into MA study in the past decade. Additional MA research on vanadium alloys including V-4Cr-4Ti system is necessary.

1.6 Issues of Li/V Blanket

It has definitely been confirmed that V-4Cr-4Ti alloys have promising low-activation properties, inherent nonmagnetic properties, and a high melting point, depending on the selection of elements. Thus, more vanadium alloys of high purity and advanced vanadium alloy via MA were fabricated. Almost in parallel, practical application of vanadium alloy in liquid Li has also been of great concern. In a self-cooled lithium vanadium alloy structure, lithium has such attractive properties as high tritium breeding capability, high thermal conductivity, immunity to irradiation damage, and the possibility of an unlimited lifetime if the ^{6}Li burn-up can be replenished. The design of the Li blanket has long been of interest, and several concepts of Li/V blankets have been presented (e. g., Tritium, Irradiation, and Thermofluid for America and Nippon (TITAN) [110], JUPITER-II [111], and ARIES-RS [112]). The blanket of ARIES-RS is an example of the Li/V self-cooled concept. It conservatively offers 46% gross thermal conversion efficiency (Cycle η) for the Li/V blanket. Table 1-5 lists some key parameters of ARIES-RS compared with those of other main blanket designs. Figures 1-18 and 1-19 present outboard cross-sections of the tokamak ARIES-RS blanket [113] and the helical FFHR2 blanket [47, 114].

Table 1-5 Design parameters for different blanket concepts [38].

Example concept	**SSTR** [46]	**ARIES-RS** [50]	**ARIES-AT** [51]	**EVOLVE** [122]	**FFHR-2** [123, 124]
Breeder (form)	Li_2O or Li_2TiO_3 (pebble bed)	Li	Pb-17Li	Li	FLiBe
Multiplier (form)	Be (pebble bed)	—	—	—	Be (pebble bed)
Coolant	H_2O	Self	Self	Li (evap.)	Self
Structure	F82H (RAFS)	V-4Cr-4Ti + CaO Ins. Layer	SiC_f/SiC	W Alloy	Ferritic Steel
Structural T_{max} (℃)	550	700	1000	1300	550
Structural T_{min} (℃)	~280	330	764	—	—
Coolant T_{max} (℃)	320 (520a)	610	1100	1200	550
Coolant T_{min} (℃)	280 (290a)	330	764	1100	450
Coolant P (MPa)	15 (25a)	<1	1.1	0.035	0.5
Max. neutron wall load (MW/m^2)	3–5	5.6	4.8	10	1.5
Energy multiplication factor	1.3	1.21	1.11	1.2	—
Tritium Breeding Ratio	1.2	1.1	1.1	>1	>1
Cycle η (%)	~35 (>40a)	46	58.5	>55	38
Structural material lifetime and criteria	>10 MW-a/m^2 100 to 200dpa	15 MW-a/m^2 200 dpa embrittlement	18 MW-a/m^2	Not available	15MW-a/m^2 150dpa swelling

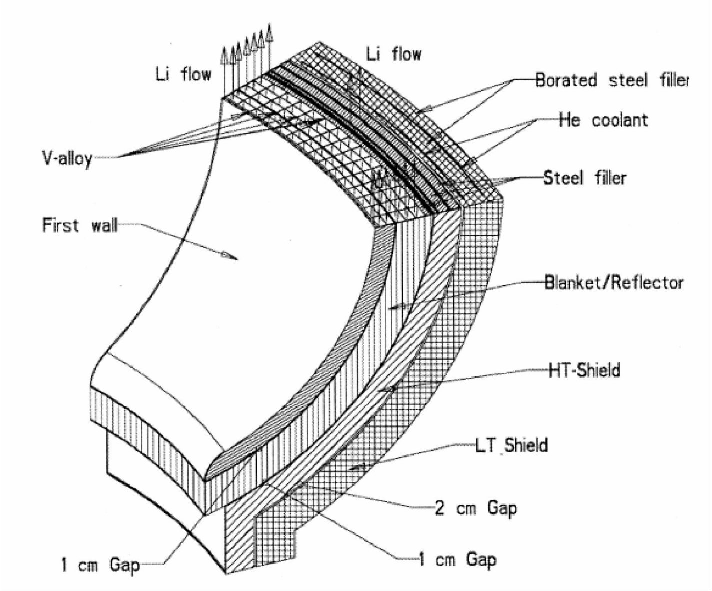

Fig. 1-18 Outboard cross-section of ARIES-RS blanket [113]

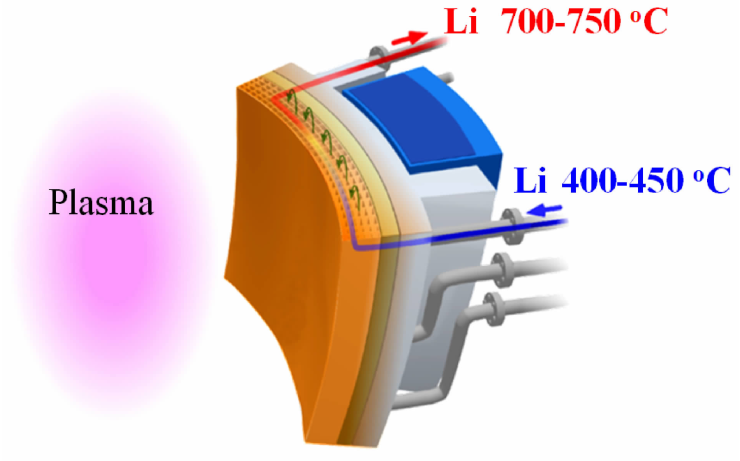

Fig. 1-19 Outboard cross-section of FFHR2 blanket [47, 114]

At Oak Ridge National Laboratory, a monometallic V-4Cr-4Ti thermal convection loop was constructed in order to conduct experiments with flowing Li at 700℃ for determining the compatibility of V-4Cr-4Ti with liquid lithium [115]. In principle, this confirms the possibility of using vanadium-based alloys and compliance of the welding techniques with the requirements for creating the liquid-metal blanket of ITER and DEMO [116].

However, as mentioned before, one remaining key feasibility issue for V alloys is the development of electrical insulator coatings in order to reduce the magnetohydrodynamic pressure drop in the flowing Li loop [117]. At present, relatively few potential insulating material compositions can serve as a MHD insulating layer and be stable in the lithium environment [118]. Even the most promising candidates, Y_2O_3 and Er_2O_3, exhibit degradation in static lithium tests at 600 to 800℃ [119, 120]. With further modification of the design concepts, the most likely alternative either employs a flow channel insert, made up of vanadium alloy foils with an oxide inner layer [121], or applies a multi-layer coating with alternating layers of vanadium and oxide [72]. This design greatly increases electrical resistance and decreases the electrical current, thus decreasing the MHD pressure drop. Figure 1-20 depicts the schematic of coating, V structure, and flowing Li arrangement for the self-healing and multilayer approaches [72].

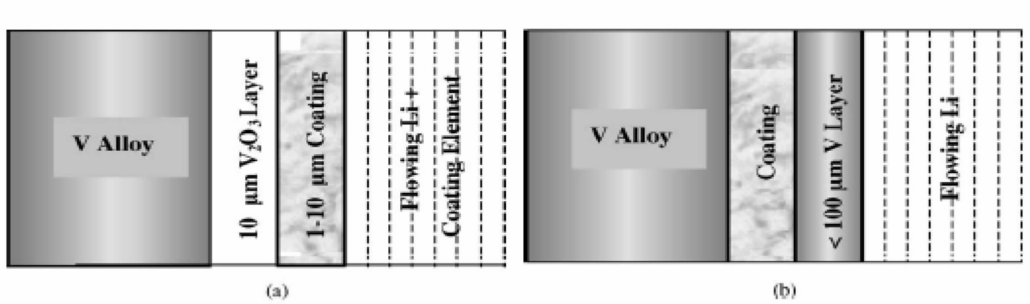

Fig. 1-20 Schematic of coating, V structure, and flowing Li arrangement for the (a) self-healing and (b) multilayer approaches [121]

An appropriate insulator coating has yet to be developed. Evaluation of the feasibility of a multilayered blanket structure should take priority. In addition, problems involving the bonding of vanadium alloys with insulator coatings must be solved. Beyond the reduced MHD effects, vanadium alloy interacts with the impurities in molten Li. Generally, most impurities in purified Li are nonmetallic elements such as C, O, and N from gas, due to inefficient purification, gas leakage, or pervasion from outside. The solubility of C, O, and N is high in molten Li, and lithium compounds can form to accommodate more such impurities. These dissolved impurities have chemical affinities with a solid wall made of vanadium alloy and then mass transfer occurs. The mass transfer is determined by the chemical potential in the disequilibrium system. Calculation of Gibbs free energy of each possible Li compound and the V, Cr, or Ti compounds indicates that N and C can transfer from Li to vanadium alloy due to a strong chemical affinity with Ti, whereas O can transfer from the vanadium matrix to Li (Fig. 1-21).

Such mass transfer remarkably changes the mechanical properties of vanadium alloy. O is the main impurity in V-4Cr-4Ti alloy [125-127]. The loss of O seems to be beneficial, as DBTT of the alloy decreases with decreasing O level. However, trapping of N and C causes embrittlement. Previous studies indicated that among the three nonmetallic elements in Ti-(C, O, N) precipitates that strengthen V-4Cr-4Ti alloy, N is generally concentrated in coarsened precipitate. In this case, the continuous trapping of N changes the precipitation status in V-4C-4Ti alloy and seriously contaminates the alloy. The diffusion coefficients of the elements also differ from one another. The affected range in the alloy gradually changes from the surface with increasing time, resulting in heterogeneity in the alloy cross-section. Accordingly, the mechanical properties of the whole alloy foil gradually change, and inner strain may develop at HT.

Therefore, it is necessary to clarify the effects of interaction between V-4Cr-4Ti alloys with the Li environment.

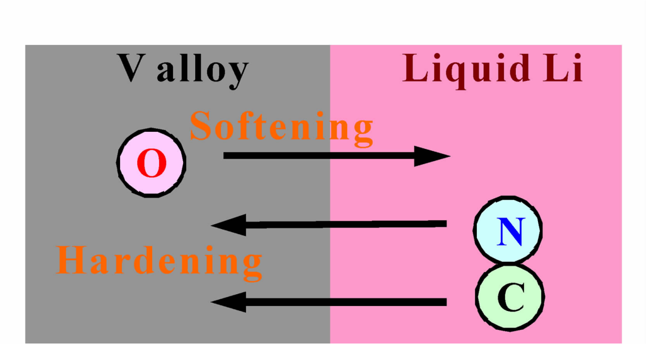

Fig. 1-21 Schematic of mass transfer between vanadium alloy and liquid Li

1.7 Relationship Between Operation Temperature and Energy Conversion Efficiency

The energy conversion efficiency of a blanket depends on the operation temperature of its coolant. However, the highest operation temperatures of the coolants are limited by corrosion of the blanket material, creep lifetime, and He brittlement. Figure 1-22 plots the dependence of energy conversion efficiency on coolant operation temperature for fission reactors and fusion reactors with various coolants. For liquid Li- and LiPb-cooled blankets, the upper-limit temperature can be as high as 900℃ (Table 1-5). However, such a temperature can hardly be achieved in real operation because of failure in the structural materials. With vanadium alloy, the maximum operating temperature limit for V alloys in design studies is typically assumed to be 700℃. Above 700℃, the mechanical properties of the blanket wall are degraded. The vanadium alloy must be strengthened in order to increase the energy conversion efficiency of the Li/V blanket.

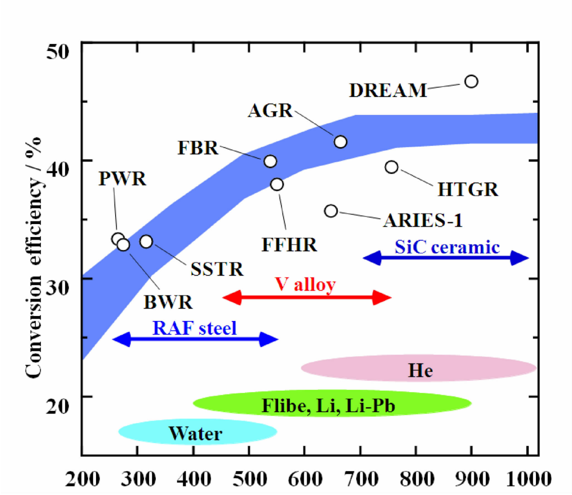

Fig. 1-22 Dependence of energy conversion efficiency on coolant operation temperature for nuclear reactors

Generally speaking, creep strength is one of the most important properties for blanket components working at HT. Thus far, there is not enough creep data for vanadium alloys, including V-4Cr-4Ti. Recently, some efforts have been made to evaluate the creep properties of the heat of V-4Cr-4Ti alloys in order to estimate their performance compared with design criteria. Typically, a lifetime of 10^5hrs for 1% deformation at the relevant minimum creep rate is necessary for first-wall/blanket components of a fusion power system. In order to estimate the limiting stress of V-4Cr-4Ti alloy running for such a long time, a Larsen-Miller parameter plot was made using creep data obtained at different temperatures (Fig. 1-23 [73]). Results indicate that the limiting stress is 74MPa for 700℃, but just 4MPa for 750℃. According to the design of the Li/V blanket, the coolant pressure in this case is 0.5MPa, or less than 1MPa. This should result in relatively low applied loads, including thermal stress in the first wall. Thus, 700℃ operation can be ensured, while many uncertainties remain for 750℃ and even higher temperatures. Improving thermal creep strength would add a margin at 700℃ to account for uncertainties in the designed stress and perhaps expand the design window to higher temperatures.

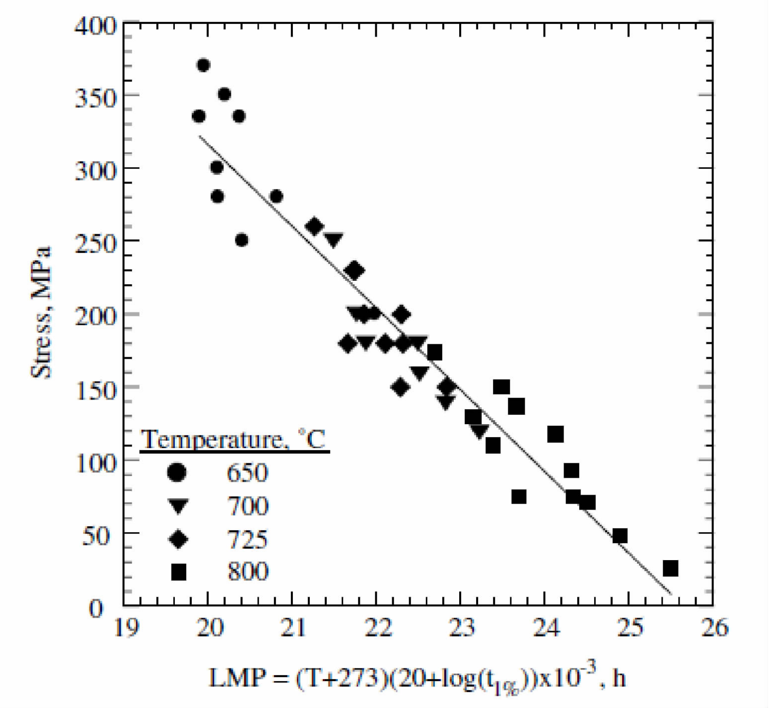

Fig. 1-23 Larson-Miller parameter plot for V-4Cr-4Ti alloy creep at 650 to 800℃ [73]

CHAPTER 2
Purpose of the present study

Great progress in material selection, fabrication, evaluation, and blanket concept design over the past two decades is now making practical blanket operation an attractive subject. High temperatures up to 700℃ and a Li environment are the designed operation conditions for V-4Cr-4Ti alloys. Both issues are related to the mechanical properties of the alloy. Avoiding degradation and enhancing creep strength in a high-temperature Li environment should take priority in future research.

Once the compositions of the main alloy elements are fixed, the best way to strengthen the alloy is to control the microstructures (e. g. , precipitates/nanoparticles, dislocations, and grain sizes). Accordingly, precipitation hardening or nanoparticle dispersion strengthening, work hardening, and grain size refinement are suitable mechanisms for strengthening metals and alloys, including V-4Cr-4Ti. A solid solution can also lead to hardening, and is usually the pre-treatment for precipitation hardening.

However, high-temperature operation and the Li environment require more than simple strengthening. The thermal stability of the strengthening agent is important. Dislocations are generally undesirable in thermal creep because they can provide vacancy diffusion with more sinks. The formation of precipitates, Ti-(C, O, N) interstitial phase, in V-4Cr-4Ti alloy attributes to thermal aging, and also does the unwanted coarsening of precipitates. Suitable precipitation is determined by the operation temperature of V-4Cr-4Ti, compared with the minimum formation temperature of the precipitates. A higher minimum temperature of precipitate formation is desirable for reducing the coarsening rate of precipitates at the operation temperature.

The issues of increasing yield stress using dislocation and precipitation have two possible solutions. One involves combining work hardening and precipitation hardening in order to achieve multiple strengthening to increase yield stress and resist material deformation. The other involves introducing supersaturated solutes into the V matrix in order to produce a high number density of particles with high thermal stability via mechanical alloying (MA). As a result, the degradation of mechanical properties at elevated temperatures is depressed.

Part of this study focuses on strengthening a V-4Cr-4Ti alloy (NIFS-HEAT-2) by combining work hardening and precipitation hardening. Different orders of these two treatments may result in different microstructures in the V matrix, and thus different creep characteristics at high temperature. Research on combined work hardening and precipitation hardening focuses on the creep mechanism. Creep for the same alloy with standard heat treatment is compared with that for combined work hardening and precipitation hardening. To obtain even higher creep resistance for V-4Cr-4Ti alloys, another part of the present study involves strengthening this alloy via MA. The effects of MA process on strengthening this alloy are related to the homogeneity of the alloy matrix and thus of the mechanical properties. This study makes effort to determine what nanoparticles have the highest thermal stability and their nature in evolution. Determining the creep mechanism for nanoparticles and grain size is the most important aim in MA study.

Mass transfer in the Li and V matrix may not be avoided in a liquid Li environment. However, understanding the effects of such mass transfer on precipitation status can lead to optimization of impurity control in material fabrication. Possible improvement of Li purification may also benefits to promote suitable precipitation hardening.

The detailed objectives are as follows.

(1) Evaluate the strengthening capability of combined work hardening and precipitation hardening in either order at RT and high temperature.

(2) Understand the creep mechanisms of combined work hardening and precipitation hardening regarding dislocations, precipitates, and their interactions.

(3) Determine the effects of mass transfer in liquid Li on the mechanical properties and creep mechanism of V-4Cr-4Ti alloy.

(4) Distinguish the quantitative range and effect of C, O, and N on mechanical properties of Li-exposed V-4Cr-4Ti alloy.

(5) Improve high-temperature mechanical properties including creep resistance for V-4Cr-4Ti alloy by the advanced fabrication technique, MA.

(6) Differentiate the dissolution characteristics of alloying elements in V-4Cr-4Ti alloy during MA to optimize process parameters in further fabrication.

(7) Determine what particles in MA vanadium alloy can survive best at temperatures above the blanket-operation temperature.

(8) Clarify the effects of nanoparticle dispersion strengthening and grain size refinement on creep properties at elevated temperatures.

Finally, the core purpose of the present study is to obtain a guiding principle for strengthening V-4Cr-4Ti alloy to resist high-temperature deformation in fusion reactors.

CHAPTER 3

General experimental procedures

3.1 Chemical Analysis.

An alloy system usually includes a series of unexpected elements, or called impurities, beside the base metal and designed alloying element (or elements). Some of them are metallic elements introduced as new alloying elements during the fabrication process when they form substitutional atoms. Some other are nonmetallic elements which are existing based on the universal thermo-dynamic equilibrium, and play important roles in strengthening the alloy by forming precipitates and acting as interstitial atoms. In order to determine the strengthening mechanism for the alloys, it is necessary to determine the impurity levels at first.

In the present study, C, N and O are the most common nonmetallic impurities for V-4Cr-4Ti alloy (NIFS-HEAT-2) from raw materials and the fabrication atmosphere. While in the mechanical alloying, some metallic impurities can also be introduced by the mechanical collisions of milling balls. For analyzing these elements, the present study used different methods.

Carbon concentration is determined by the oxygen combustion method using a carbon analyzer LECO CS-444LS (Fig. 3-1) which equips with an infrared detector. The mechanism is to get quantitative analysis of CO_2 gas emitted from decomposed samples at high temperature in pure oxygen atmosphere. N is measured using thermal conductivity method, and O is measured by infrared absorption. Both N and O can be analyzed with the inert gas fusion method using a Nitrogen/Oxygen Analyzer (LECO TC-600) as shown in Fig. 3-2. Highly pure helium gas up to 99.9995% purity was used in the nitrogen and oxygen analyses.

Fig. 3-1 Carbon/Sulfur analyzer (LECO CS-444LS)

Fig. 3-2 Nitrogen/Oxygen Analyzer (LECO TC-600)

Concentrations of V, Cr Ti and other solid impurities like Si, W and Co are measured by wet analysis. The mechanisms are various as shown in Fig. 3-3. Samples for each element should be at least 0.4g and the size of every bulk sample should be smaller than 5mm × 5mm × 5mm.

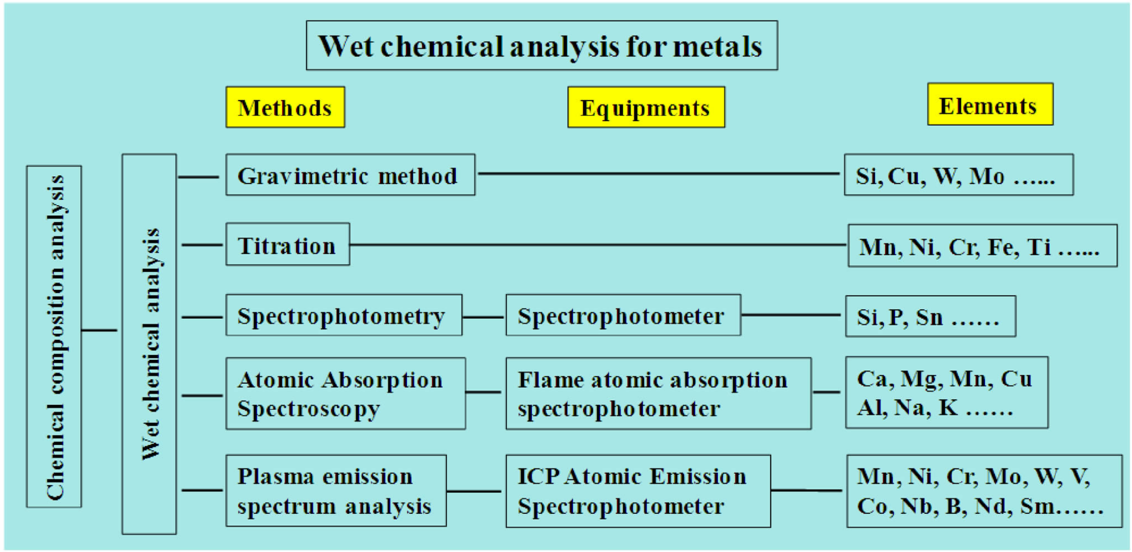

Fig. 3-3 Sketch of wet chemical analysis methods

3.2 Hardness Tests.

Hardness is an important mechanical property of an alloy, and is usually the first property to measure. With small deformation areas and limited strains, the hardness can show the homogeneity of mechanical property on small scale sample in the present study.

Fig. 3-4 Grinding machine

The samples are first ground to get a smooth surface on a grinding machine (Fig. 3-4). Sand papers varying from 180 meshes to 600 meshes are used one by one. The grinding is carried out with the rotation speed at 100-300rpm for 30min and a load of 3-4 Newton in pure water flow. After paper grinding, an emery cloth polishing is carried out at the rotation speed of about 200rpm for 3hrs using abrasive varies from 3μm to 0.05μm in size. Grinding oil is used for cloth polishing. Finally, the hardness test is performed with a micro-hardness tester (Fig. 3-5). The load is 300g, and the loading duration is 30s. In order to avoid overlaps of strain area, each testing point is at least 0.5mm away from another.

Fig. 3-5 Micro-hardness tester (in Vickers' hardness)

In the case of cross-section hardness test, the testing area is very narrow, and the hardness marker is small. Thus, the surface of sample should be even smoother. Accordingly, the polished samples need further electronic polishing. The polishing solution is 80% methanol + 20% sulfuric acid in volume ratio, and the total volume of the solution is 200ml. The cross-section surface is kept 2cm away in parallel from the copper plate with the electronic solution sustaining at 0℃.

Electro-polishing (see Fig. 3-6) is carried out with a voltage of 17V and electrical current of 30mA for 60s. Sample is the anode and cooper plate is the cathode. Then the polished sample is rinsed in 300ml methanol and 100ml acetone. Small load of 25g is used with a loading duration time of 30s in cross-section hardness test. The distance between the nearby hardness indentations is about 15μm.

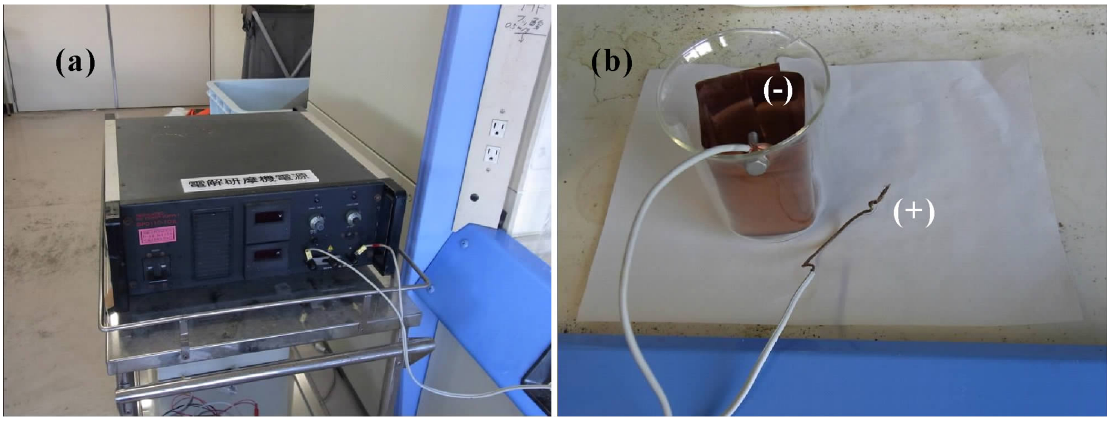

Fig. 3-6 Sketch of electronic polishing. (a) for electrical current, (b) for samples

3.3 Tensile Tests

Tensile properties are also important mechanical properties to indicate the performance of structural materials in service. In the present study, the tensile tests use SSJ specimens. Size of the tensile samples is shown as Fig. 3-7. Specimen of NIFS-HEAT-2 can be punch out from a mold as shown in Fig. 3-8. While in the case of mechanically alloyed material, the specimens are machined from the alloy bulk with wire cutting.

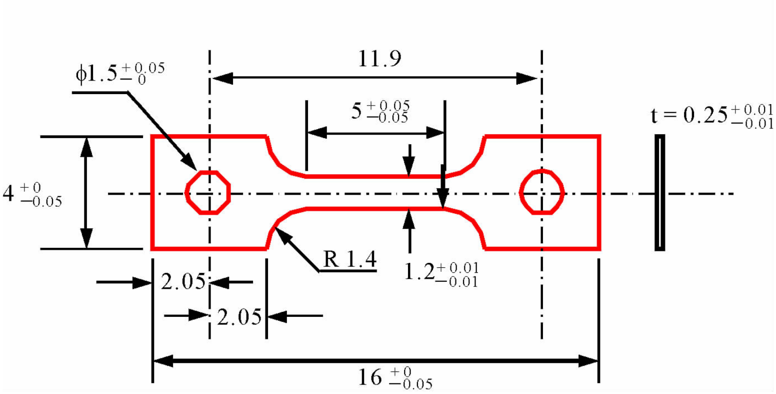

Fig. 3-7 Size of SSJ tensile/creep specimen

Tensile tests in the present study are carried out at room temperature as well as high temperature up to 700℃ and 750℃, because 700℃ is the designed operation temperature and 750℃ is the expected application temperature for V-4Cr-4Ti alloys in the future. The high temperature tests are performed in vacuum better than 1×10^{-6} torr in an INTESCO tensile tester (see Fig. 3-9) which equipped with a Ta heater. The strain rate for all the tensile tests is 0.2mm/min. When high temperature is used, the specimen is surrounded by a Zr foil to scavenge the O and N gases. Heating starts when the vacuum is lower than 1×10^{-6} Torr at a heating speed of 20℃ per minute. The tensile test starts at 15 min after the target temperature is achieved.

Yield stress is the most important tensile property in the present study to show the strengthening and to determine stress region for creep tests. Also, other properties as ultimate strength, uniform elongation and total elongation can be determined from the tensile curves.

Fig. 3-8 Punch mold for tensile/creep samples

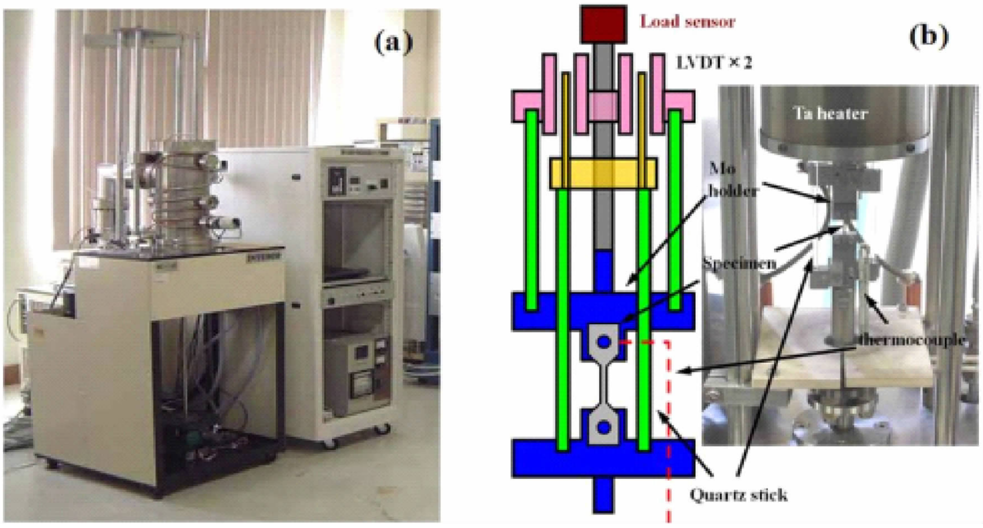

Fig. 3-9 tensile/creep tester (a) and schematic of tensile/creep tests

3.4 Creep Tests

Creep in mechanical engineering here means the deformation of material with a sustain load at elevated temperature. The load is less than the yield stress of the material at the testing temperature. Creep rate is an important parameter for structural materials used in high temperature environments. Material with lower creep rate is regarded as to own higher creep strength, and its lifetime in service is longer. The creep tests share the same machine and the same specimen size with tensile tests in the present study. During the creep tests, the specimen is surrounded by Zr getter foil, and the vacuum is better than 1×10^{-6} torr. During heating, a stress of 3-10MPa is loaded on the specimen to avoid compression when the specimen is expending with increasing temperature. The creep test starts when the temperature and outputs from the double linear variable differential transformer (LVDTs) are stable, which is usually about 6 hrs after the temperature achieves the set value.

Creep data are recorded as strain-time curves as shown in Fig. 3-10. In the present study, minimum creep rate is used to evaluate the creep strength. The minimum creep rate is determined as the minimum of the average creep rate for the secondary creep stage (Stage II in Fig. 3-10) depending on different test duration. Stresses of 100MPa and 280MPa are loaded on the creep specimens at 700-750℃ to study the creep mechanism for the V-4Cr-4Ti alloys.

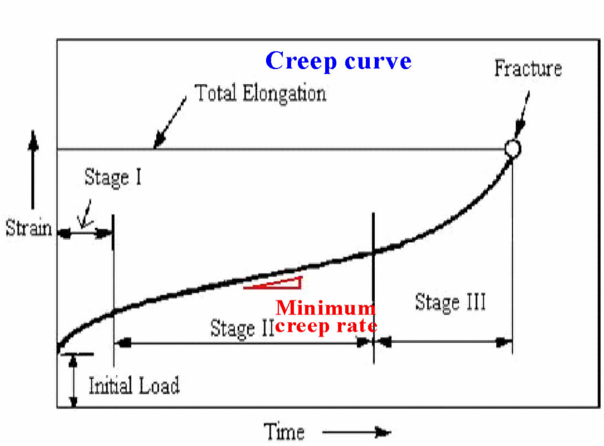

Fig. 3-10　Determination of minimum creep rate

3.5　SEM-EDX Observation.

In order to observe the surface morphology of specimens before and after tests, and in order to obtain the map of element distribution in an alloy, a scanning electron microscope (SEM) equipped with an energy-dispersive X-ray spectroscopy (EDX) is used in the present study. The SEM used is the type of JEOL (JSM-5600) as shown in Fig. 3-11.

Fig. 3-11　SEM (JSM-5600) with an EDX

For fracture surface of tensile specimens and metallic powder samples, the observation is carried out with a voltage of 20kV. The magnification of the SEM observation varies from 100 to 2000 times. Cross-section samples kept in a resin block are very small, and the resin part is insulating, which may cause charging up of the resin. So an electric coating is made before SEM observation. The coating is sprayed for 60s, and a layer of Au coating with the thickness of about 10 nm has covered the whole resin block. In the case of observation for grain size, the sample surfaces are etched at first. The etching solution is HNO_3 : HF : H_2O = 1 : 1 : 2 in volume ratio and the etching temperature is kept at 0℃. After 30-60s etching with ultrasonic vibrations, the samples are then rinsed in 300ml methanol.

EDX analysis for the alloys in bulk samples uses a TEM sample with the size of Φ3mm × 0.25mm. For powder samples, a carbon tape about 5mm × 5mm is used to hold the powders. Magnification varies from 100 to 500 times is applied to show the distribution of each alloying element such as Cr, Ti, Y and W impurity in sample preparation process.

3.6 TEM Observation

In order to observe the precipitate size and distribution as well as dislocation distribution, a JEOL-2000 FX type transition electron microscope (TEM) as shown in Fig. 3-12 is used. For sample preparation, theΦ3 × 0.25mm specimens are electropolished with the solution of 80% methanol + 20% sulfuric acid in volume ratio. Then the resulted film samples are observed in the TEM with an operation voltage of 200kV.

Fig. 3-12 TEM equipment (JEOL-2000 FX)

Two beam images are used to calculate the sample thickness and thus volume of a selected area. The calculation uses an extinction distance of about 45nm for vanadium. Precipitates and dislocations are characterized by this TEM.

EDX in TEM machine is also used to analyze the compositions of the sample matrix and nano-particles.

3.7 XRD analysis

In the present TEM observation, some particles are too small to be analyzed by EDX, thus the structures and compositions can hardly be detected. An X-ray diffraction (XRD) as shown in Fig. 3-13 is used to characterize the presence of secondary phases beside the matrix. During mechanical alloying, peak shift of the matrix material is also evaluated by XRD to show its lattice parameter change. As to the operation parameters, the operation voltage varies from 40kV to 60kV, and the electron current is 50mA. As to the other parameters, the divergence slit is 0.2mm; the scattering Slit is 0.2 ~ 1mm; the receiving Slit is 0.15 ~ 1mm; and the scan speed is 0.2°/min.

Fig. 3-13 XRD equipment

CHAPTER 4

Thermo-mechanical strengthening of V-4Cr-4Ti alloy

4.1 Theory

Structural materials are usually expected to have both high strength and acceptable ductility. Thus, they can sustain high load and have much allowance for deformation. Nowadays, many ways have been developed to strengthen a material and there are also some ways to make a material ductile. However, for metals, there is usually a tradeoff between strength and ductility. How to balance between strength and ductility is an important issue. For this concern, a simple process called "thermo-mechanical treatment" is widely applied on the metal being tested.

The thermo-mechanical treatment (TMT) is a combined process of cold working and heat treatment. The heat treatment usually includes solid-solution hardening and precipitation hardening [128]. Techniques for TMT have been commercially mature and are available for various materials. Generally, cold working which introduces high density of dislocations is used for work hardening. When it is needed to improve the ductility, an annealing can be considered as an approach. On the other hand, aging (a kind of heat treatment) which produces high number density of precipitates is used for precipitation hardening. The solid-solution prior to precipitation also needs to be completed with heat treatment, and it can recover ductility of the material again after precipitation hardening. So, taking one with another, thermo-mechanical treatment is an efficient way to control the balance of mechanical properties for a metal.

Work hardening is based on the interactions between dislocations. It can be described by following Bailey-Hirsch equation (4-1):

$$\Delta\tau = \alpha \cdot \mu \cdot \boldsymbol{b} \cdot \Delta\rho^{1/2} \tag{4-1}$$

Where, indicates the change in shear stress of a material; α is a constant; μ is the shear modulus of a determined material (46.7GPa for V-4Cr-4Ti alloy); $\boldsymbol{b}$ is Burgers vector of the material (0.26nm for V); and ρ is the area number density of dislocations in the material ($/\mathrm{m}^2$).

Since yield stress can be evaluated by the shear stress at a certain temperature and strain rate. So the yield stress of the material increases with the increasing dislocation number density.

The equation (4-1) can be converted to indicate hardness as equation (4-2):

$$\Delta \mathrm{Hv} = \alpha' \cdot \mu \cdot \boldsymbol{b} \cdot \Delta\rho^{1/2} \tag{4-2}$$

α' is a constant which can convert shear stress into hardness.

Precipitation strengthening is based on the interactions of dislocations with precipitates. It can be described by following equation (4-3).

$$\tau = \frac{\sqrt{3}}{(2\pi)^{\frac{3}{2}} \cdot K} \cdot \frac{G \cdot b \cdot f^{\frac{1}{2}}}{r} \cdot \ln \frac{l}{2r_0} \approx \beta \cdot f^{\frac{1}{2}} \cdot r^{-1} \tag{4-3}$$

Where G is shear modulus, K is a constant related to inherent conditions of dislocation, b is Burgers vector, f is the volume fraction of particles to material, r is average radii of particles, l is the average distance between particles nearby, β is a constant and r_0 is the radius of dislocation core. When volume fraction is determined, to reduce the size of precipitates can be regarded as to increase the number density in a determined volume, and which will finally increase the yield stress.

The equation (4-3) can be converted to equation (4-4) to calculate the hardening:

$$\Delta Hv \approx \Delta \sqrt{N_v \cdot d} \cdot C' \cdot M \cdot \alpha'' \cdot \mu \cdot b \qquad (4\text{-}4)$$

Where, N_v is number density of particles in a determined volume, d is average diameter of the particles, these two parameters can be measured in experiments. "C'" is a constant, "M" is Taylor factor, "μ" is shear modulus and "$\boldsymbol{b}$" is Burgers vector with values of 3, 3Hv/9.8MPa, 46.7GPa and 0.26nm for vanadium, respectively. "α''" is assumed to be 0.3, which is barrier strength of the particles to dislocations.

In the case of high temperature application, metallic materials will become softer very much. Thus more strengthening is required beforehand on the material. Moreover, it is also important to stabilize the strength of the material at high temperature. Combining work hardening and precipitation hardening through thermo-mechanical treatment is an attractive idea for strengthening metals. The combination can be completed in two different orders. One is to do precipitation hardening first and then do work hardening . Another is to do work hardening at first, then followed by precipitation hardening. Since dislocations caused by cold working can partly be recovered by post aging, the microstructures and yield stress related to these two different types of combination could be different. Moreover, the kinetic conditions will be changed by precipitation after cold working, thus the stability of strengthening for each way of combination may also be different.

Based on the above considerations, this paper focuses on the study of creep resistance of V-4Cr-4Ti alloy through the use of work hardening and precipitation hardening in two different orders.

4.2 Experimental

4.2.1 Preparation of material and chemical compositions

The main material used in the present study is from a 4mm-thick plate of NIFS-HEAT-2 which is a 166kg V-4Cr-4Ti alloy ingot [129]. The ingot was fabricated with Vacuum Arc Remelting (VAR) technology with some improvements in protective atmosphere. Then the ingot was canned into a case made of SS304 stainless steel for hot forging and hot rolling to obtain some alloy plates. Finally, a cold rolling was applied on the V-4Cr-4Ti alloy plates.

A reference V-4Cr-4Ti alloy, which is a 200g-ingot designated as SWIP-11, which contains more O impurities is introduced to investigate the effect of impurities on mechanical properties of V-4Cr-4Ti alloy. This alloy was fabricated with Vacuum Induction levitation Melting (VIM). The post-treatments for SWIP-11 are similar to those for NIFS-HEAT-2. Main chemical compositions including alloying elements and non-metallic impurities for NIFS-HEAT-2 and

SWIP-11 are listed in Table 4-1. Note: For the impurities in SWIP-11, only concentration levels of carbon C, O and N are available.

Table 4-1 Chemical composition of the used V-4Cr-4Ti alloys.

	Alloying Elements (wt%)			**Impurities (wppm)**					
	V	Cr	Ti	C	O	N	Al	Si	Fe
NIFS-HEAT-2	Bal.	4.02	3.98	67	148	122	59	270	49
SWIP-11	Bal.	3.76	4.05	110	570	10			

4.2.2 Thermo-mechanical treatments

The method of combining work hardening and precipitation hardening is used to strengthen V-4Cr-4Ti alloys in this study. Solid solution annealing followed by two different orders of cold working and aging are the main technologies used in strengthening. A reference treatment, standard heat treatment for NIFS-HEAT-2, is used to contrast the strengthening of the above thermo-mechanical treatments. The detailed treatments are as follows:

(1) Standard heat treatment (STD) is used for recrystalization and recovery from cold working. This treatment is carried out at 1000℃ for 2 hrs.

(2) Work hardening after precipitation hardening. A pre-solid solution annealing is carried out at 1100℃ for 1 hr. Then, an aging process at 600℃ for 20 hrs was carried out to produce precipitates. Finally, a cold working was performed by reducing 20% thickness of the plate to obtain high density of dislocations. The above treatment can be summarized as solution annealing plus aging and then cold working, which is called SA + A + CW method (or SAACW) in this paper.

(3) Work hardening followed by precipitation hardening. All treatment conditions are the same as those for SAACW. While, in case the pre-solid solution annealing before precipitation can make recovery from cold working, the cold working was carried out just after solid solution annealing was done, and finally the aging was performed. Thus, the route for this treatment is solution annealing plus cold working and finally plus aging, called SA + CW + A (or SACWA) in this study [130]. This treating route might have been used for other materials, however, the present study, for the first time, uses SACWA to improve creep strength of V-4Cr-4Ti alloy.

A schematic illustration for the above description is shown in Fig. 4-1 below. As for each alloy, the arrangements of thermo-mechanical treatments are listed in Table 4-2. Note: SWIP-11 has no SAACW treatment.

It is worth noting that most experiments for SAACW were carried out by Professor Chen [131]. This study takes his data for comparison purpose, only limited data of SAACW are obtained in the present study.

Table 4-2 Arrangement of thermo-mechanical treatments for each alloy

	Treatments		
NIFS-HEAT-2	STD	SAACW	SACWA
SWIP-11	STD		SACWA

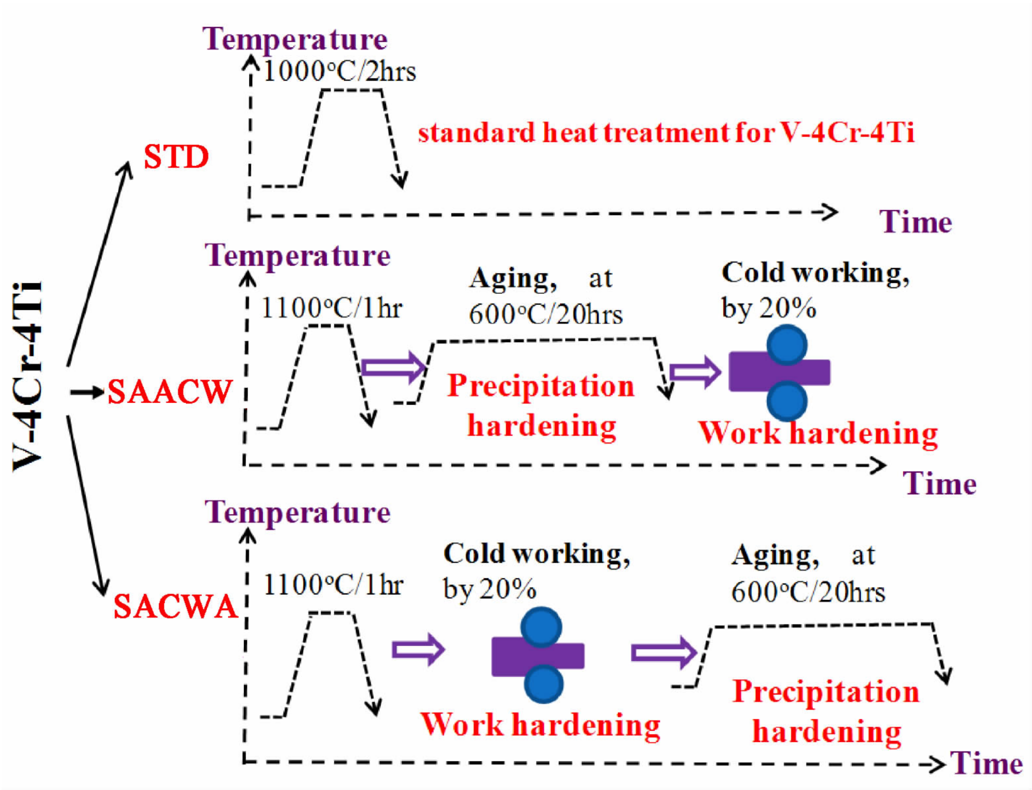

Fig. 4-1 Schematic illustration of thermo-mechanical treatments for V-4Cr-4Ti alloys

4.2.3 Mechanical property tests

As NIFS-HEAT-2 is the main material for the present study, most tests about mechanical property are applied on this material.

Hardness is tested with a load of 300g and a testing duration of 30s. Tensile tests are carried out at 700℃ which is the designed operating temperature, and also at 750℃ which is the expected temperature in the future. Tensile tests are performed in order to determine the yield stresses of STD, SAACW and SACWA. SSJ specimens are used for the tensile tests in a vacuum. Each yield stress is determined as 0.2% proof stress. Then the uniaxial creep tests for the V-4Cr-4Ti alloy in STD, SAACW and SACWA states are carried out under the conditions listed in Table 4-3. Yield stresses of these samples at 700℃ and 750℃ are also listed. According to this table, creep tests for SACWA and SAACW are conducted below their yield stress levels, while some of the creep tests for STD are performed beyond its yield stress.

Table 4-3 Conditions of uniaxial creep tests for V-4Cr-4Ti alloys.

Material	State	Temperature	Yield Stress	Applied Stress (MPa)						
NIFS-HEAT-2	STD	700℃	241 MPa	100	140*	203*	222*	240*	280	290*
		750℃	200 MPa	100	180	230	280			
	SAACW	700℃	451 MPa	100	214*	240*	263*	287*	308*	
		750℃	418 MPa	100	176*	214*	240*	263*		
	SACWA	700℃	418 MPa	100	180	230	280			
		750℃	393 MPa	100	180	230	280			
SWIP-11	STD	750℃	——	180	230	280				
	SACWA	750℃	——	180	230	280				

* marked data were published in Ref. [131].

4.2.4 Microstructure observations.

TEM observation has been performed at each step of the thermo-mechanical treatments for SAACW and SACWA to indicate microstructural evolutions. SA is the pre-treatment for them both. SAA is the pre-treatment for SAACW, and SACW is the pre-treatment for SACWA.

The details of these pre-treatments are as follows:

SA: Solid solution annealing at 1100℃ for 1hr.

SAA: SA + aging at 600℃ for 20hrs.

SACW: SA + 20% cold working.

4.3 Mechanical Properties

4.3.1 Hardness evolution of different thermo-mechanical treatments

Hardness is a property which can be used to evaluate hardening quickly. So hardness test is arranged prior to other mechanical property tests. Figure 4-2 shows the comparison of hardness change for V-4Cr-4Ti alloys between thermo-mechanical treatments and standard heat treatment (STD). In Fig. 4-2 (a), the pre-solid solution annealing (SA) hardens the NIFS-HEAT-2 alloy a little. Cold working (SACW) and aging (SAA) can introduce more obvious hardening. Then, cold working after aging (SAACW) or aging after cold working (SACWA) hardens the alloy further. Finally, the hardness of SAACW and SACWA are similar. In Fig. 4-2 (b), different materials with same SACWA treatment are compared. Their trends of hardening are similar, though the hardness of NIFS-HEAT-2 and SWIP-11 in STD states are different, the hardness in SACWA state for these two different alloys are almost the same.

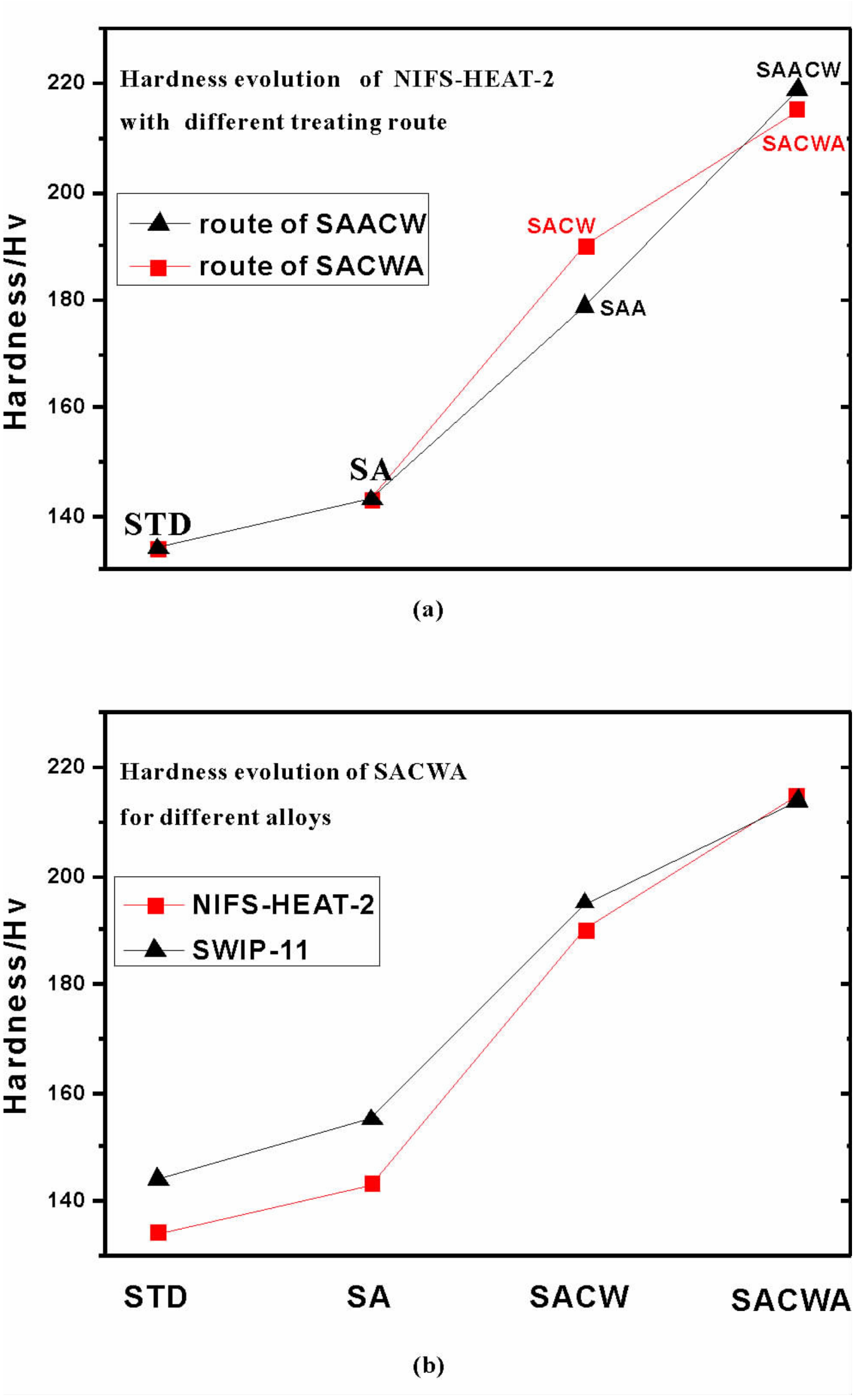

(a)

(b)

Fig. 4-2 Hardness evolution of (a) NIFS-HEAT-2 with SAACW compared with SACWA, and (b) hardness evolution of SACWA for NIFS-HEAT-2 compared with SWIP-11

4.3.2 Tensile properties of NIFS-HEAT-2 with different thermo-mechanical treatments

Tensile properties are important parameters to determine the design criteria of structural components. Fig. 4-3 shows the determination of yield strength (YS), ultimate strength (UTS), uniform elongation (UE) and total elongation (TE). Among these properties, yield strength is the most important parameter in the present study.

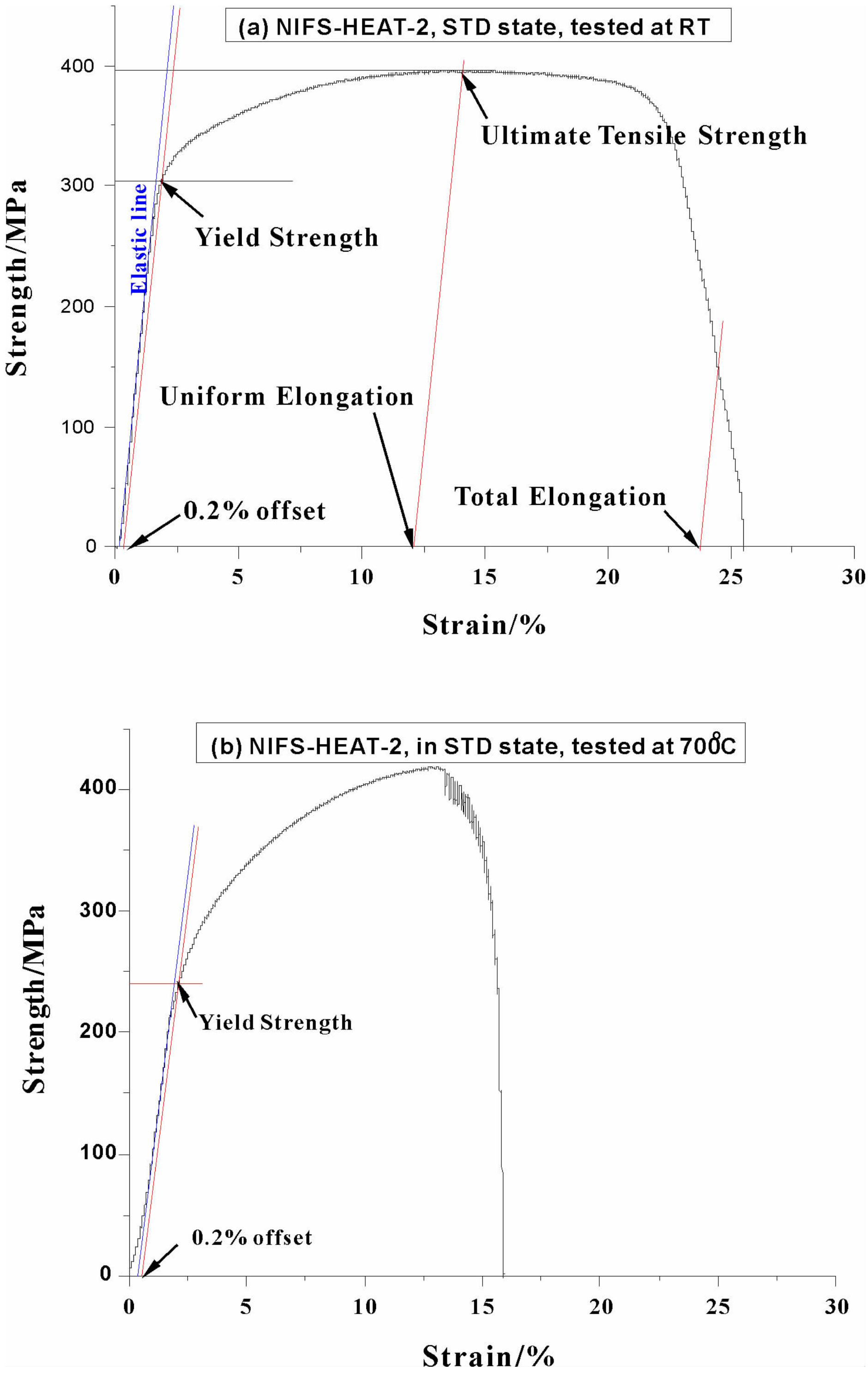

Fig. 4-3 Example of tensile curves for NIFS-HEAT-2 in STD state at (a) RT and (b) 700℃

Figure 4-4 shows the tensile properties including YS, UTS, UE and TE for V-4Cr-4Ti alloy (NIFS-HEAT-2) at RT, 700℃ and 750℃. It is clear that the thermo-mechanical treatments SAACW and SACWA both strengthened the V-4Cr-4Ti alloy, no matter if it is at RT or high temperatures.

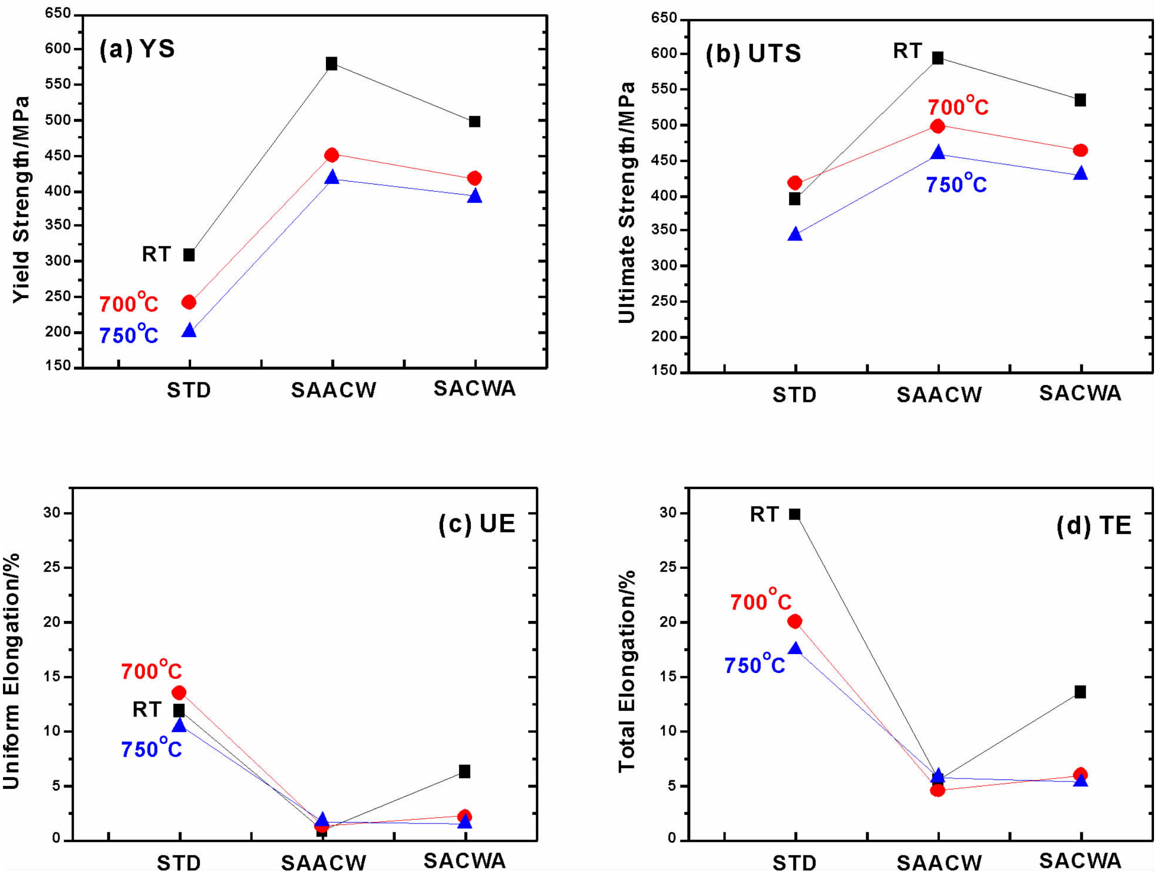

Fig. 4-4 RT and 700℃ tensile properties as YS

(a), UTS (b), UE (c) and TE (d) of V-4Cr-4Ti alloy (NIFS-HEAT-2)

4.3.3 Creep properties of NIFS-HEAT-2 with different thermo-mechanical treatments

The creep deformation is recorded in strain-time curves in this study. Fig. 4-5 shows an example of creep curves for V-4Cr-4Ti alloy (NIFS-HEAT-2) in SACWA state at 700℃ and 750℃.

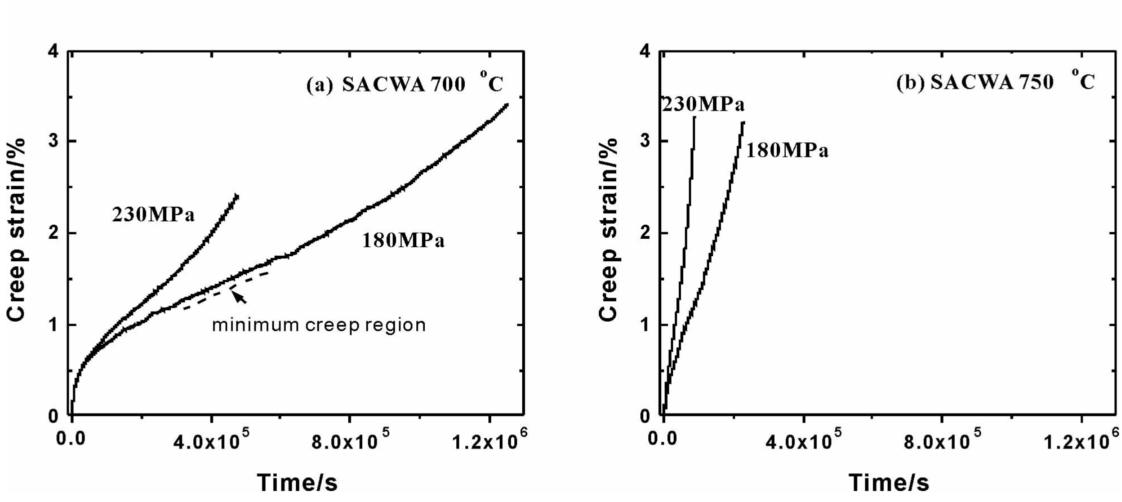

Fig. 4-5 Example of creep curves for NIFS-HEAT-2 in SACWA state at (a) 700℃ and (b) 750℃

It is clear that, within the same creep time, higher stress leads to higher creep strain rate at the same temperature, and higher temperature leads to higher creep strain rate under same stress. Minimum creep rate is calculated from the secondary deformation region, as shown in Fig. 4-5 (a).

The dependence of the minimum creep rate on applied stress for SACWA, STD and SAACW at 700℃ and 750℃ is shown in Fig. 4-6. Note data with open symbols are referred from [131].

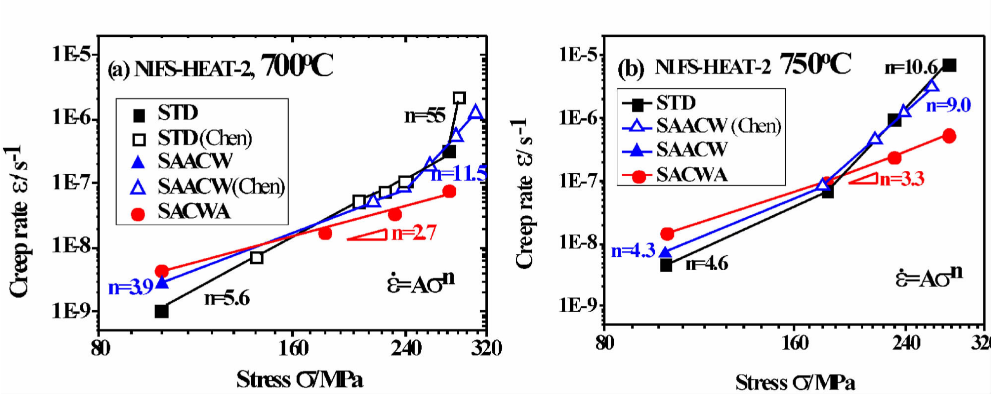

Fig. 4-6 Dependence of the minimum creep rate on applied stress for SACWA, STD and SAACW at (a) 700℃ and (b) 750℃

Most creep data in Fig. 4-6 are fitting to equation (4-5) [132]:

$$\dot{\varepsilon} = A\sigma^{n}\exp(-Q_a/RT) \tag{4-5}$$

Where $\dot{\varepsilon}$ is the minimum creep rate;

A is a constant;

σ is the applied stress;

n is the stress exponent;

R is the gas constant;

T is the absolute temperature; and,

Q_a is the apparent activation energy of creep [133]. According to the fitting, the stress exponent "n" for SACWA is 2.7 at 700℃ and 3.3 at 750℃, respectively, at all the stress levels examined. For STD, "n" is 5.6 under stress below about 240MPa at 700℃ and 4.6 under stress below 180MPa at 750℃, respectively. In the same stress region, the estimated value of "n" for SAACW is 3.9 and 4.3 at 700℃ and 750℃, respectively. Above about 240MPa, "n" value changes to 55 at 700℃ for STD; and above 180MPa, "n" value changes to 10.6 at 750℃ for STD. Similar trend happens to SAACW, its "n" value changes to 11.5 above 240MPa at 700℃ and 9 above 180MPa at 750℃, respectively. According to Fig. 4-6, the curve of creep rate for SACWA crosses with that for STD and SAACW around 180MPa, SACWA has the highest creep rate in low stress region, and when it is probably over 180MPa, SACWA exhibits the lowest creep rates.

The apparent activation energy of creep, Q_a, can be obtained from the slope of the plot of $\ln\dot{\varepsilon}$ vs. $1/T$. The plots for creep activation energy of STD, SAACW, and SACWA at 700℃ and 750℃ are shown in Fig. 4-7. Assuming the minimum creep rate $\dot{\varepsilon}$ is equivalent to the steady-state creep rate, the creep activation energy can be calculated with equation (4-6) [133]:

$$Q_a = R(\ln\dot{\varepsilon}_1 - \ln\dot{\varepsilon}_2)/(1/T_1 - 1/T_2) \tag{4-6}$$

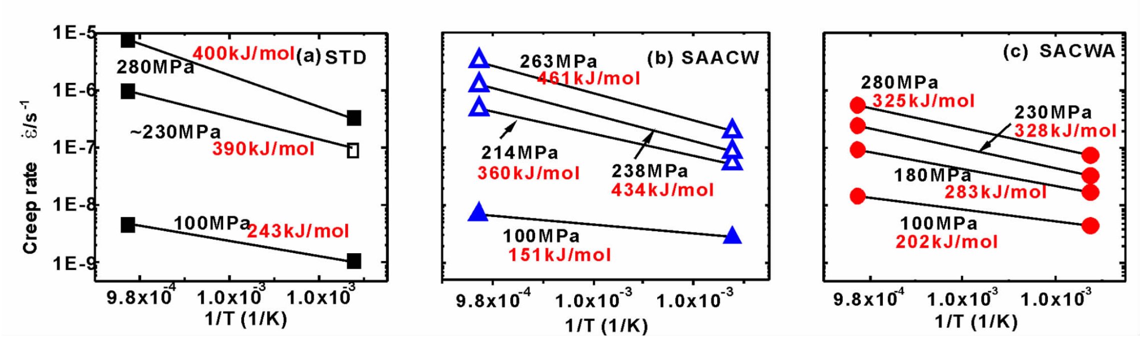

Fig. 4-7 Determination of creep activation energy for STD (a), SAACW (b) and SACWA. Note: data with open symbols are from [131]

The estimated creep activation energy of SACWA is 202 ~ 328 kJ/mol at all stress levels examined, with an average value of 283kJ/mol, which is near the self-diffusion activation energy of vanadium (about 270kJ/mol) [133, 134]. For STD at 100MPa, the estimated creep activation energy is 243kJ/mol. For SAACW at 100 ~ 214MPa, the average value is ~256kJ/mol, which is also similar to the self-diffusion activation energy of vanadium.

On the other hand, the estimated creep activation energy is 390 ~ 400 kJ/mol for STD at 230 ~ 280MPa and 434 ~ 461 kJ/mol for SAACW at 238 ~ 263MPa, respectively, which are much higher than the self-diffusion activation energy of vanadium.

4.3.4 Creep properties of NIFS-HEAT-2 compared with those of SWIP-11.

Figure 4-8 shows the comparison of creep rates of NIFS-HEAT-2 comparing with SWIP-11, both are in STD (a) and SACWA (b) states.

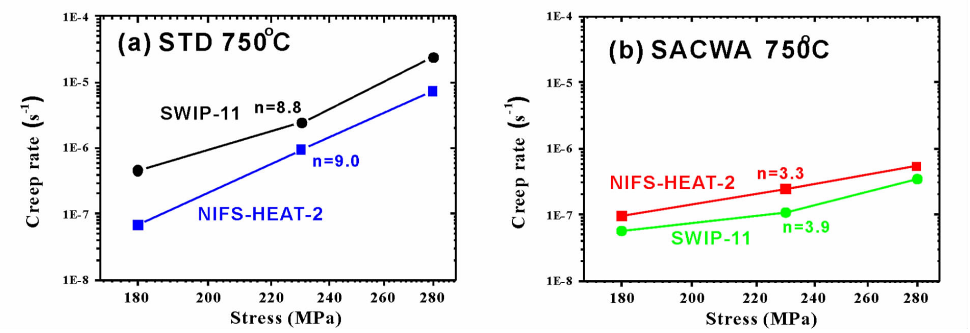

Fig. 4-8 Comparison of creep rates of NIFS-HEAT-2 with SWIP-11 in STD (a) and SACWA (b) states at 750℃

Same data are plotted in Fig. 4-9 to show the comparison of creep rates of NIFS-HEAT-2 (a) and SWIP-11 (b) between STD state and SACWA state. The test temperature is 750℃, and the stresses are mostly above 180MPa. In STD state (See Fig. 4-8(a)), NIFS-HEAT-2 shows lower creep rate than SWIP-11. However, in SACWA state (See Fig. 4-8(b)), NIFS-HEAT-2 shows higher creep rate than SWIP-11. In the case of same treatment for SWIP-11, there is similar trend to NIFS-HEAT-2. In Fig. 4-9(a) and (b), SACWA shows lower creep rates than STD mostly, and the differences are more notable for SWIP-11 than for NIFS-HEAT-2.

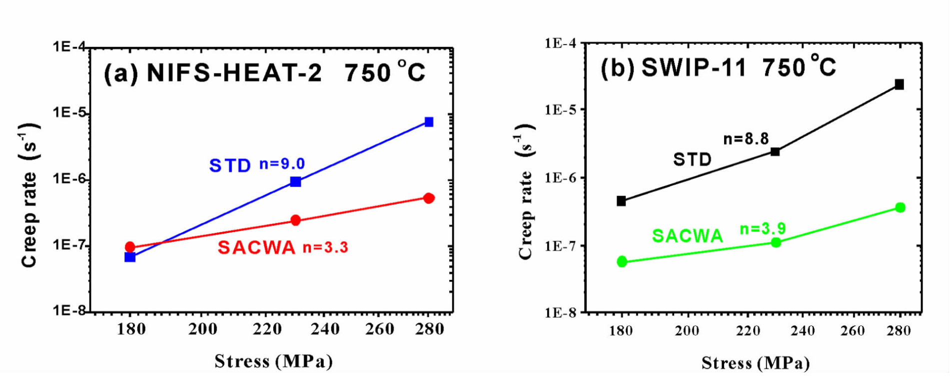

Fig. 4-9 Comparison of creep rates of NIFS-HEAT-2 (a) with SWIP-11 (b) in STD and SACWA states at 750℃

4.4 Microstructures

In Fig. 4-6, STD and SAACW have similar creep behavior but much difference in hardness (Fig. 4-2) and yield stress (Table 4-3). In contract, hardness and yield stress in SAACW state and SACWA state are very similar, however the creep behavior (Fig. 4-6) in SAACW state and SACWA state are very different. All these properties depend on microstructure of the material very much.

Fig. 4-10 shows the evolution of microstructures in STD, SAACW and SACWA. Fig. 4-10 (a) is for STD, where the matrix has extremely low density of dislocations, and low number density of precipitates except for some inclusions. After solid solution annealing (SA as shown in Fig. 4-10(b)), the dislocation number density is keeping extremely low. Aging produces high number density of precipitates (estimated to be $2.18\times10^{22}/m^3$) for SAA in Fig. 4-10(c). These precipitates are considered to be Ti-(C,O,N) interstitial composites. The following cold working introduces a high number density of dislocations (up to $3.54\times10^{14}/m^2$) as shown in 4-10(d) which is SAACW. While in the case of SACWA, the cold working is ahead of aging. This cold working introduced a dislocation density of $3.8\times10^{14}/m^2$ to SACW. While after final aging, this value decreased to $1.6\times10^{14}/m^2$ for SACWA. Precipitates are not confirmed in the present observation conditions for SACWA because of the overlapping of dislocations.

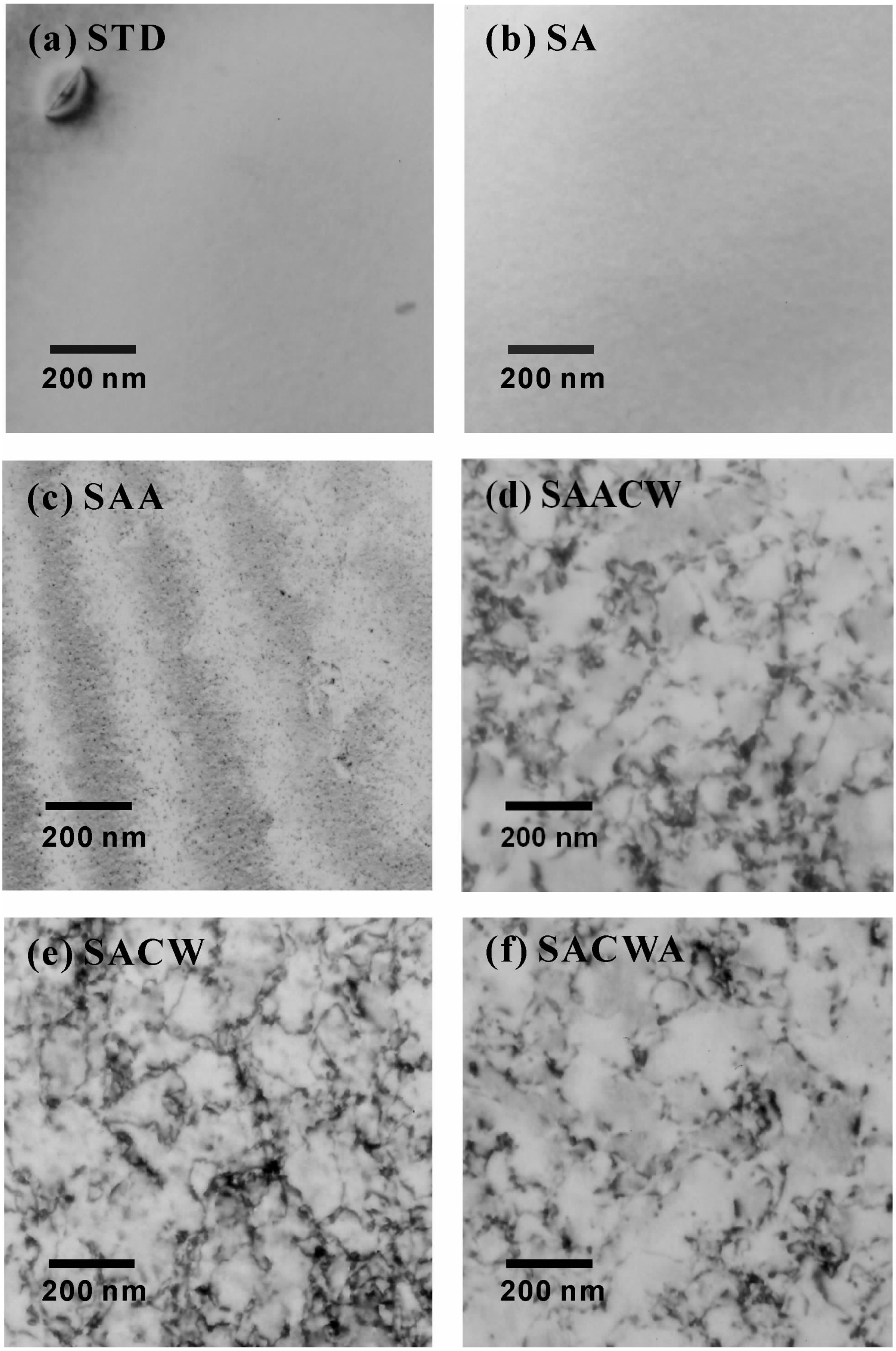

Fig. 4-10 Evolution of microstructures in V-4Cr-4Ti alloy (NIFS-HEAT-2) for SAACW ((b),(c), (d)) and SACWA ((b), (e), (f)) compared with STD (a)

However, in XRD analysis as shown in Fig. 4-11, TiO, TiN and VC peaks are observed beyond V peaks for both matrices.

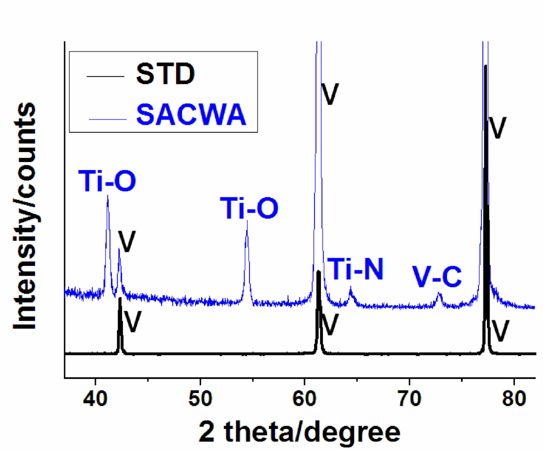

Fig. 4-11 Comparison of phases for NIFS-HEAT-2 in SACWA and STD states

4.5 Discussion

4.5.1 Hardening by thermo-mechanical treatments.

STD is a reference treatment in the present study, the microstructures of this state are considered to contain the fewest defects such as interstitial atoms, dislocations and interfaces of different phases. The solid solution annealing accommodates the N, O and C interstitial impurities. The lattice distortion caused by the accommodation of these impurities will then resist dislocation motion, thus hardens the alloy, as shown in Fig 4.2 (a). The V-4Cr-4Ti alloy in SA state is harder than that in STD state.

On the other hand, solubility of N, O and C impurities in V matrix is limited, which can be referred from binary-phase diagram of V-N, V-O and V-C systems as shown in Fig. 4-12 (a), (b) and (c), respectively. In the (V) state, detailed limiting values at RT are about 0.75% for N and 3.6% for O in atomic ratio, respectively [135]. Though the solubility of N and O in V-Ti system cannot be directly estimated from the V-N and V-O phase diagrams, rough estimation of the impurity concentrations of N and O in either NIFS-HEAT-2 or SWIP-11 are considered to be within the solid solution range at RT, because the V-Ti system can also accommodate a lot of N and O impurities. So solid solution of these 3 kinds of impurities can roughly account for the hardening of SA.

The hardening ability of interstitial impurities can actually be estimated from an empirical formula as shown below (4-7):

$$\Delta Hv = \alpha''' \cdot C'' \qquad (4\text{-}7)$$

Where, α''' is a constant, and C'' is the concentration of impurities. For C, constant α''' can be referred from Fig. 4-13 below, which is published in [136]. For N and O, this value is 0.008Hv/wppm and 0.042 Hv/wppm in SA state, respectively.

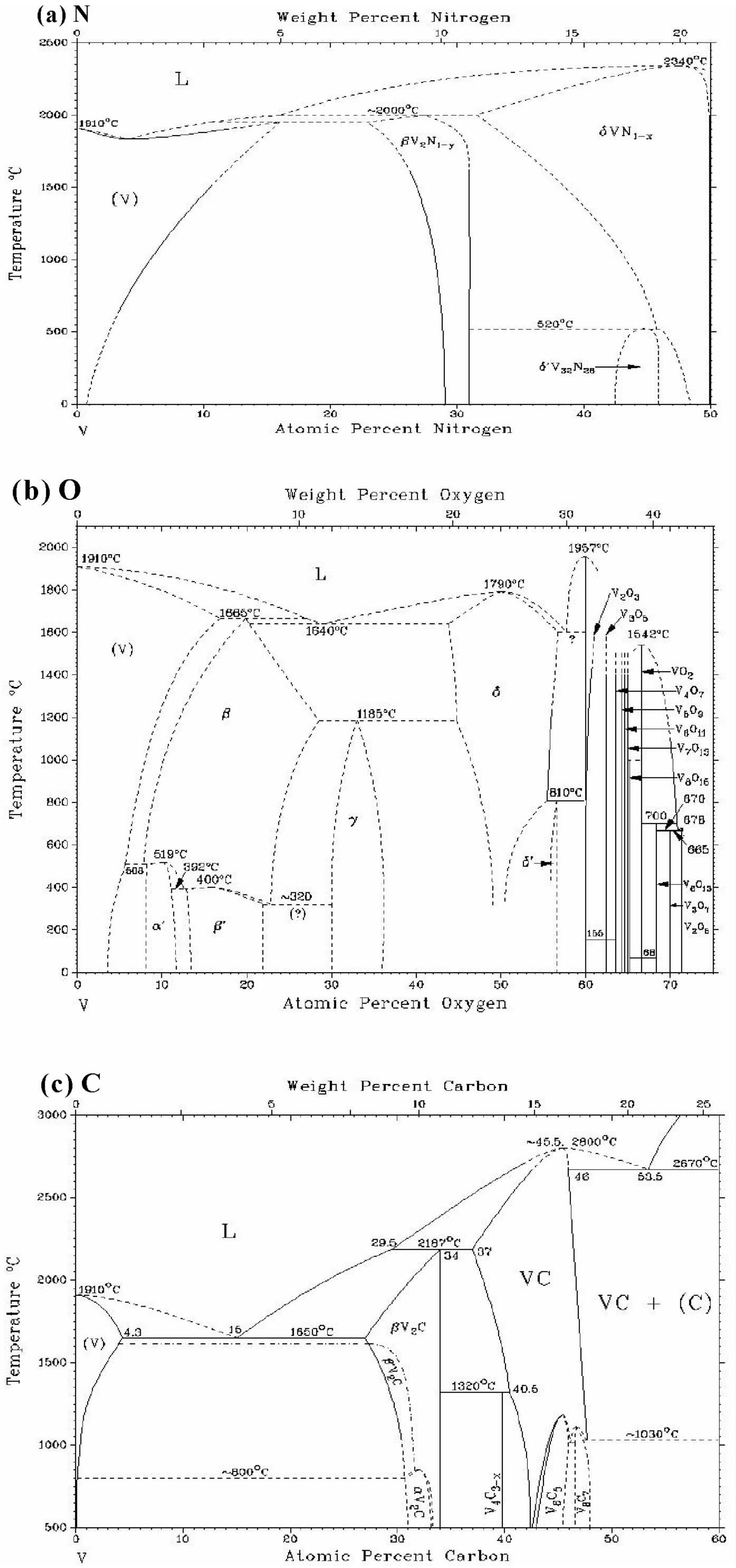

Fig. 4-12 Phase diagrams of V-N (a), V-O (b) and V-C (c) systems [135]

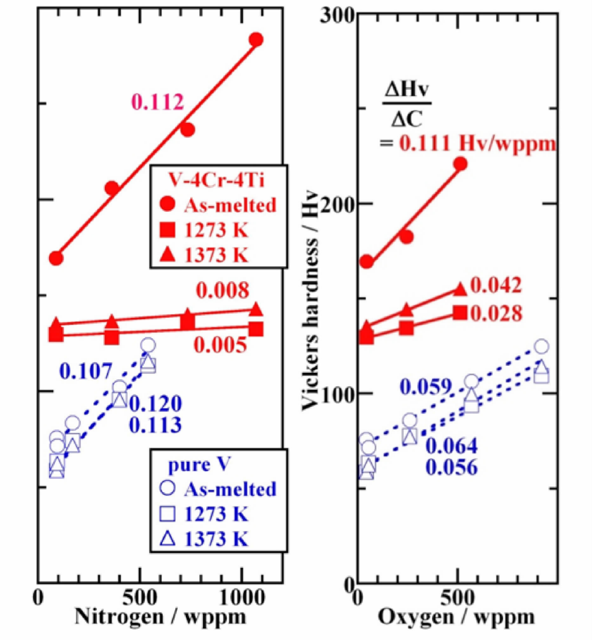

Fig. 4-13 Ability of solid solution hardening by N and O for vanadium and V-4Cr-4Ti alloy [136]

Data base for C is limited because C has relatively low solubility in vanadium. Little C content can be retained in solid solution. However, C is a potent solid-solution hardener. A previous study [75] showed that the tensile strength of an electro-refined vanadium increases with C content to a peak value, and then decreases with further increase in C content. The initial increase in strength at low-carbon level is due to the fact that there is carbon in solid solution. At higher C level, when carbides formed, the strength decreases and then remains constant, even though there is further increase in C content in the material. The illustration of this process can be seen in Fig. 4-14 below.

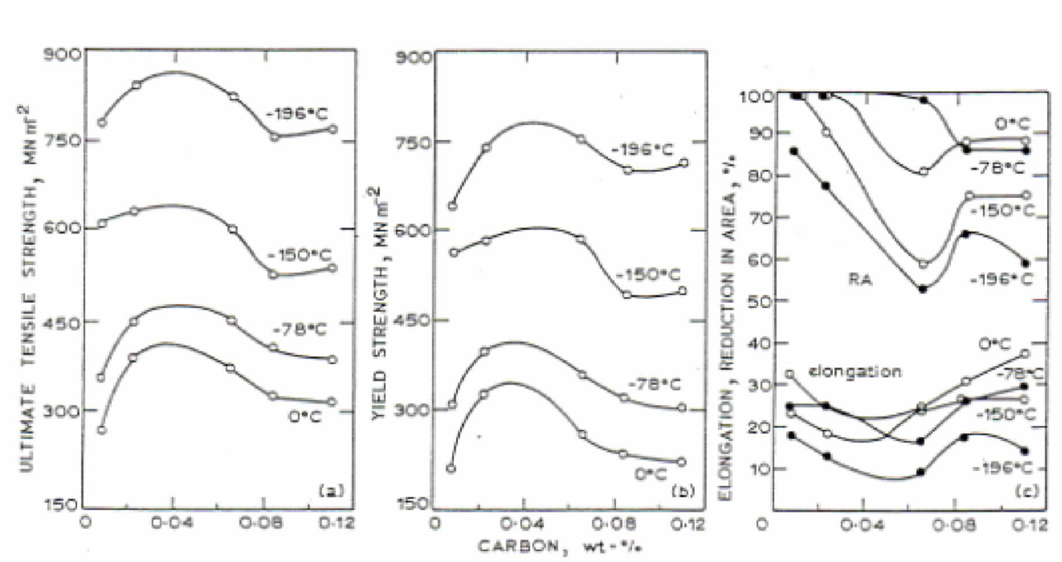

Fig. 4-14 Effects of Carbon content on tensile strength of electro-refined vanadium [75]

Although less potent in precipitation hardening, carbides are also effective strengtheners at low temperatures. The proper dispersion is developed and this requires suitable control of both C content and heat treatment. Little is known about the effectiveness of carbides at high temperatures. Roughly say, C is about half as potent as O in the present estimation [75], assume to be 0.021 Hv/wppm in SA state.

Accordingly, the calculation of solid solution hardening contributions of N, O and C to NIFS-HEAT-2 in SA state relative to standard heat treatment (STD) are listed in Table 4-4, assuming most impurity atoms are in inclusions for STD and have dissolved as interstitial atoms for SA. It seems that the calculated value (~8.6) is approximately the same as the measured value (~9.0).

Table 4-4 Solid solution hardening contributions of N, O and C for to V-4Cr-4Ti alloy (NIFS-HEAT-2)

NIFS-HEAT-2 (SA)			
Solutes	C	O	N
Concentration C'' (wppm)	67	148	122
α''' value (Hv/wppm)	0.021	0.042	0.008
Hardening contribution (Hv)	~1.4	~6.2	~1
Total hardening calculated (Hv)		1.4 +6.2 +1 =8.6	
Total hardening measured (Hv)		~9.0	

Both aging and cold working are effective to harden the V-4Cr-4Ti alloys. In SAA state, NIFS-HEAT-2 has a precipitate number density of $2.18 \times 10^{22}/\ m^3$. The mean size of these extremely fine precipitates is estimated to be 5nm. The distribution state is as shown in Fig. 4-15. According to equation (4-2), the hardening caused by these precipitates is estimated to be 34.9Hv, which is similar to the measured value of 36.0Hv.

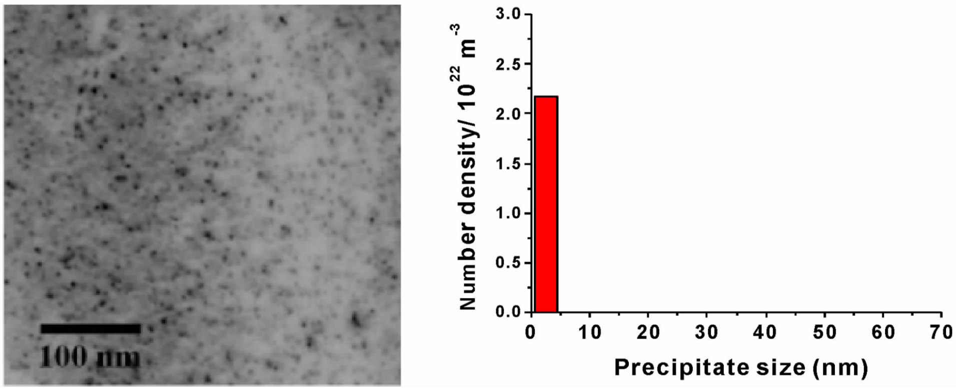

Fig. 4-15 Size distributions of precipitates in SAA state NIFS-HEAT-2 alloy

According to equation (4-2), the hardening from SA to SACW contributed by cold working is 72.4Hv. To compare it with the measured value of 47Hv, this estimation is still reasonable. From SAA to SAACW, the hardening contributed by increase in dislocation is calculated to be 69.9Hv. To compare it with the measured value of 40Hv, this estimation is still reasonable.

The combined work hardening followed by precipitation hardening (SACWA) is a little complex as the precipitates are too small to observe under present observation condition and the interaction between the precipitates and dislocations is also unclear. However, the hardening is finally measured to be pretty similar as that in SAACW.

The above hardening trend of SAACW for NIFS-HEAT-2 is also expected to exist in SWIP-11, as the mechanism is the same and the two materials are quite similar. The only difference is that SWIP-11 contains higher total impurity concentration than NIFS-HEAT-2 does. However, this difference in impurity concentration again agrees with the difference in solid solution hardening as shown in Table 4-5. To compare SWIP-11 in SA state with that in STD state is not favored, because SWIP-11 in STD state has a lot of inclusions in the matrix. Therefore, this study just shows the comparison of hardening for SWIP-11 in SA state with that for NIFS-HEAT-2 in STD state.

Finally, NIFS-HEAT-2 and SWIP-11 have similar hardness in SACWA state as Fig. 4-2 (b) shows. This may indicate that the combined hardening ability of work hardening together with the following precipitation hardening is common for V-4Cr-4Ti alloys containing similar chemical compositions. Formation and coarsening of precipitates seem to be resisted by the dislocations. Details of such resistance is unclear in the present study, but worth investigating in the future.

Yield stress of NIFS-HEAT-2 has similar hardening trend for SAACW and SACWA states, both at RT and high temperatures, like what Fig. 4-4 (a) shows. In this method, the yield stress of V-4Cr-4Ti alloy is considered to be increased, and enhances the resistance to deformation.

Table 4-5 Contribution of N, O and C to solid solution hardening for V-4Cr-4Ti alloy (SWIP-11).

SWIP-11 (SA)			
Solutes	C	O	N
Concentration C'' (wppm)	110	570	10
α''' value (Hv/wppm)	0.021	0.042	0.008
Hardening contribution (Hv)	~2.3	~23.9	~0.1
Total hardening calculated (Hv)	2.3 + 23.9 + 0.1 = 26.3		
Total hardening measured (Hv) relative to STD of NIFS-HEAT-2	~21.0		

4.5.2 Creep Mechanisms of Thermo-Mechanically Strengthened V-4Cr-4Ti Alloy

In the present study, the two thermo-mechanical treatments, SAACW and SACWA enhanced the creep resistance of V-4Cr-4Ti alloy at stresses higher than 180MPa compared with STD, and, especially at lower temperature, as what shows in Fig. 4-6. However, the trends of creep rate for SAACW is similar to that for STD. NIFS-HEAT-2 in these two states both have a sharp change in stress exponent ("*n*" value). For example, under 240-280MPa at 700℃, STD has a change in "*n*" value from 5.6 to 55 and SAACW has the "*n*" value 3.9 to 11.5, respectively. When under about 180MPa at 750℃, the "*n*" value changes from 4.6 to 10.6 for STD and changes from 4.3 to 9.0 for SAACW, respectively. In contrast, SACWA keeps a consistent "*n*" value of 2.7 at 700℃ and 3.7 at 750℃, respectively, throughout the whole testing stress regions at each temperature.

Creep activation energy is an important parameter which determines creep mechanism of a material. It is well known that a creep deformation with the activation energy similar to the self-diffusion activation energy of the matrix is usually dominated by dislocation climbing. Above this energy level, some other mechanism such as dislocation glide starts to operate. Since the creep activation energy, Q_a as shown in Fig. 4-7 is consistent with the self-diffusion energy of vanadium (~270kJ/mol), the climbing-assisted creep mechanism is expected to operate in SACWA at all stress levels examined, as well as in STD under 100 MPa (243kJ/mol) and SAACW under 100-214 MPa (256kJ/mol in average). Above these stresses, Q_a is much higher than the self-diffusion energy of vanadium for both STD (390-400kJ/mol) and SAACW (434-461kJ/mol). In such case, dislocation glide is considered to start, and part of dislocation climbing continues. Thus the creep mechanism may change into dislocation glide together with climbing above 180 MPa for both STD and SAACW. This classification of stress regions, which divides stress level into "above 180MPa" and "below 180MPa", is consistent with the "*n*" values obtained. The "*n*" value ranging from 2.7 to 5.6 in climbing-assisted creep region changes into the range of 9.0 ~ 55 in dislocation glide creep region.

The reason why SAACW behaves like STD but not SACWA can be explained by the microstructures. In a TEM characterization of dislocation evolutions in SAACW before and after creep as characterized in Fig. 4-16, Professor Muroga [137] pointed out that after creep deformation, most dislocations in SAACW are of a/2 <1 1 1> type and, more specially, with Burgers vector b of $\pm a/2[1\ {-1}\ \pm 1]$. The analysis was based on the $g \cdot b = 0$ method, where *g* is the reciprocal vector that indicates the electron reflection condition, and *b* is Burgers vector.

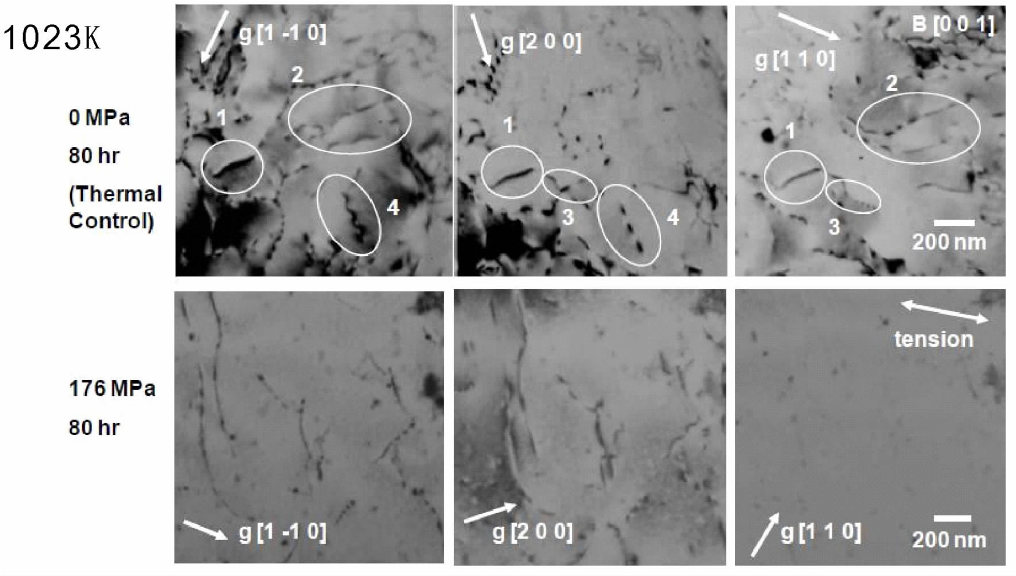

Fig. 4-16 Dislocation images of NIFS-HEAT-2 in SAACW state after creep deformation [137]

In SAACW before creep, which is designated as "Thermal Control", the sample went through annealing at 750℃ (1023K) for 80hrs. The dislocations in the thermal control specimen are the mixture of type a < 1 0 0 > (including type ± a[1 0 0] marked as "1" and type ± a[0 1 0] marked as "2") and type a/2 < 1 1 1 > (including type ± a/2[1 1 ±1] marked as "3" and type ± a/2[1 -1 ±1] marked as "4"). While, after creep, the dislocation density appears to be negligibly low under the condition of g[1 1 0]. This indicates that type ± a/2[1 -1 ±1] (belong to type a/2 < 1 1 1 >) dislocations are the predominantly remaining ones after creep, which are observed in g[1 -1 0] and g[2 0 0] conditions.

Similar situation was also found in STD crept at 750℃ under 176MPa for 60hrs and under 250MPa for 6hrs, as shown in Fig. 4-17. It is considered that the a/2 < 1 1 1 > type dislocations are also the mostly remaining ones for STD after creep. Type a < 100 > dislocations are not identified. According to Fig. 4-16 and Fig. 4-17, it is clear that the dislocation densities of SAACW and STD largely decrease soon after the creep starts, and only the dislocations of a/2 < 1 1 1 > type are dominant ones after creep deformation happened.

However, situation in SACWA is different from that in SAACW and STD. Fig. 4-18 shows the dislocation evolution in SACWA comparing with that in SAACW, under the same creep conditions and observation conditions. As discussed above, SAACW predominantly keeps low density of type a/2 < 1 1 1 > dislocations after creep. While, SACWA still keeps high density of dislocations after creep, even when type ± a/2[1 -1 ±1] dislocations are invisible under the condition of g[110].

Due to the high density of dislocations in SACWA, the characterization of dislocation Burgers vectors is not so sufficient. However, considering type a/2 < 1 1 1 > and type a < 1 0

0 > dislocations are popular dislocations in body central cube (BCC) crystals, it is regarded that the dislocations in SACWA before and after creep include both a/2 <1 1 1> and a <1 0 0> types.

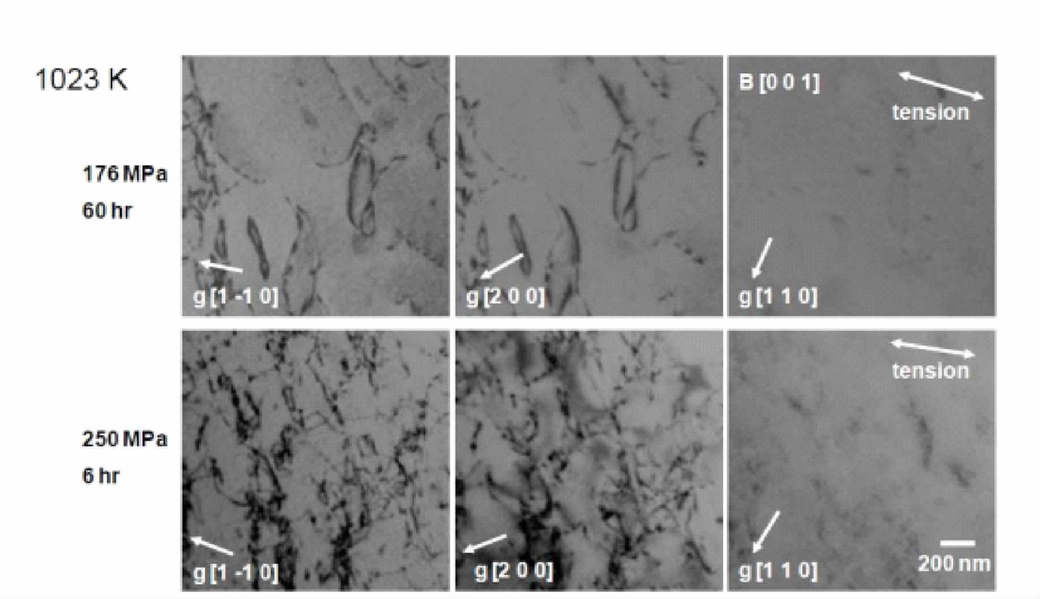

Fig. 4-17 Dislocation images in NIFS-HEAT-2 of STD state after creep deformation [137]

The reason of high density dislocations being kept after creep is considered to be that the fine precipitates formed along the dislocations could decorate the dislocations strongly, including those of sessile a <1 0 0> type produced by cold working. As a result, the strong decoration makes SACWA proceed with the climbing-assisted mechanism at stress regions of both over 180MPa and below 180MPa. That is why SACWA has lower creep rate than that of STD and SAACW proceeding with dislocation glide mechanism at stress over180MPa.

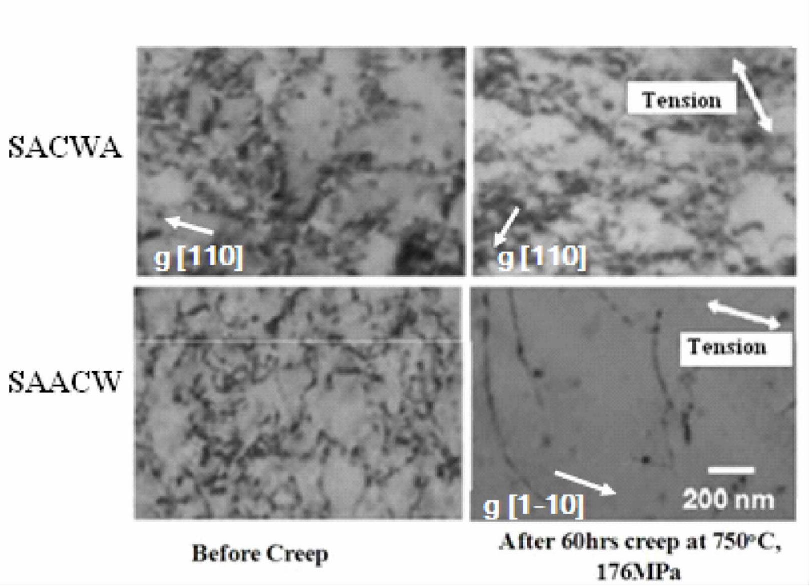

Fig. 4-18 Dislocation evolutions in SACWA compared with SAACW after creep [137]

4.5.3 Comparison of creep properties between NIFS-HEAT-2 and other vanadium alloys

For various V-4Cr-4Ti alloys, the most important difference is impurity concentration. Different impurity level not only affects the hardness and tensile strength of a material, but also affects its creep resistance. From Fig. 4-8 it can be seen that in STD state, NIFS-HEAT-2 has lower creep rate than SWIP-11; while in SACWA state, SWIP-11 has lower creep rate than NIFS-HEAT-2. The value of grain size for SWIP-11 is not available in this study, here just discuss about the effects of impurity levels on creep resistance. NIFS-HEAT-2 has lower total impurity level than SWIP-11. As discussed before, SWIP-11 has a lot of inclusions in the matrix, which results in many defects to be sinks for vacancy diffusion and enhances the dislocation motion in STD.

However, after SACWA treatment, SWIP-11 shows lower creep rate than NIFS-HEAT-2, although their hardness is nearly the same. The reason is considered to be that more impurities in SWIP-11 lead to more precipitates after aging, thus the resistance to dislocation motion is stronger.

4.5.4 Prediction of creep lift time for V-4Cr-4Ti alloys

In engineering application, the designed lifetime of V-4Cr-4Ti components is at least 10 year (or 100,000 hrs) for 700℃ operation at the minimum creep rate. Thus the maximum stress is an variable for different materials.

Fig. 4-19 shows the dependence of lifetime for 1% deformation at minimum creep rate on applied stresses for STD, SAACW and SACWA in the present study. In STD state, under the same stress, SWIP-11 has several times lower lifetime than NIFS-HEAT-2. However, in SACWA state, and under the same stress, SWIP-11 has a lifetime several times higher than that of NIFS-HEAT-2. This is certainly the result of different creep rates discussed above (in Part 4.5.3). From the data available people can see that, for NIFS-HEAT-2 alloy in STD state, the lifetime of 1% strain at the minimum creep rate is 2626 hrs under the condition of 700℃ and 100MPa. This lifetime is the highest, compared with that of SACWA and SAACW states under the same test conditions.

Since it is impractical to carry out long-time experiments for 100,000 hrs or more, and there are also possible risks to interrupt the experimental conditions during the experiment, relatively short-time experiments are preferred when some models are available for prediction. Larson-Miller parameter (LMP) is a widely used one for predicting the lifetime or maximum creep stress of a material. In this model, y axis is stress, and x axis is the Larson-Miller parameter. The Larson-Miller parameter can be described with equation (4-8) as below [138]:

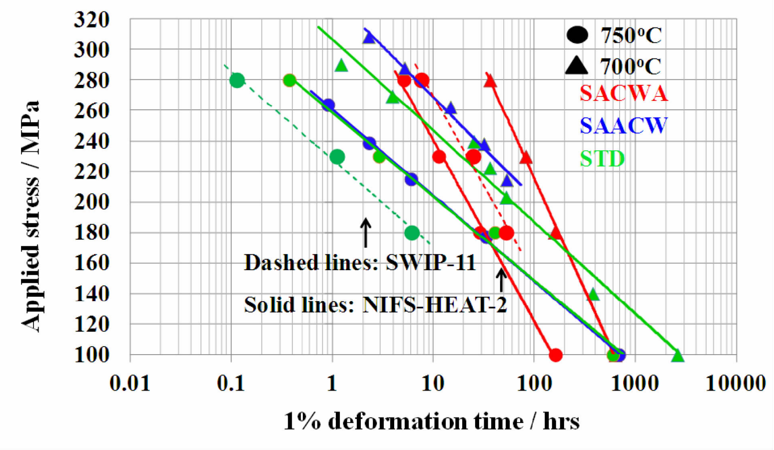

Fig. 4-19 Dependence of 1% strain lifetime for STD, SAACW and SACWA

$$P_{L-M} = T \cdot (C + \log t_{1\%})/1000 \tag{4-8}$$

Where, $t_{1\%}$ is the lifetime of 1% steady creep deformation, C is a material specific constant often approximated as 20 according to previous work [73].

However, the prediction using Larson-Miller parameter with $C = 20$ seems not efficient for NIFS-HEAT-2. Fig. 4-20 shows the prediction of maximum stress for NIFS-HEAT-2 under the condition of design criteria (working at 700℃ with 100MPa for 100,000hrs). Creep data of 700℃ and 750℃ tests in Fig. 4-6 are used for this prediction. According to this figure, STD and SAACW have almost the same maximum stress of 29.5MPa. This is much lower than the previously predicted value, 74MPa with $C = 20$, for similar V-4Cr-4Ti alloy in Ref. [73]. Moreover, according to the design criteria, NIFS-HEAT-2 in SACWA state does not have a positive value of maximum stress in the Larson-Miller prediction using $C = 20$ as shown in Fig. 4-20.

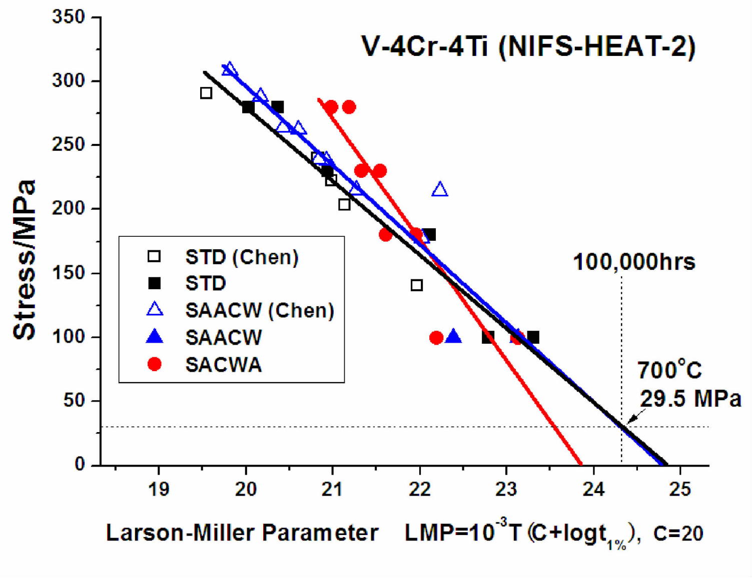

Fig. 4-20 Prediction of maximum stress for NIFS-HEAT-2 working at 700℃ for 100,000hrs.

The present study just uses simple extrapolation to roughly estimate the stress range of NIFS-HEAT-2 under the designed condition. Assuming the creep mechanism is not changing at low stress region including the extrapolated stress, a straight line in the plot is extended along the data trend with the smallest "*n*" value, as shown in Fig. 4-21. According to this extrapolation, the maximum stress is about 51MPa, 31MPa, and 16MPa for STD, SAACW and SACWA, respectively.

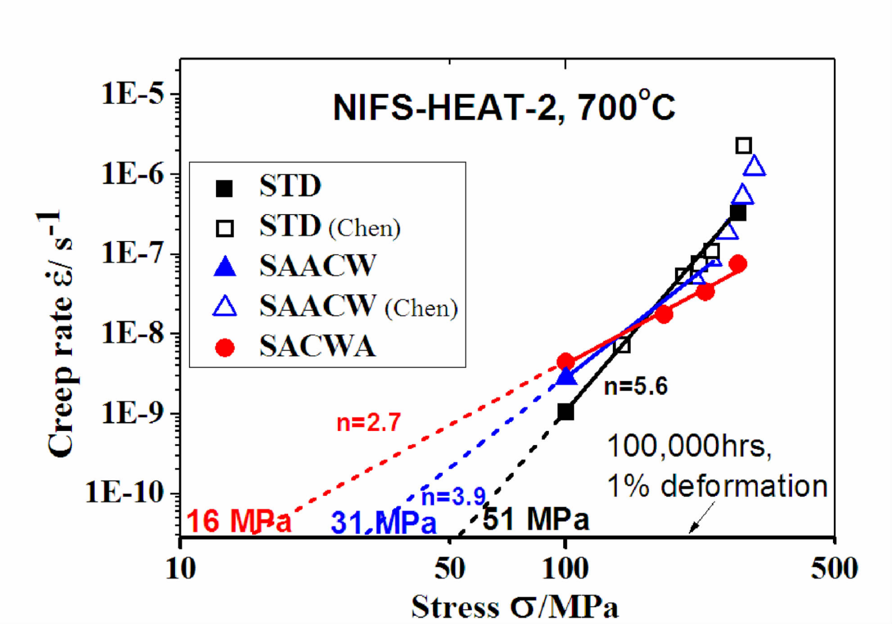

Fig. 4-21 Simple extrapolation for prediction of maximum stress for NIFS-HEAT-2 under designed condition.

Considering the dislocation climbing mechanism might change to be diffusion-creep-dominant instead of dislocation-creep-dominant at stresses as low as the above estimated value, the creep rate might be underestimated, and then the maximum stress might be overestimated. So, the real maximum stress is considered to be lower than 51MPa, 31MPa, and 16MPa for STD, SAACW and SACWA, respectively.

4.5.5 Further proposal for strengthening V-4Cr-4Ti alloys

Thermo-mechanical treatments can strengthen V-4Cr-4Ti alloys in hardness, tensile strength and creep resistance. In the present study, SAACW does not show remarkable advantages in creep resistance compared with STD, because the loss of dislocations during creep deformation enhanced creep deformation in SAACW. SACWA can benefit creep resistance at relatively high stress. However, it is also necessary to extend the usage of SACWA to obtain enhanced creep resistance at low stress levels. Dislocations in SACW can resist the growth of precipitates in SACWA, and the precipitates then resist the disappearance of these dislocations during creep. This mechanism would be common for various V-4Cr-4Ti alloys and even other alloys. In SACWA state in Fig. 4-9(b), SWIP-11 has higher creep resistance than NIFS-

HEAT-2, which indicates that high number density of precipitates could be one of the key factors that contributes to improved resistance of dislocation motion during creep. The interaction between dislocations and precipitates along them is a core factor that reduces creep rate at high stress region for SACWA. However in the future, it may be better to reduce the dislocation density, thus the interior vacancy diffusion and further dislocation climbing-dominated creep deformation can be inhibited. On the other hand, without pre-cold working, Ti-(CON) precipitates can coarsen with the increasing temperature and time. So, using dislocation to stabilize precipitation may not be an efficient way for improving creep resistance in all cases, inherently high thermal stability of precipitates are desirable.

According to the above consideration, high number density of thermally stable precipitates with low dislocation density should be the first priority in the research on strengthening V-4Cr-4Ti alloys for high temperature application.

4.6 Summary

The present study investigated the thermo-mechanical strengthening for V-4Cr-4Ti alloys at RT and high temperatures. The results show that the two different orders of work hardening and precipitation hardening can both strengthen V-4Cr-4Ti alloys. The order of work hardening and then precipitation hardening can remarkably enhance creep resistance of NIFS-HEAT-2 in relatively high stress region over 180MPa at both 700℃ and 750℃. The reason is considered to be interactions between dislocations and precipitates distributed along them. The comparison of NIFS-HEAT-2 with SWIP-11 shows higher impurity level may potentially lead to higher number density of precipitates and thus higher creep resistance. The summary of this study is as following:

(1) SAACW shares similar creep rate-stress dependence to that of STD. They both have the creep mechanism of dislocation glide with climbing at stresses over 180MPa. While, the creep of SAACW and STD is controlled by dislocation climbing-assisted mechanism at stresses below 180MPa approximately.

(2) The estimated upper stress for the same lifetime (100,000 hrs) of 1% deformation at 700℃ with minimum creep rate for STD and SAACW is at most 51MPa and 31MPa respectively, and for SACWA it is 16MPa.

(3) SACWA keeps dislocation climbing-assisted creep in wider stress range than that of SAACW and STD. This may be due to the reason that the dislocations are decorated by high number density of fine precipitates formed along them. Detailed classification is shown in Table 4-6.

Table 4-6 Classification of creep mechanisms for V-4Cr-4Ti with different thermo-mechanical treatments.

	< 180MPa	> 180MPa
STD	Dislocation climbing $n = 4.6 \sim 5.6$ $Q = 240$ kJ/mol	Dislocation glide & climbing $n = 10.6 \sim 55$ $Q = 390 \sim 400$ kJ/mol
SAACW	Dislocation climbing $n = 3.9 \sim 4.3$ $Q = 150$ kJ/mol	Dislocation glide & climbing $n = 9 \sim 11.5$ $Q = 360 \sim 460$ kJ/mol
SACWA	Dislocation climbing $n = 2.7 \sim 3.3$ $Q = 200 \sim 280$ kJ/mol	Dislocation climbing $n = 2.7 \sim 3.3$ $Q = 320 \sim 330$ kJ/mol

(4) SACWA can enhance creep resistance at high stress region. However in low-stress region, the creep resistance of SACWA is degraded by the enhanced vacancy diffusion due to high density of dislocations.

(5) The decoration of dislocations by precipitates in SACWA may also suppress the decrease of dislocation density during creep deformation.

(6) Due to interactions between dislocations and precipitates formed along them, SACWA may keep both type a < 100 > and type a/2 < 111 > dislocations. While, STD and SAACW may mainly have dislocations of a/2 < 111 > type. The evolution of microstructures of V-4Cr-4Ti alloy in STD, SAACW and SACWA states before and after creep is shown in Fig. 4-22.

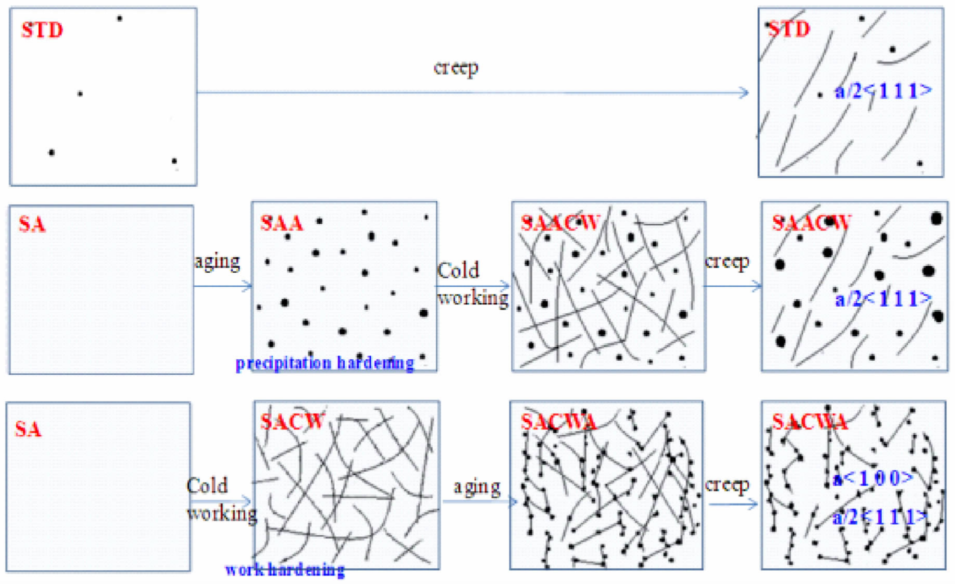

Fig. 4-22 Micro-structural evolution of V-4Cr-4Ti alloy in STD, SAACW and SACWA states

(7) Higher impurity level does not benefit the creep resistance of SWIP-11 alloy in STD state probably because of the many interfaces between matrix and inclusions. While in SACWA state, the more impurities lead to more precipitates, which then strengthen the alloy and increase its creep resistance.

(8) More precipitates can extend the usage of SACWA in resisting creep deformation toward to low stress regions.

(9) Further strengthening of V-4Cr-4Ti alloy for higher temperature application should avoid high dislocation density. A method which can introduce high number density of thermally stable precipitates without contribution from dislocations could be a leading method for strengthening V-4Cr-4Ti alloys at high temperatures.

CHAPTER 5

Mechanical properties of V – 4Cr – 4Ti alloy after static Li exposure

5.1 Chemistry for Molten Lithium and Vanadium Alloy System

Since lithium is so active that almost all insulating coatings cannot survive for long time in the blanket, efforts to consider new blanket concepts without much Li corrosion in coatings are becoming more and more important. Some researchers [139] have investigated the multilayer (or dual) coating approach for a more durable system. In this concept, the insulating coating is sandwiched between the main V structure and a thin (<100 μm) V layer which the flowing Lithium as shown in Fig. 5-1 [140]. Note the "vanadium" in the diagram should stand for V-4Cr-4Ti alloy in the present study.

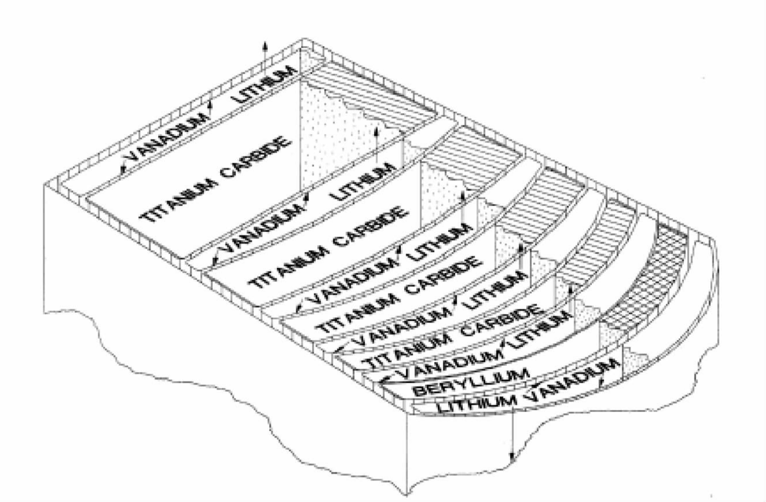

Fig. 5-1 Schematic of blanket sector cross-section [140]

According to the phase diagrams as shown in Fig. 5-2 [135], V, Cr, Ti and thus V-4Cr-4Ti alloy have good compatibility with liquid Li because they do not form obvious Li solutions. In this case, thin V-4Cr-4Ti wall has high electrical resistivity which can reduce electrical current and thus reduces the MHD pressure drop. Therefore, the most concern of multilayered (or dual coated) V-4Cr-4Ti alloy could be the impurity-assisted corrosion [141] of grain boundaries and change of mechanical properties caused by mass transfer. This study will just talk about the effects of mass transfer.

The mass transfer across liquid Li and V-4Cr-4Ti alloy is based on the thermodynamic equilibrium of chemical potential among the Gas-Liquid-Solid system. Fig. 5-3 shows the Gibbs free energy of formation for selected carbide, oxide and nitrides with Lithium-Nitrogen solutions. According to the thermodynamic calculation, TiC, CrC are more stable than LiC; Li_2O is more stable than all other oxides; VN and especially TiN are more stable than Li_3N in the temperature range from 50℃ to 1050℃. This indicates the C and especially N can be trapped by Ti in the alloy matrix, while O can be trapped from V matrix to Li at the operation temperature of blanket. Only Fig. 5-3 (c) has marks of equilibrium scale for impurity concentration because only N level is available in the as-received Li. The value of 0.0048 is an estimated N concentration at which V has equilibrium chemical potential compared with Li at 650℃.

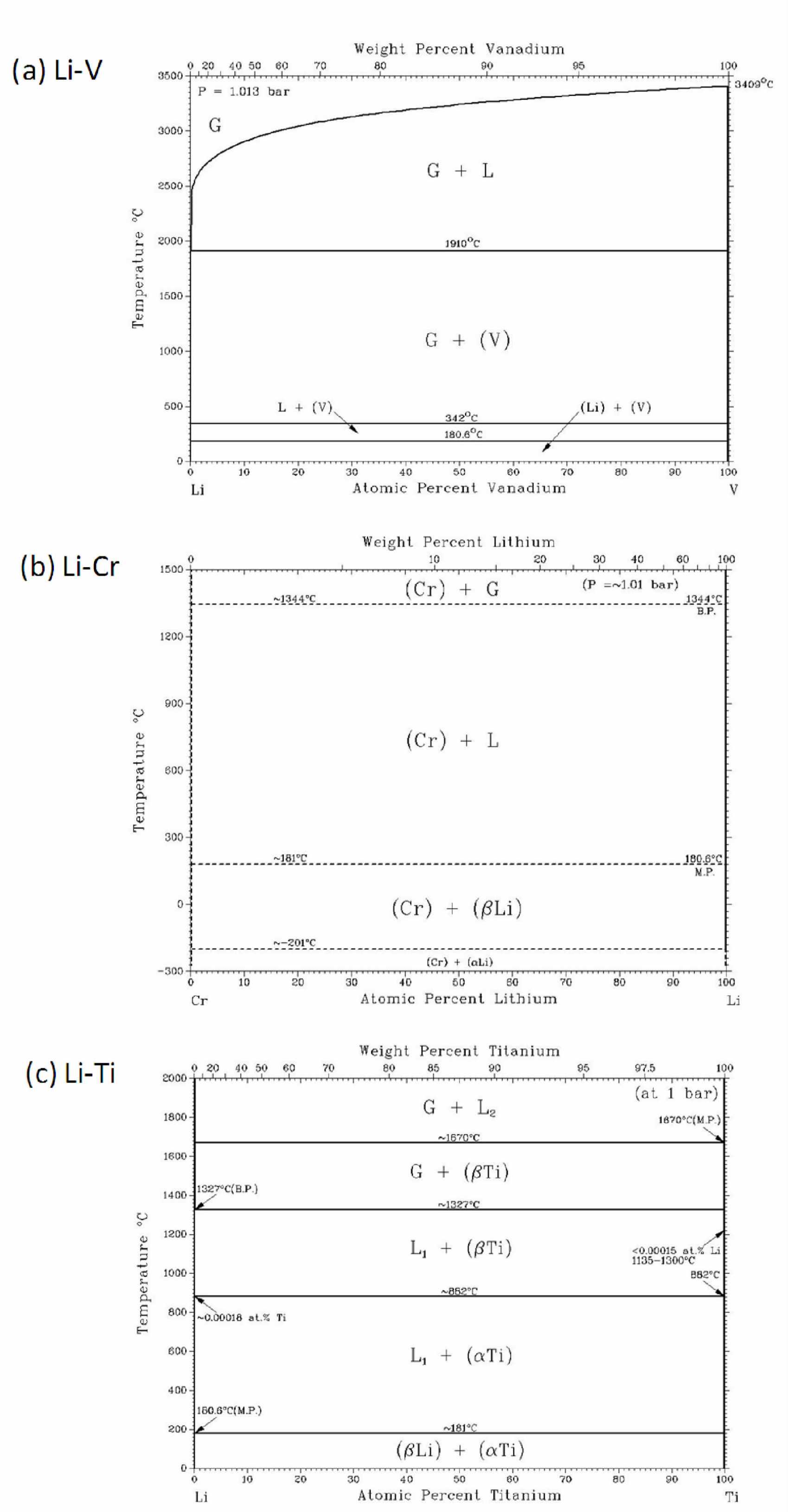

Fig. 5-2 Phase diagrams of Li-V (a), Li-Cr (b) and Li-Ti (c) [135]

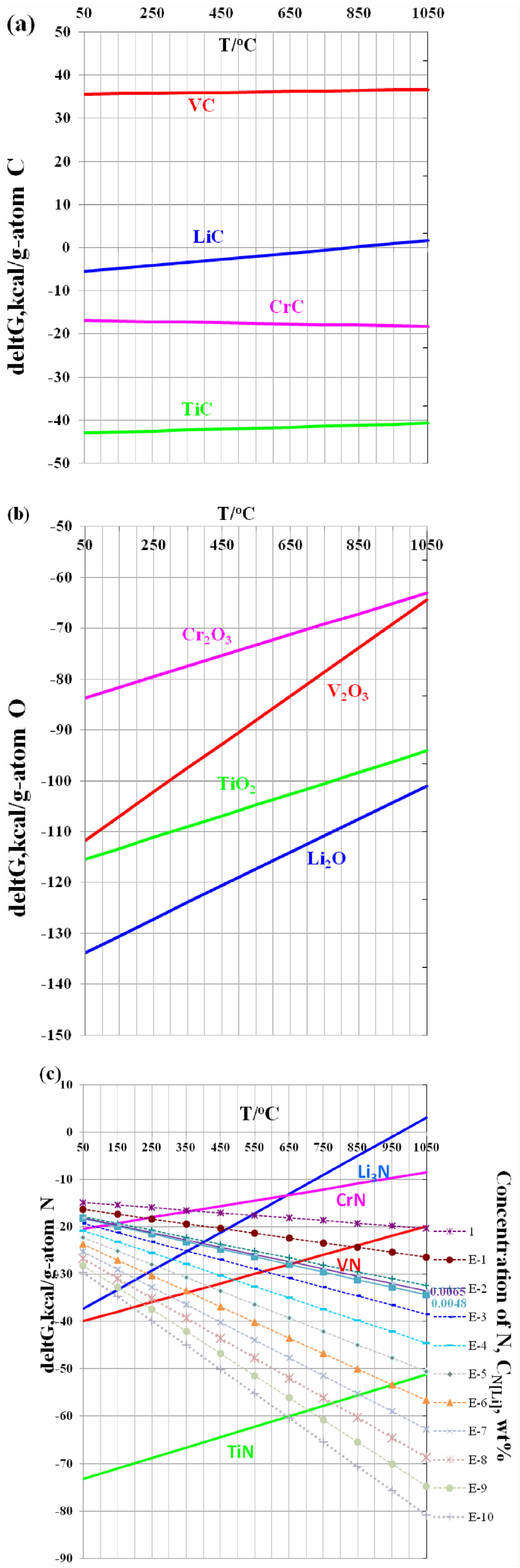

Fig. 5-3 Gibbs free energy of selected nitrides formation and lithium carbide (a), lithium oxide (b) and lithium nitrogen (c)

5.2 Experimental

5.2.1 Sample Preparation

The samples used in this study are chosen from the thermo-mechanically treated ones. The NIFS-HEAT-2 (V-4Cr-4Ti alloy) in STD and SACWA states exhibited relatively high creep resistance at low and high stress regions, respectively. The effects of mass transfer and thermal aging on mechanical properties of the V-4Cr-4Ti alloy with these two treatments are of concern. So they are introduced in liquid lithium exposure test. Moreover, in order to identify the effects of mass transfer related to alloying element such as Ti, pure vanadium is used for comparison. The comparison of chemical compositions between pure vanadium and the V-4Cr-4Ti alloy, NIFS-HEAT-2, are listed in Table 5-1. In order to identify the effects of dislocations on mechanical properties of the alloy, a V-4Cr-4Ti alloy in SAA state is used to compare with the alloy in SACWA state. Where, SAA has high number density of precipitates but only a few dislocations while SACWA has both high number density of precipitates and high density of dislocations.

Table 5-1 Chemical composition of pure vanadium and V-4Cr-4Ti alloy used (NIFS-HEAT-2)

	Alloying elements (wt%)			**Impurities (wppm)**		
	V	Cr	Ti	C	O	N
NIFS-HEAT-2	Bal.	4.02	3.98	67	148	122
Pure V	Bal.	—	—	90	60	120

Thus, there are a total of four groups of samples and treatments as shown in following description and Table 5-2:

(1) Pure V, is pure vanadium after recrystalization from hot and cold working.

(2) STD is the standard heat treatment for V-4Cr-4Ti alloy (NIFS-HEAT-2).

(3) SACWA is the treatment of work hardening and then precipitation hardening for V-4Cr-4Ti alloy (NIFS-HEAT-2). This treatment can introduce high density of dislocations and fine precipitates along these dislocations.

(4) SAA is only precipitation hardening for V-4Cr-4Ti alloy (NIFS-HEAT-2).

Table 5-2 Samples for this study and the relevant treatments

Sample	Annealing	Cold working	Aging
Pure V	900℃ ×1hr	—	—
STD	1000℃ ×2hrs	—	—
SACWA	1100℃ ×1hr	20% rolling	600℃ ×20hrs
SAA	1100℃ ×1hr	—	600℃ ×20hrs

Note SAACW is not used, because SAACW with a further aging can be regarded as a work hardening followed by precipitation hardening again, and cannot be clearly distinguished from SACWA. These materials are prepared to be tensile samples, coupon samples, and chemical analysis samples. The specifications and purpose for them are listed in Table 5-3.

Table 5-3 Specifications and purpose for samples of each material

ID	Specification	Purpose
Tensile sample	4mm × 16mm × 0.25mm (SSJ)	Weight change, tensile tests and creep tests.
Coupon sample	5 ~ 10mm × 11mm × 0.25mm	Hardness, cross-section analysis, TEM observation
Chemical analysis sample	10mm × 50mm × 0.25mm × 2 (0.7 g × 2 for each material)	Chemical analysis

5.2.2 Lithium Exposure

Since V-4Cr-4Ti alloy is designed to work in liquid lithium at 700℃ and a potential temperature of 750℃, lithium exposure at a temperature within this range is highly favored. Up to now, lithium exposure tests have been carried out at 700℃ and 800℃ [125-127], the present study focuses on lithium exposure test at 650℃.

The tensile samples and coupon sample were assembled with gaps as shown in Fig. 5-4 (a) below to avoid surface adherence, and then together with another assemblage of chemical analysis samples, were put into a crucible made of molybdenum (See Fig. 5-4 (b)). 37g liquid lithium with 65 wppm N was filled into the crucible in a glove box, and the glove box is filled with 99.9999% Ar atmosphere (See Fig. 5-4 (c)). The top of the crucible was covered with Zr foil, and then inserted into a steel container with Cu gasket. The heating was carried out in air by putting the sealed container in an induction heater.

After heating at 650℃ for about 250 hrs, the steel container was again moved into the glove box, and the Mo crucible was taken out and reheated to melt the solidified lithium for picking up the exposed samples inside.

A cleaning of Li exposed samples was carried out by putting the samples in pure ethanol (maybe methanol by mistake). The pure ethanol is kept in air.

Fig. 5-5 shows a coupon sample before and after Li exposure. Note no more other special post treatment was performed on the as-cleaned samples.

5.2.3 Thermal Aging

Since high-temperature Li exposure includes co-effects of mass transfer and thermal aging, a control aging for the second group of samples was also carried out at 650℃ for the same duration in vacuum. Moreover, a third group of samples in initial state are introduced to indentify the effects of vacuum aging on the change of mechanical properties.

The arrangements of experiments and samples is as shown in following Table 5-4:

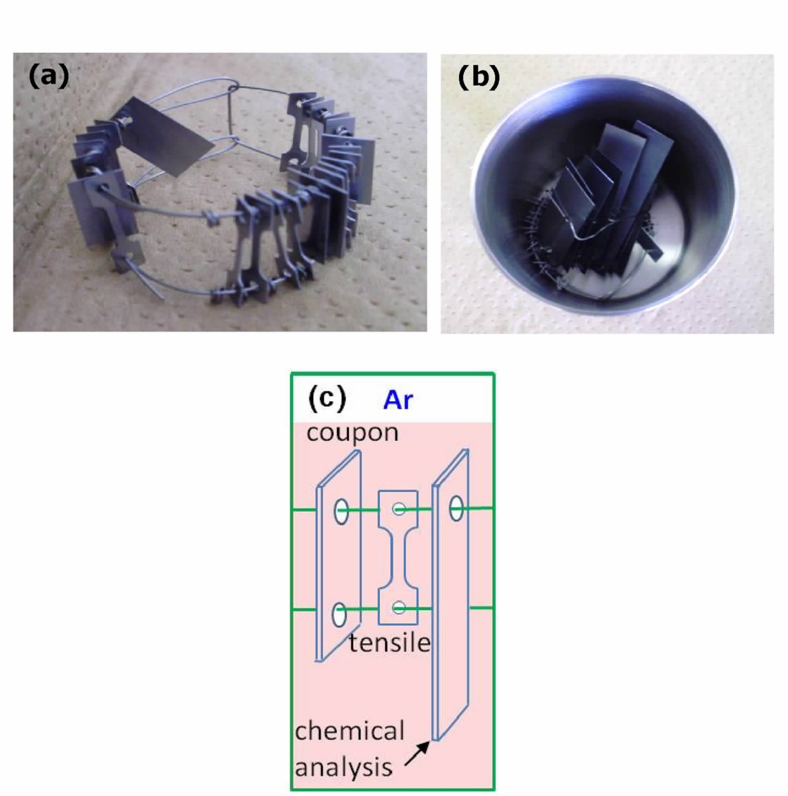

Fig. 5-4 Assemblage of samples for Li exposure

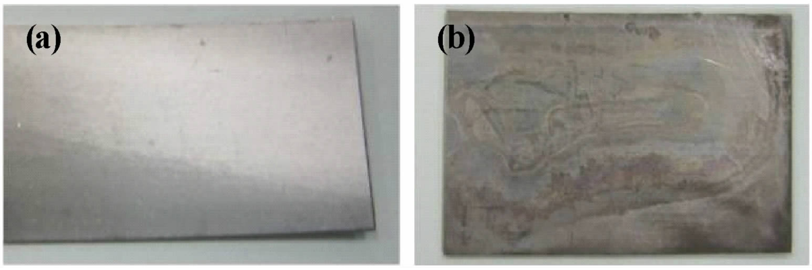

Fig. 5-5 Typical surface morphologies of the samples (a) before Li exposure and (b) after Li exposure

Table 5-4 Arrangements of samples and experiments in present study

	Group 1 Li exposure at 650℃ for 250hrs	**Group 2** Vacuum aging at 650℃ for 250hrs	**Group 3** Initial state
Pure V	In crucible	In furnace	In air
STD	In crucible	In furnace	In air
SAA	In crucible	In furnace	In air
SACWA	In crucible	In furnace	In air

With the above arrangements, the effects of aging and mass transfer on the mechanical properties of V-4Cr-4Ti alloy are clarified.

5.2.4 Evaluation of Lithium Exposure Effects

Mechanical property tests such as hardness (including cross-section hardness) test have been carried out on all coupon samples at RT. Tensile tests were carried out at RT and 700℃ for each material. Creep properties were characterized at 700℃ for STD, SAA and SACWA. Since the typical design criterion of stress for V-4Cr-4Ti alloy is 100MPa, this study takes100MPa and 180MPa as the experimental stresses. All tests at 700℃ were performed in vacuum with Zr getter. Chemical analysis and TEM observations have been carried out for all the 4 groups of samples. Note the samples after cleaning with ethanol had no other specific post-treatment, and some cleaning products are still adhering on the sample surface.

5.3 Mechanical Properties

5.3.1 Surface Hardness Evolution for Different Treatments

Fig. 5-6 shows hardness of Pure V in initial state, vacuum-aged state and Li-exposed state along with V-4Cr-4Ti alloy in STD, SAA and SACWA states. For Pure V, there is no obvious change in hardness after any treatment. While for V-4Cr-4Ti alloy, there are various changes. In detail, STD, SAA and SACWA are hardened remarkably after Li exposure. While, vacuum aging softens SACWA very much, softens SAA a little bit, and seems to bring some unnoticeable hardening to STD.

5.3.2 Evolution of Tensile Properties for Different Treatments

Fig. 5-7 shows RT tensile curves for Pure V, STD, SAA and SACWA in initial (a), vacuum-aged (b) and Li-exposed (c) states. Fig. 5-8 show 700℃ tensile curves for Pure V, STD, SAA and SACWA in initial (a), vacuum-aged (b) and Li-exposed (c) states. The yield stresses and uniform elongations at RT and 700℃ for all samples are plotted in Fig. 5-9.

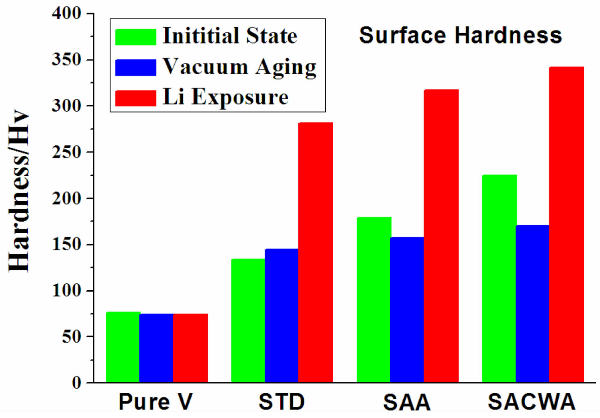

Fig. 5-6 Hardness of initial, vacuum-aged and Li-exposed Pure V along with V-4Cr-4Ti alloy in STD, SAA and SACWA states

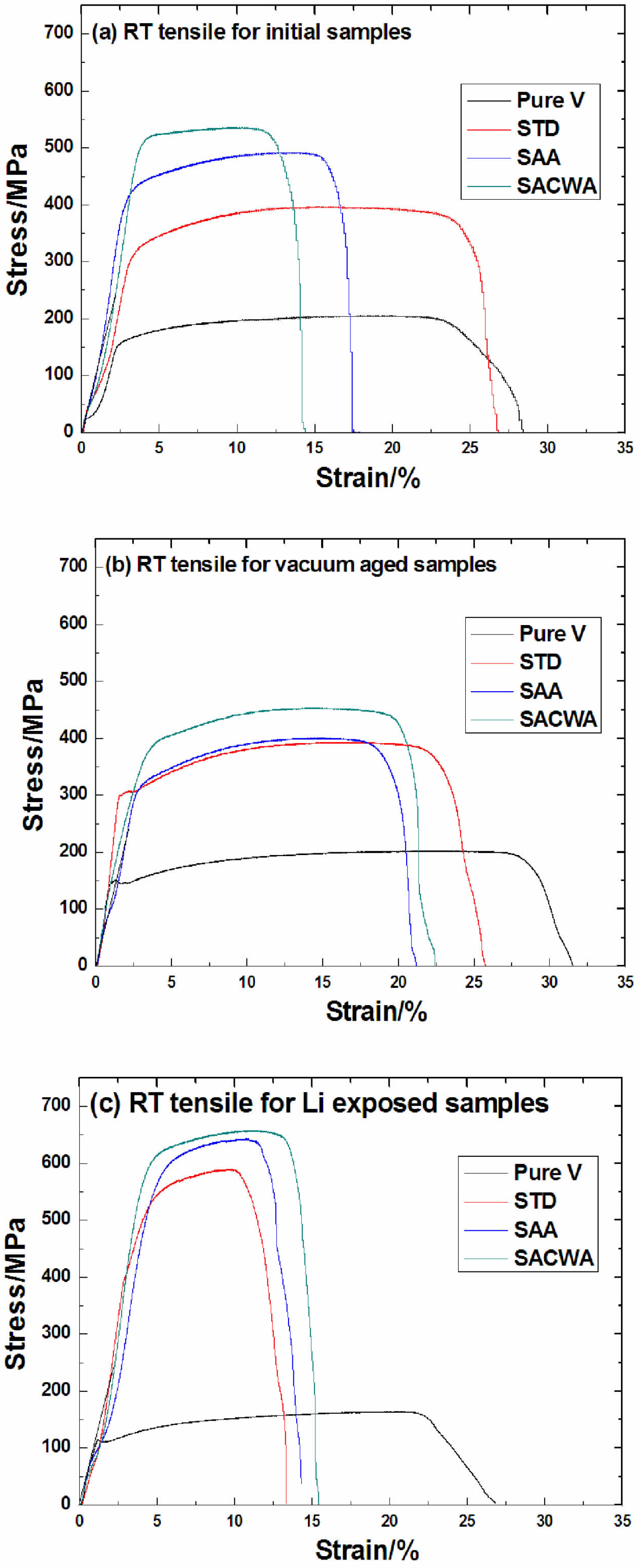

Fig. 5-7 RT tensile curves of Pure V along with V-4Cr-4Ti alloy in STD, SAA and SACWA states in (a) initial, (b) vacuum-aged and (c) Li-exposed states

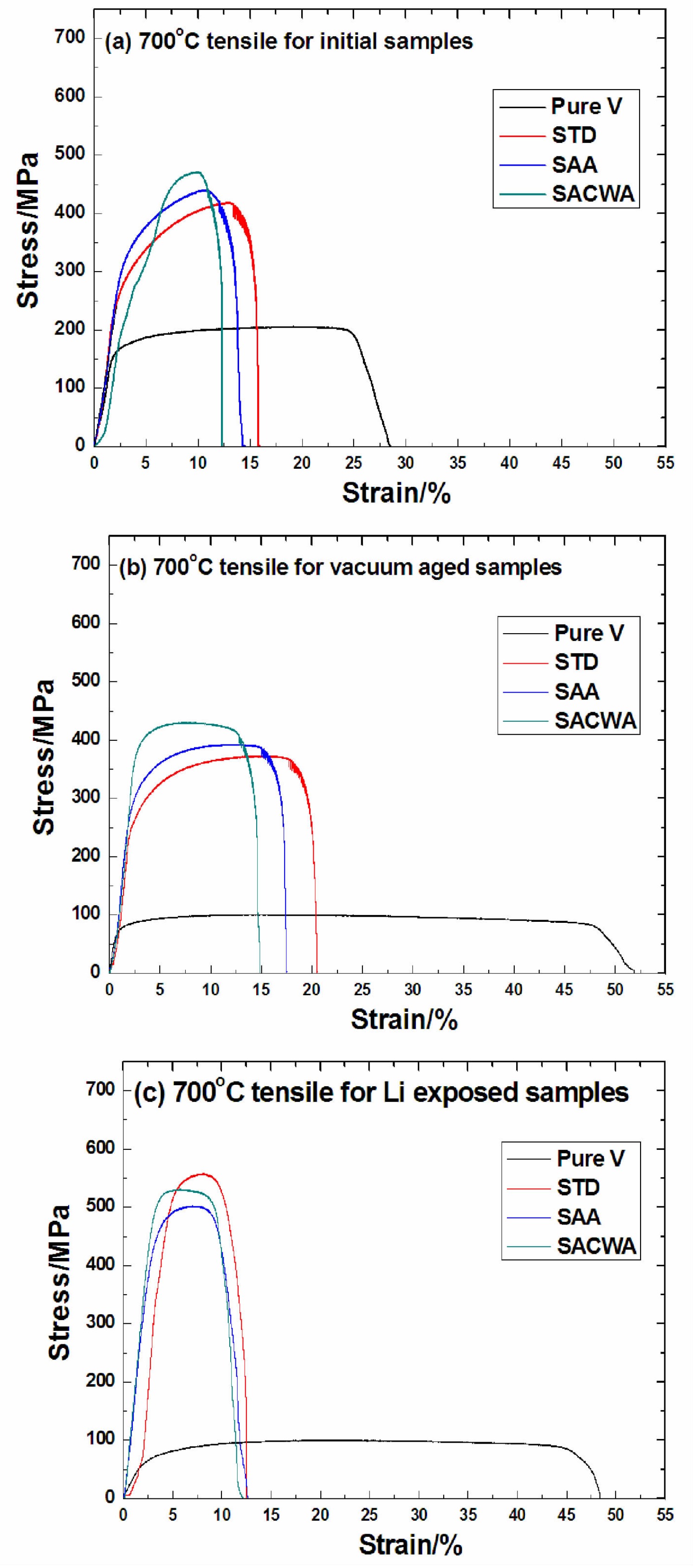

Fig. 5-8 700℃ tensile curves of Pure V along with V-4Cr-4Ti alloy in STD, SAA and SACWA states in (a) initial, (b) vacuum-aged and (c) Li-exposed states

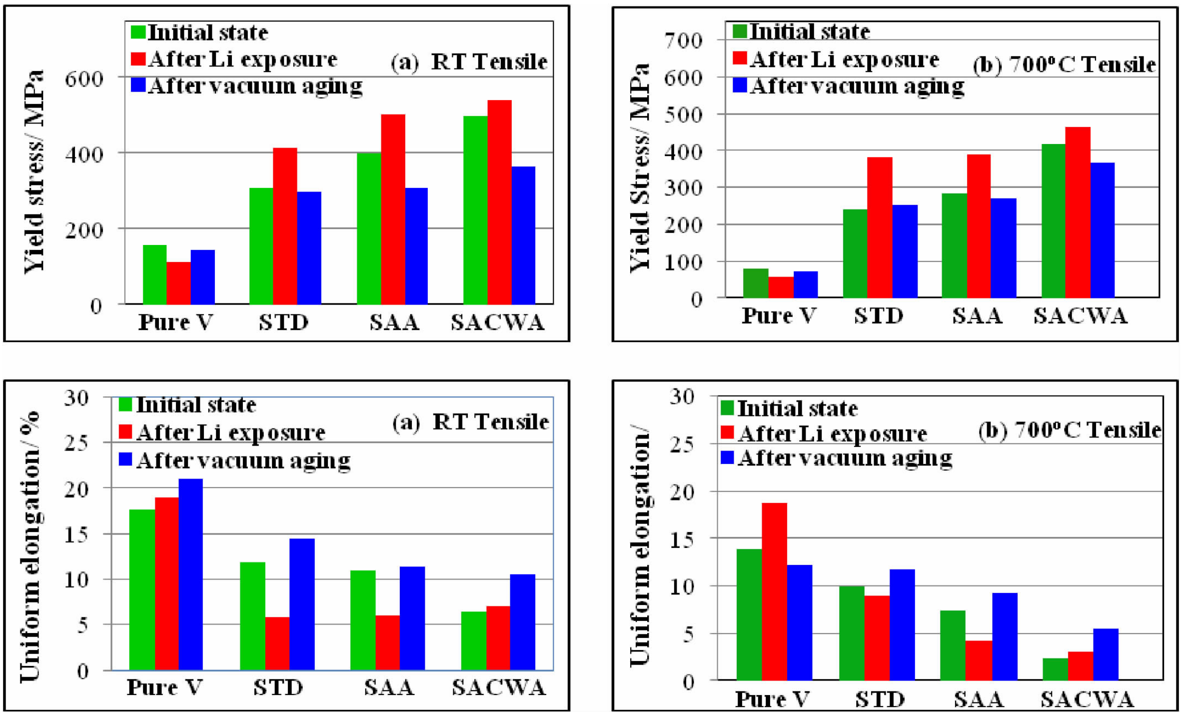

Fig. 5-9 Tensile properties of initial, vacuum-aged and Li-exposed Pure V along with V-4Cr-4Ti alloy in STD, SAA and SACWA states at (a) RT and (b) 700℃

According to the RT tensile results, Pure V is softened after Li exposure, while the V-4Cr-4Ti alloys are strengthened. The strengthening of STD and SAA, on the other hand, causes a decrease in uniform elongation. However, after Li exposure, the uniform elongation of SACWA seems not to decrease, which is considered to be due to the decrease in dislocation density. The strengthening for SACWA is smaller than that for STD and SAA, which is considered to be due to the resistance of precipitate coarsening by dislocations. Vacuum aging softens SAA and SACWA, and increases their uniform elongations. The trends of tensile properties of V-4Cr-4Ti alloy at 700℃ are similar to those at room temperature. Generally speaking, higher yield stress accompanies lower uniform elongation.

5.3.3 Creep Properties

Creep tests are only performed on Li-exposed STD, SAA and SACWA. Fig. 5-10 shows 700℃ creep curves for V-4Cr-4Ti alloy in 3 different states after Li exposure. The tests were carried out under 100MPa and 180MPa, and were all stopped before fracture when the secondary creep stage has been reached for several hrs, depending on different test durations. Results show that STD has the lowest creep rate and SACWA has the highest creep rate. Most interests are focused on the alloy with these two treatments.

Fig. 5-11 shows typical comparison of creep curves for V-4Cr-4Ti alloy with and without Li exposure. The material used in this example is SACWA. It is clear that the Li exposure has strengthened SACWA a lot since the strain in the same creep time was largely decreased under the same stress. The Li-exposed SACWA under 180MPa even has a lower creep rate than the initial SACWA under 100MPa. Converting the creep curves into the dependence of creep rate on applied stress, the comparisons of change in creep rates for STD and SACWA with and without Li exposure are shown in Fig. 5-12. The results clearly show that STD was also strengthened by the Li exposure. However, the Li exposure still did not change the fact that STD is more effective to get lower creep rate than SACWA in low stress region (below 180MPa).

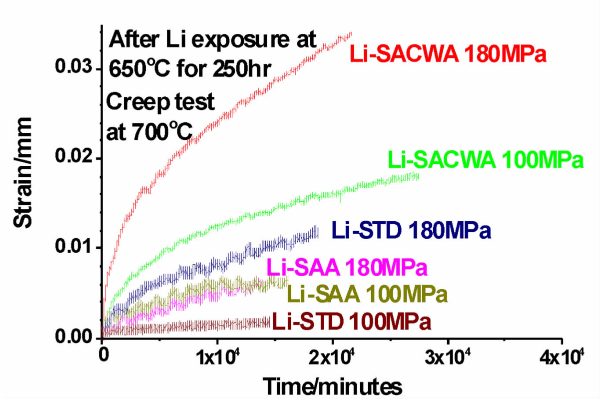

Fig. 5-10 700℃ creep curves for STD, SAA and SACWA after Li exposure at 650℃ for 250hrs

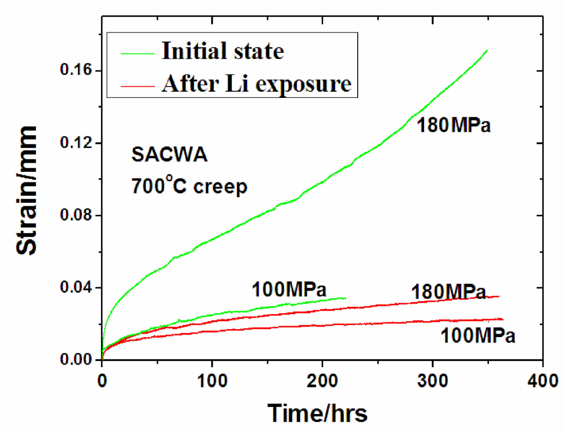

Fig. 5-11 Comparison of creep curves for SACWA with and without Li exposure

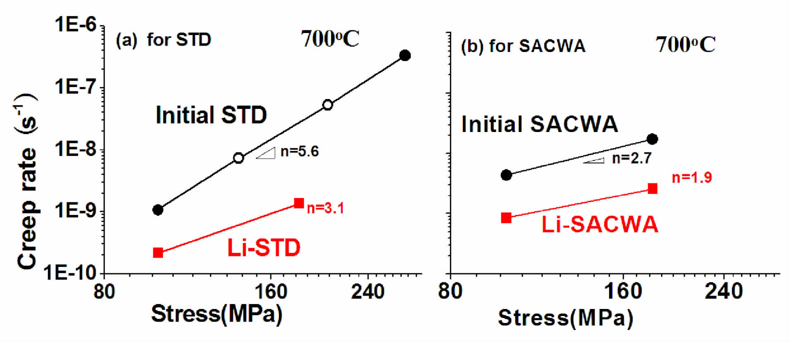

Fig. 5-12 Comparison of creep rate changes for (a) STD and (b) SACWA with and without lithium exposure. Data with open symbols are from [131].

All creep data in Fig. 5-12 above are fitting to the following equation:

$$\dot{\varepsilon} = A \cdot \sigma^{n} \cdot exp(-Q_{\alpha}/RT) \tag{4.5}$$

According to this fitting, the stress exponent "n" for STD at 700℃ is 5.6 in the initial state and 3.1 after Li exposure; the stress exponent "n" for SACWA at 700℃ is 2.7 in initial state and 1.9 after Li exposure.

5.3.4 Cross-Section Hardness

Since mass transfer happened during Li exposure, it can cause change in hardness on cross section of the exposed samples. Fig. 5-13 shows the cross-section hardness of Pure V, STD, SAA and SACWA. All of these samples are sorted in initial state, after vacuum aging and after Li exposure. For Pure V, the hardness has no remarkable change after each post-treatment. While for V-4Cr-4Ti alloy, the situation varies very much. In detail, STD has no remarkable change in hardness after vacuum aging, but it was hardened after Li exposure, especially in an area of 75μm near each surface; SACWA was softened by vacuum aging uniformly, and was also softened by Li exposure limited in center part, but it was hardened by the Li exposure in an area of 75μm near each surface. The situation for SAA is similar to that of SACWA.

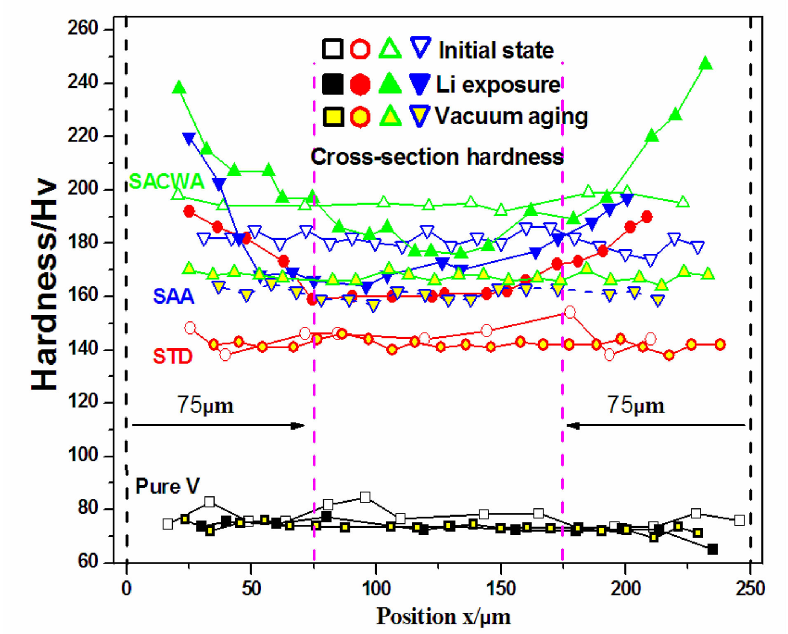

Fig. 5-13 Cross-section hardness of Pure V, STD, SAA, and SACWA in initial state, with vacuum aging and after Li exposure

5.4 Microstructure

Figure 5-14 shows the microstrucures of Pure V, STD, SAA and SACWA in initial state, after Li exposure and after vacuum aging. It must be noted that the microstructural observation was conducted on the central part of the specimens, around the position of 125 μm in Fig. 5-

13. For pure V, although Fig. 5-3 (c) indicates that vanadium nitride can form rather than lithium nitride, there seems neither change in microstructure of the material after Li exposure, and nor change after vacuum aging. High density of precipitates are formed in STD after Li exposure, but no remarkable presence of precipitates are observed after the vacuum aging. There are new pecipitates formed in the initial state SAA after Li exposure, though they are too small to be observed in the present study. It is noticed that the existing precipitates in SAA have coarsened after either Li exposure or vacuum aging. In SACWA, precipitates are not observed under the present conditions, but they are expected to form along the dislocations during the Li exposure and further vacuum aging, according to the previous study [130] and the discussion in Chapter 4 of this thesis. The dislocation density of SACWA decreases during both the Li exposure and the vacuum aging. Li exposure, however, seems to keep more dislocations ($1.0 \times 10^{14}/m^2$) than the vacuum aging keeps ($5.5 \times 10^{13}/m^2$).

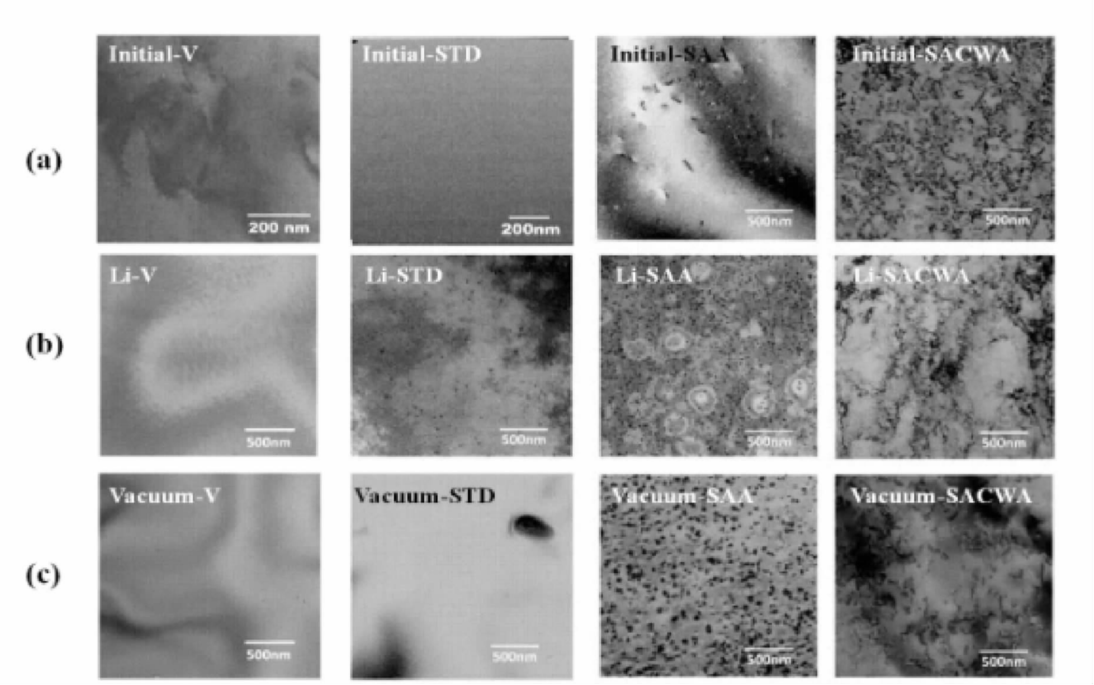

Fig. 5-14 TEM images for pure V and V-4Cr-4Ti (a) in initial state, (b) after Li exposure, (c) after aging in vacuum. Note: TEM images for pure V and STD in initial state are from the previous studies

5.5 Evaluation of Cleaning Method Basing on Chemical Analysis

Fig. 5-15 shows the results of chemical analysis for Pure V, STD, SAA and SACWA in their initial state, with vacuum aging and after Li exposure. It is considered that no obvious change of impurity levels has occurred during the vacuum aging. A thin layer which can be wiped away easily was formed on sample surfaces after cleaning (See Fig. 5-16). It is considered the most possible reason for the remarkable increase in all impurity levels of the Li-exposed samples.

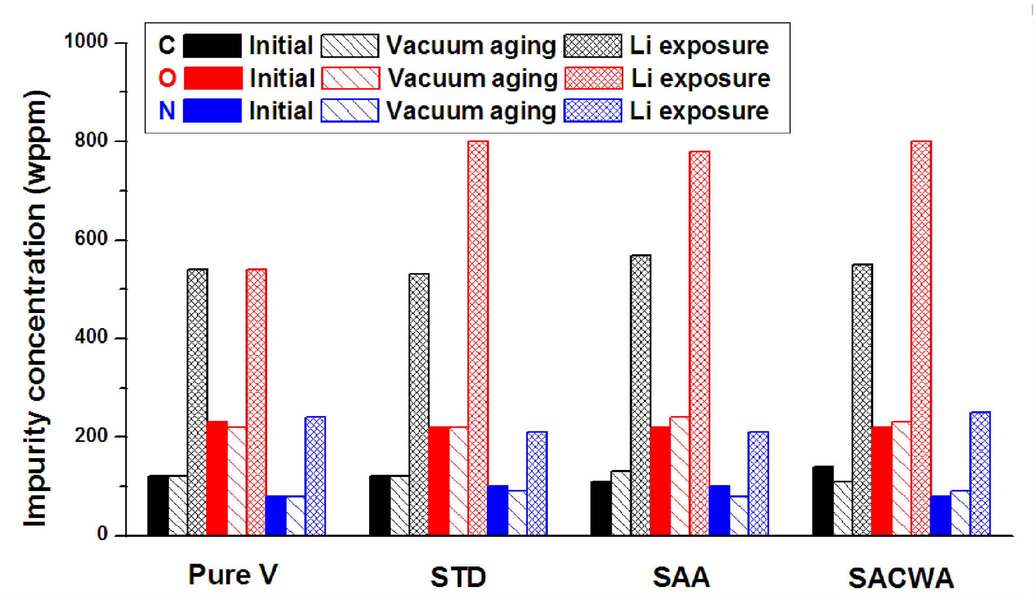

Fig. 5-15 C, O and N concentrations of the samples in initial, vacuum aging and Li-exposure states

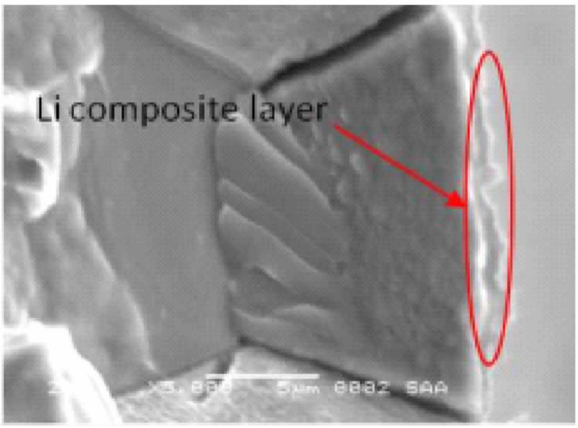

Fig. 5-16 Layer formed on sample surface after cleaning the Li with alcohol

After Li exposure, all C, O and N concentrations have excessive increase. See Table 5-5 for the increase in C, O and N concentrations. The rough ratio of mass increase for C to O is 2∶1 for Pure V, and 1∶1 for the V-4Cr-4Ti alloy. During the cleaning procedure, the reaction between Li and ethanol (may be methanol by mistake) causes Li composite and the Li composite can deposit on the sample surface. Detailed reaction formula is as follows:

$$2Li\ (s)\ +\ 2CH_3CH_2\text{-}OH\ (l)\ =\ 2\ CH_3CH_2\text{-}OLi(s)\ +\ H_2(g)$$

In the above formula, the mass ratio of C to O is 2∶1, which agrees with the rough estimation for Pure V. Considering the cleaning is carried out in the air, O_2 and N_2 can react with Li further and form Li composites which will then deposit on the sample surface. However, the reaction between Li with O_2 and N_2 in the air can be avoided, thus the formation of lithium alcoholate is the major reason that interferes with the chemical analysis results for impurity change in Li-exposed V and V-4Cr-4Ti alloy.

Table 5-5 Change in impurity concentrations for Li-exposed samples after cleaning in ethanol

Material		**C**	**O**	**N**
	Weight increase (wppm)	420	310	160
	Mass increase (ppm)	1785	988	588
Pure V	Rough C:O ratio		2:1	
	Weight increase (wppm)	410	580	110
	Mass increase (ppm)	1743	1849	401
STD	Rough C:O ratio		1:1	
	Weight increase (wppm)	460	560	110
	Mass increase (ppm)	1955	1785	401
SAA	Rough C:O ratio		1:1	
	Weight increase (wppm)	410	580	170
	Mass increase (ppm)	1743	1849	620
SACWA	Rough C:O ratio		1:1	

5.6 Discussion

5.6.1 Diffusion of C, O and N

Mass transfer during Li exposure is one of the main factors that contribute to the change of mechanical properties for V-4Cr-4Ti alloy. The concentration of impurities in starting Li and material is also important. Among the impurities, N is the only one with clear concentration level (65wppm) in the present study. According to Fig. 5-3 (c), equilibrium concentration of N at 650℃ for VN formation is 48 wppm in Li, which is lower than the N concentration in the as-received Li, indicating VN can form easier than Li_3N. In consequence, N is expected to transfer mostly into V alloy matrix. However, Ti has even stronger affinity with N than V does. It is considered that Ti in V-4Cr-4Ti traps much N, and the N concentration in Li decreases largely, then formation of VN in pure V is reduced largely. Likewise, according to Fig. 5-3 (a) and Fig. 5-3 (b), C is expected to be trapped by Ti in V matrix. While O transfers from V matrix to liquid Li, though C and O concentrations in starting Li are unknown.

From the TEM images people can see that the strengthening of STD after Li exposure should be due to the formation of precipitates. Some previous studies also showed that the N and C in Li solution can be trapped by Ti in the alloy matrix, hardening the alloy; while O diffuses from the alloy matrix into the molten Li, softening the alloy [125-127]. The loss of O is considered to be the reason why precipitates in Li-exposed SAA are smaller in size than those in vacuum-aged SAA. Again note the TEM observation is performed on the central part of the cross section.

According to Ref. [142], the diffusion coefficients of O and C in V matrix at 650℃ are 2.46×10^{-13} m^2/s and 2.29×10^{-13} m^2/s, respectively. Based on equation (5-1) as shown below.

$$d \approx \sqrt{D \times t} \tag{5-1}$$

Where, d is diffusion range;

D is diffusion coefficient;

t is diffusion time in seconds.

And, D can be determined with equation (5-2)

$$D = D_0 e^{(-Q/RT)} \tag{5-2}$$

Where, D_0 is frequency factor;

Q is diffusion activation energy;

T is absolute temperature; and,

R is gas constant.

The calculated diffuion ranges are 475μm for O and 452μm for C, respectively, which penetrate the whole cross section of the specimens. While in the same condition, the diffusion coefficient of N in V is 6.67×10^{-15} m^2/s, giving a diffusion range of 78μm. This diffusion range is much smaller than those of O and C, and is not very different from the hardening range of V-4Cr-4Ti alloys (75μm) as shown in Fig. 5-13. Consequently, N diffusion contributes more to surface hardening than C and O diffusion does.

In this case, the additional precipitates in the alloy observed with TEM are considered to be C-rich Ti(C, O, N) particles. The reason is that TEM observations in this study are performed on the center of the specimens, which is beyond the diffusion range of N in the present Li exposure, and O is gone into Li. These C-rich Ti(C, O, N) precipitates contribute to the hardening at all positions in STD. While, N mainly contributes to the hardening within the diffusion range, which is about 75 μm from the surfaces. In the hardened area of V-4Cr-4Ti alloys, there is more hardening caused by C and N than the softening caused by the decrease in O concentration.

The Li-exposed SAA and SACWA only gain hardening within 75 μm from the surfaces. For SACWA, the dislocations can supply nucleation sites for the precipitates and supress the coarsening of precipitates [130], enhancing the hardening. Then the stronger interaction between dislocations with precipitates increases the yield stress in SACWA, which in turn reduces the creep rates as shown in Fig. 5-12. However, SAA and SACWA are softened in the center part after Li exposure. The softening of SAA is considered to be caused by the decrease in number density of the precipitates due to their growth. This might be more effective than the hardening caused by additionally formed C-rich Ti(C, O, N) precipitates. The softening of

SAWCA in its center part is probably caused by the decrease in dislocation density in the V-4Cr-4Ti alloy.

For pure V, there seems no change in the microstructures after Li exposure. However, since O has diffused from V matrix to liquid Li, the V matrix was softened according to the tensile test results shown in Fig. 5-9.

In the future estimation, the time and temperature dependence for impurity transfer can be converted from equation (5-1) and (5-2) into equation (5-3):

$$\begin{aligned} d &\approx \sqrt{D_0 \times \exp\left(-\frac{Q}{RT}\right) \times t} \\ &= \sqrt{D_0} \times (\exp(-Q/2R))^{\frac{1}{T}} \times t^{\frac{1}{2}} \\ &= A_0 \times B_0^{\frac{1}{2}} \times t^{\frac{1}{2}} \end{aligned}$$

Where, $A_0 = \sqrt{D_0}$ and $B_0 = \exp(-Q/2R)$ are calculated using the relevant data in handbook [143, 144]. In this estimation, a complete mass transfer of N through a 5mm-thick wall of blanket will take about 118 years at 650℃, about 44 years at 700℃, and about 18 years at 750℃, which seems not practical for strengthening of the whole structure.

5.6.2 Hardening and Softening due to Mass Transfer and Aging

Assuming N has almost been trapped by Ti, and all O in Pure V, 60wppm, has been trapped by the Li, the softening of Pure V is estimated to be $0.113 \times 60 \approx 6.8$Hv (See Fig. 4-13). In the measurement, the softening in hardness is 4.0Hv. In the case of tensile test, the yield stress of Pure V decreased by about 55MPa after Li exposure. Both estimations show that there is expected softening due to the loss of O.

STD got a lot of precipitates after Li exposure. The relevant number density is $4.9 \times 10^{21}/\mathrm{m}^3$, and the mean size is 10nm (See Fig. 5-17), contributing an increase in hardness of 23Hv in the center part. To compare with the value measured, which is an increase of about 16Hv, the estimated hardening caused by precipitation in the center part of STD is reasonable.

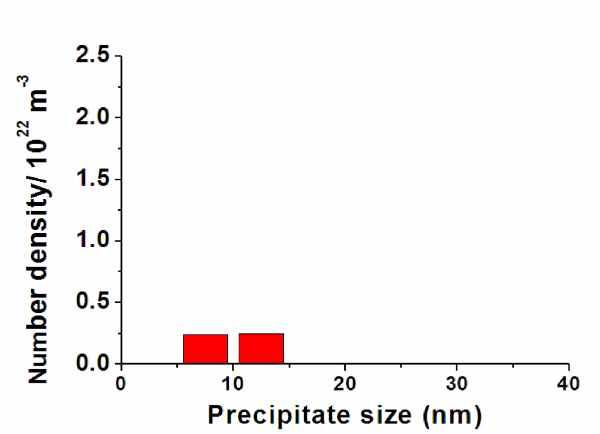

Fig. 5-17 Size distribution of newly formed precipitates in the center part of STD after Li exposure

Figure5-18 shows the size distribution of precipitates in the center part of SAA in initial state (a), after vacuum aging (b) and after Li exposure (c). The precipitation number density in the initial SAA is $2.18\times10^{22}/\mathrm{m}^3$ with a mean size of 4nm, giving a precipitation hardening of 31Hv. After vacuum aging, the number density reduced to $8.0\times10^{20}/\mathrm{m}^3$, and the mean size coarsened to 38nm. Accordingly, the hardening was weakened to be 18Hv, which is a decrease in hardening of 13Hv relative to the calculated hardening for initial SAA. This estimation is reasonable, compared with the measured softening of 20Hv. After Li exposure, the precipitates also coarsened and the corresponding total number density decreased to be $2.28\times$

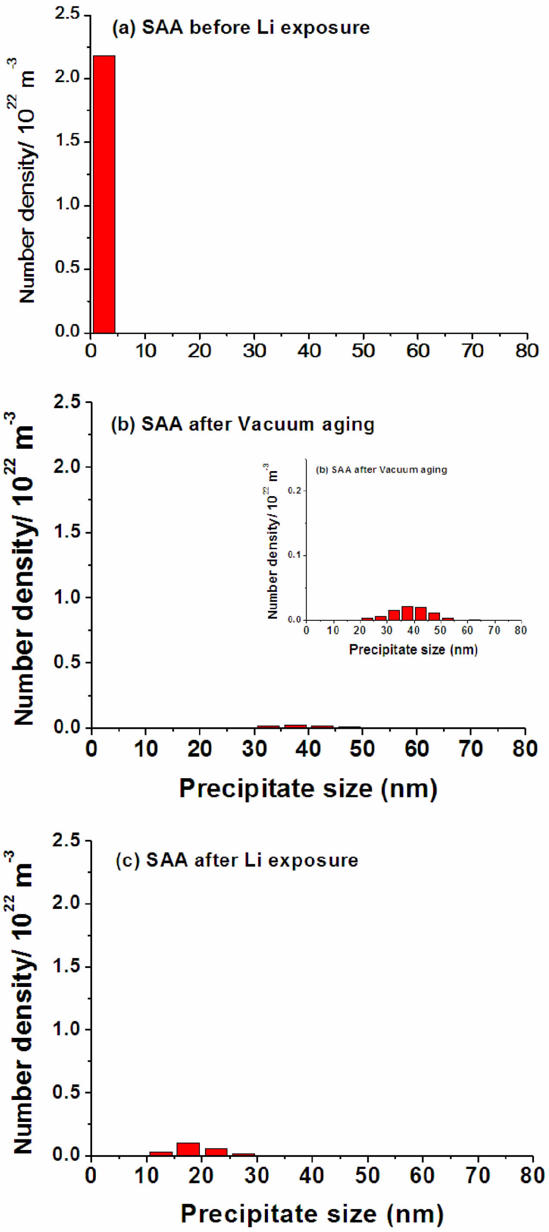

Fig. 5-18 Size distributions of precipitates in center part of (a) SAA in initial state, (b) after vacuum aging and (c) after Li exposure

$10^{21}/m^3$ with a mean size of 20nm. Accordingly, after lithium exposure, the hardening caused by precipitates changed to be 22Hv. This is a decrease in hardening of 9.0Hv relative to the calculated hardening for initial SAA. This estimation is also reasonable, compared with the softening of 12Hv measured for SAA after the Li exposure.

Comparing SAA after Li exposure with after vacuum aging, the softening is common because precipitates coarsened, while the softening after Li exposure is less than that after vacuum aging. The reason is considered to be that in lithium exposure, C can transfer from Li to V-4Cr-4Ti alloy, which makes the alloy harder, while in vacuum aging, this mass transfer does not happen.

The precipitates in SACWA after both vacuum aging and Li exposure are invisible in the observation conditions. However, the change of dislocation density can be observed clearly. Table 5-6 lists the softening and hardening for all the materials with vacuum aging and after Li exposure.

Table 5-6 Expected hardening and softening for Pure V, STD, SAA and SACWA with vacuum aging and after Li exposure (Only show center part)

Material	Lithium exposure (Center part)			Vacuum aging	
Agent	Solution	Precipitation	Dislocation	Precipitate	Dislocation
Pure V	O loss				
	-6.8Hv				
	Total estimated change: -7Hv			Total estimated change: 0Hv	
	Measured change: -4Hv			Measured change: -4Hv	
STD	O loss	Density increase			
	-6.8Hv	+23Hv			
	Total estimated change: +16Hv			Total estimated change: 0Hv	
	Measured change: +16Hv			Measured change: -3Hv	
SAA	O loss	Density decrease		Density decrease	
	-6.8Hv	-9Hv		-13Hv	
	Total change: -16Hv			Total estimated change: -13Hv	
	Measured change: -12Hv			Measured change: -20Hv	
SACWA	O loss	Density decrease	Density decrease	Density decrease	Density decrease
	-6.8Hv	unknown	-7Hv	unknown	-13Hv
	Total estimated change: (unknown-14) Hv			Total estimated change: (unknown-13) Hv	
	Measured change: -15Hv			Measured change: -28Hv	

In initial state SACWA, the dislocation density is measured to be $1.6\times10^{14}/\mathrm{m}^2$. This density changes to be $5.5\times10^{13}/\mathrm{m}^2$ for vacuum-aged SACWA and $1.0\times10^{14}/\mathrm{m}^2$ for Li-exposed SACWA, respectively. In Chapter 4, SACW has an estimated hardening of 47Hv relative to SA, and its dislocation density is $3.8\times10^{14}/\mathrm{m}^2$. According to equation (4-1) and the dislocation number density of each SACWA (in initial, Li-exposed or vacuum-aged state), the hardening caused by dislocations is 31Hv, 18Hv and 24Hv for the initial state, vacuum-aged, and Li-exposed SACWA, respectively. The decrease in dislocation density, to some extent, can account for the decrease in hardness in the center part of SACWA after vacuum aging. Thus vacuum aging caused 13Hv softening for SACWA due to dislocation recovery. Another part of softening is thought to be caused by precipitation coarsening, rather than the change in possible interactions of the precipitates with dislocations. Calculation shows that Li exposure caused 7.0Hv softening for SACWA due to dislocation recovery. Compared with the measured softening of 15Hv, the decrease in precipitate number density could be another possible factor that softens the material.

5.6.3 Creep Mechanism

Converting Fig. 5-12 to the comparison between different treatments for V-4Cr-4Ti alloy, as shown in Fig. 5-19, Li-exposed STD has lower creep rates than SACWA in the present tests below 180MPa, which is similar to the situation of STD and SACWA in initial state. Li-exposed SACWA seems to also have lower creep rates than Li-exposed STD in higher stress region if extent the trend of the curves. This indicates that the creep mechanism for these two treatments may not be changed, though creep resistance has been increased.

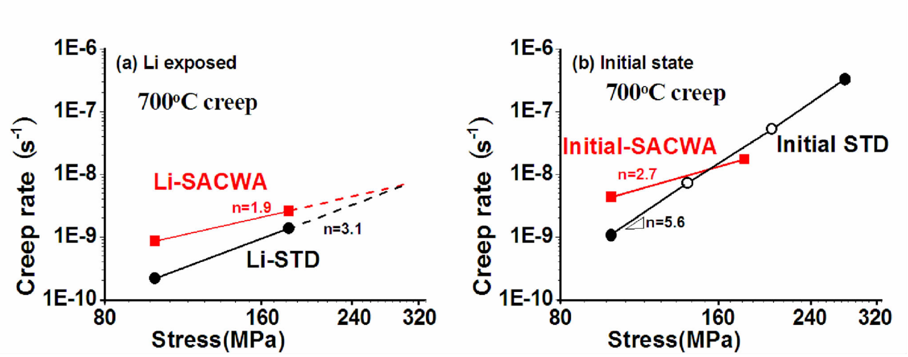

Fig. 5-19 Comparison of creep rates between SACWA and STD in (a) initial state, and (b) Li-exposed states

On the other hand, the minimum creep rates of both Li-exposed STD and Li-exposed SACWA under 100MPa have been decreased by 5 times. For SACWA under 180MPa, the creep rate was reduced by about 7 times after Li exposure. Currently, it is not clear how many times of decrease in the minimum creep rate will be for Li-exposed STD under 180MPa, however, the estimation from Fig. 5-12 (a) comes that the decrease would be about 20 times. In other words, when the stress component "n" gets smaller, with the same creep mechanism, the minimum creep rate under higher stress will decrease more. This decrease indicates larger number density of precipitates could extend the advantage of STD over SACWA to higher stress region, in the creep resistance point of view.

5.7 Summary

The present study investigated the effects of Li exposure on mechanical properties of V-4Cr-4Ti alloy with different treatments. The effects of alloying element on mass transfer has been discussed. The effects of mass transfer and aging during Li exposure on mechanical property have been clarified. Follows are the summary for this study:

(1) O can transfer from V-4Cr-4Ti matrix to liquid Li, while N and C can transfer from liquid Li to V-4Cr-4Ti matrix.

(2) The mass transfers of impurities are based on chemical affinity and thermodynamic equilibrium conditions.

(3) The trapping of N and C into the V-4Cr-4Ti alloy is due to the strong chemical affinity of them with Ti.

(4) Thermal diffusion is the basic way for C, O and N mass transfers.

(5) Li exposure includes both mass transfer effects which helps forming new precipitates and aging effects which causes dislocation loss and precipitate coarsening. The identification of mechanical property change due to mass transfer and aging effects are listed in Table 5-7.

Table 5-7 Mechanical property change due to mass transfer and aging effects for Pure V, STD, SAA and SACWA (Main reasons for the change are included)

	Li exposure (center)	**Li exposure (surface)**	**Vacuum aging**
Pure V	**Softened** O diffuse into Li	**Softened** O diffuse into Li	**No obvious change**
STD	**Hardened** C trapped by Ti	**Hardened** C and N trapped by Ti	**No obvious change**
SAA	**Softened** Precipitates coarsened	**Hardened** C and N trapped by Ti	**Softened** Precipitates coarsen
SACWA	**Softened** Dislocations decrease	**Hardened** C and N trapped by Ti	**Softened** Dislocation decrease

(6) C-rich Ti-(C,O,N) precipitates have higher thermal stability than O-rich Ti-(C,O,N).

(7) The creep rate of V-4Cr-4Ti alloy has been largely decreased due to precipitation hardening after Li exposure.

(8) The precipitates with large number density could extend the advantage of STD over SACWA to higher stress region, in creep resistance point of view.

This study again confirms that the higher number density of thermally stable precipitates with fewer dislocations is a key factor to strengthen V-4Cr-4Ti alloy at elevated temperatures.

CHAPTER 6

Mechanical alloying for strengthening V-4Cr-4Ti alloys with Y addition

6.1 Mechanism of Strengthening by Mechanical Alloying

Mechanical alloying (MA) is a powder processing technique involving repeated cold welding, fracturing, and re-welding of powder particles in a high-energy ball mill which allows production of homogeneous materials starting from blended elemental powder mixtures [145].

The nature of mechanical alloying is that the collision energy activates the bonding of different atoms when the powders are milled to small sizes and mixed uniformly in atomic scale. Refined pre-alloy or mixture of pure metal powders can both be the starting material for MA. Dispersion particles can either be added from outside or formed in alloy matrix. The present study uses pure metal powders as starting material and adds dispersion particles from the outside. As to the strengthening of alloys by MA, grain size refining and nanoparticle dispersion strengthening are two coexisting mechanisms.

During MA process, the loss of kinetic energy from the balls is converted to heat and inner energy of the powders. Unbonded atoms will absorb energy during this period and form various bonds including metallic bond and electrovalent bond, thus form alloy and compounds during the MA process. Moreover, in the following HIPing, thermal diffusion of atoms additionally helps reactions of the alloying elements with interstitial impurities to form small particles, and further benefits homogeneous distribution of the alloying elements. These small particles are usually in nano-meter scale, and can act as obstacles to resist dislocation motions.

The nanoparticle dispersion strengthening of materials shares the same mechanism with precipitation hardening. The simplified equation of this mechanism for yield stress was shown in equation (4-4).

The key parameters of nano-particle dispersion strengthening are the number density and size of the particles. If the volume fraction of nanoparticles is sustained, to increase number density should be a favorable effort.

Because of collision, the powders are deformed, which introduce high density of dislocations, and the kinks of dislocations finally join together as grain boundaries in HIPing. Thus the grain sizes are refined with the increasing milling time. Experiments show that for most metals, smaller grain size leads to higher yield stress (Refer to equation (6-1)) [146, 147].

$$\Delta\tau = K' \cdot \Delta d'^{-\frac{1}{2}} \tag{6-1}$$

Where τ is the yield stress, K' is a constant related to the material, and d' is the average diameter of the grains in a material. If convert the above equation to show the dependence of hardness on grain size, similar Hall-Petch equation (6-2) can be obtained.

$$\Delta Hv = k' \cdot \Delta d'^{-\frac{1}{2}} \tag{6-2}$$

Where Hv stands for the hardness value, k' is a constant related to the material by converting shear stress to hardness. This value can be calculated from experimental data.

Considering thermal creep strength not only depends on yield stress of a material, the above strengthening mechanisms should be directed toward an optimized situation. For example, although small grain size can enhance creep deformation, the post-annealing after HIPing can lead to coarsening of the grains and introduce more nanoparticles. This can both resist deformation on grain boundary and the dislocation motion in matrix.

6.2 Experiment

The general material preparation is shown in Fig. 6-1 below. The first step is to prepare the starting material (powders). Then, the second step is to mill the powders. The following is hot iso-static pressing (HIP), and the final step is sample machining with some other post treatments.

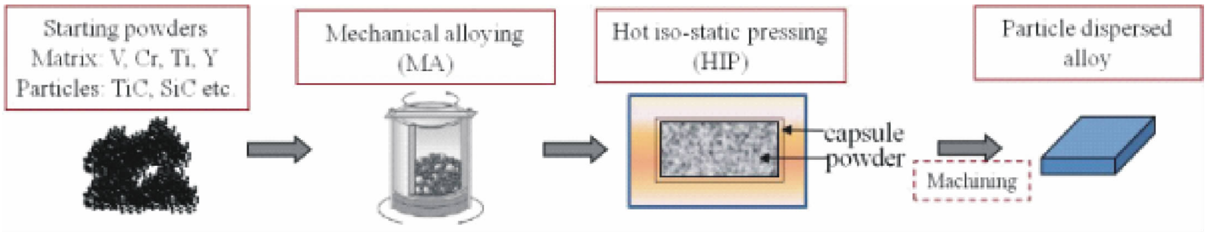

Fig. 6-1 Mechanical alloying procedure

In the present study, the starting material used includes vanadium powders (99.9%, 100 mesh), chromium powders (99.9%, 100 mesh), titanium powders (99.9%, 100 mesh), yttrium powders (99.9%, 20 mesh), TiC particles (99.5%, ~200 mesh) as well as SiC particles (99.5%, ~200 mesh) from Furuuchi chemical corporation and Ti_3SiC_2 particles (~99.5%, ~200 mesh) supplied by Wuhan University of Technology in China. The reason to choose these carbides is that TiC has already been used as dispersion particles for strengthening vanadium alloys [102, 109]; SiC is the composition of a structural material, SiC_f/SiC composites; and Ti_3SiC_2 can be considered as a mixture of TiC and SiC, however the crystal structure of these carbides are different. The chemical compositions of the impurities in the metal powders and carbide particles are listed in Table 6-1. Note the impurity levels of Ti_3SiC_2 are not available.

The necessary amount of yttrium addition is designed depending on the O and N impurity levels in the starting powders, which is set to be 1.5 wt% in this study, assuming most O and N are scavenged by Y to the form yttrium oxides and nitrides. The powders are mixed to compositions of V-4Cr-4Ti-1.5Y-0.3XC in a helium atmosphere, where XC is one of TiC, SiC and Ti_3SiC_2 carbides.

A Fritsch PULVERISETTE 7 premium line (Fig. 6-2) is used as the milling equipment. Firstly, the present study investigates the milling ability of Si_3N_4 balls and vessels for V powders. The volume of each Si_3N_4 vessel is 20ml; volume ratio of the balls together with the powders to vessel varies from 1/3 to 2/3; weight ratio of balls to the powders varies from 5/2 to 10/1 and the rotation speed varies from 350rpm to 750rpm. Details of the milling parameters are listed in Table 6-2.

Table 6-1 Chemical compositions of impurities in starting powder and particles

	Chemical compositions (wt%)						
	V	Cr	Ti	Y	TiC	SiC	Ti_3SiC_2
O	0.348	0.08	0.137	—	0.79	<0.15	—
N	0.046	0.019	0.002	—	—	—	—
C	0.013	0.005	0.004	—	/	/	/
H	0.010	—	0.014	—	—	—	—
Mo	0.001	—	—	—	—	—	—
Fe	0.009	<0.1	0.005	<0.02	0.05	<0.35	—
Si	0.021	0.002	<0.01	—	—	/	/
Al	0.015	0.001	—	—	—	—	—
Mn	—	—	<0.001	—	—	—	—
Mg	—	—	0.007	<0.01	—	—	—
Cl	—	—	0.026	—	—	—	—
P	—	0.001	—	—	—	—	—
S	—	0.019	—	—	—	—	—
Pb	—	0.001	—	—	—	—	—
Cu	—	0.0004	—	—	—	—	—
Ca	—	—	—	<0.01	—	—	—
Gd	—	—	—	<0.01	—	—	—
Tb	—	—	—	<0.01	—	—	—
Dy	—	—	—	<0.01	—	—	—
Er	—	—	—	<0.01	—	—	—

The main fabrication in the present study uses a set of milling vessels and balls made of WC/Co. The ball size is 5mm in diameter with a weight of about 1.0g, the volume of each vessel used is 45ml; volume ratio of ball plus powder to the vessel is 1:4; and the weight ratio of balls to powders is 5:1 as shown below.

$$\text{Volume ratio:}\frac{v_{balls}+v_{powders}}{v_{vessel}}=\frac{1}{4};\qquad \text{Weight ratio:}\frac{w_{balls}}{w_{powders}}=5.$$

Thus the weight of each powder and particles is precisely measured as following:

V, 19.955g;

Cr, 0.882g;

Ti, 0.882g;

Y, 0.331g;

and powders of each carbide (TiC, SiC or Ti_3SiC_2) weight 0.066g.

The total weight of the starting powders is about 22.116g, and the weight of the WC/Co balls is around 110g.

Table 6-2 List of milling by Si_3N_4 balls

No.	ID	Compositions	Time			Rotation speed
①	1/3,5:1,350rpm	V	60hrs	1/3	5	350rpm
②	1/2,5:1,350rpm	V	30hrs	1/2	5	350rpm
③	2/3,5:1,350rpm	V	90hrs	2/3	5	350rpm
④	2/3,5:2,550rpm	V	40hrs	2/3	5/2	550rpm
⑤	1/3,5:2,650rpm	V	12hrs	1/3	5/2	650rpm
⑥	1/2,5:1,650rpm	V	12hrs	1/2	5	650rpm
⑦	2/3,5:1,650rpm	V	40hrs	2/3	5	650rpm
⑧	2/3,10:1,650rpm	V	40hrs	2/3	10	650rpm
⑨	1/3,5:2,750rpm	V	10hrs	1/3	5/2	750rpm
⑩	2/3,5:2,750rpm	V	10hrs	2/3	5/2	750rpm
⑪	-TiC,Si_3N_4,4hr(HIPed)	V-4Cr-4Ti-1.5Y-0.3TiC	4hrs	2/3	5	650rpm

Fig. 6-2 Mill used in the present study

The packing of powders and milling balls along with the sealing of vessels are performed in a glove box. Pure helium gas (> 99.9999%) with continuous purification is used. The O level is lower than 1 ppm and the moisture level is below 0.1 ppm. After packing, the vessels are set in the mill outside of the glove box. A milling speed of 340 rotations per minute (rpm) is used for the present study. In case lots of pastes (films formed when powders are bonded) might form on milling balls and the inner wall of the vessels, the mill was paused every other minute for cooling. After every 30 minutes, the vessels are transferred into the glove box again and opened in helium atmosphere. Then the thin pastes are peeled from inner wall of the vessel and are mixed into the remaining powders again. After MA process is completed for a material, W powders (~74μm) are used to polish the balls and vessel wall to remove the pastes.

In order to get a systematic research on V-4Cr-4Ti alloy with MA process, the present study investigated the particle dependence and time dependence on the mechanical properties of V-4Cr-4Ti alloys milled with WC/Co balls and vessels. The arrangement for this alloy series is listed in Table 6-3 below. Note sample $\boxed{1}$ contains neither Y nor carbides, the word "base" in its ID category stands for V-4Cr-4Ti; and all the other materials contain the same amounts of V, Cr, Ti and Y. The carbide names and milling time in the ID category are used for distinguishing purpose.

Table 6-3 List of materials fabricated with WC/Co balls

No.	ID	Compositions	MA process time
$\boxed{1}$	base, 10hr	V-4Cr-4Ti	10 hrs (not HIPed)
$\boxed{2}$	-TiC, 2hr	V-4Cr-4Ti-1.5Y-0.3TiC	2 hrs
$\boxed{3}$	-TiC, 4hr	V-4Cr-4Ti-1.5Y-0.3TiC	4 hrs
$\boxed{4}$	-TiC, 10hr	V-4Cr-4Ti-1.5Y-0.3TiC	10 hrs
$\boxed{5}$	-TiC, 20hr	V-4Cr-4Ti-1.5Y-0.3TiC	20 hrs
$\boxed{6}$	-TiC, 40hr	V-4Cr-4Ti-1.5Y-0.3TiC	40 hrs
$\boxed{7}$	-Ti_3SiC_2, 4hr	V-4Cr-4Ti-1.5Y-0.3Ti_3SiC_2	4 hrs
$\boxed{8}$	-Ti_3SiC_2, 10hr	V-4Cr-4Ti-1.5Y-0.3Ti_3SiC_2	10 hrs
$\boxed{9}$	-Ti_3SiC_2, 40hr	V-4Cr-4Ti-1.5Y-0.3Ti_3SiC_2	40 hrs
$\boxed{10}$	-SiC, 4hr	V-4Cr-4Ti-1.5Y-0.3SiC	4 hrs

During the milling procedure, small amount of the alloyed powders with TiC and Ti_3SiC_2 are used for XRD analysis to study the lattice change within 0-40hrs and the phase evolution.

Among these powders, $\boxed{1}$, $\boxed{2}$, $\boxed{3}$ and the starting material of $\boxed{2}$ (or $\boxed{3}$) are used in EDX line analysis to study element distribution. Element distributions of HIPed V-4Cr-4Ti-1.5Y-0.3TiC with 2-40hrs ($\boxed{2}$, $\boxed{3}$, $\boxed{4}$, $\boxed{5}$ and $\boxed{6}$) milling are analyzed with EDX area mapping. The arrangements and status of EDX analysis in the present study are listed in Table 6-4.

The remaining powders are filled into HIPing capsules made of low carbon steel SS400 with yield stress of 235MPa and total elongation of 20% at RT. The chemical compositions of SS400 are shown in Table 6-5. It is considered that this steel is suitable for the HIPing of vanadium alloy because of low impurity levels and low activation property of the elements.

The design of HIPing capsules has taken into consideration of sample arrangements and size shrinkage of the capsules. The scheme of the capsule cross-section is as shown in Fig. 6-3. The cross section is enough for 2 tensile/creep specimens and 2 or more TEM specimens. The design for the capsules is as shown in Fig. 6-4. The inner diameter of each capsule is 24mm, the length is 45mm, and the thickness of its wall and cover cap is 1mm. A groove is cut for gas flow during the pumping.

Table 6-4 EDX analysis for mechanically-alloyed material in the present study

Samples used in EDX analysis	Accomplishment (Line scan during MA)	Accomplishment (Area mapping after HIP)
Base, 10hr	Successful	Not planned
-TiC, 0hr (starting powder)	Successful	Not planned
-TiC, 1hr (midway of "TiC, 2hr")	Successful	Not planned
-TiC, 2hr	Successful	Successful
-TiC, 4hr	Successful	Successful
-TiC, 10hr	Failed	Successful
-TiC, 20hr	Failed	Successful
-TiC, 40hr	Successful	Successful
-Ti_3SiC_2, 10hr	Successful	Not planned

Table 6-5 Chemical compositions (%) of SS400 steel for HIPing capsule

Fe	C	Si	Mn	P	S
Bal.	0.15	0.2	0.5	0.017	0.021

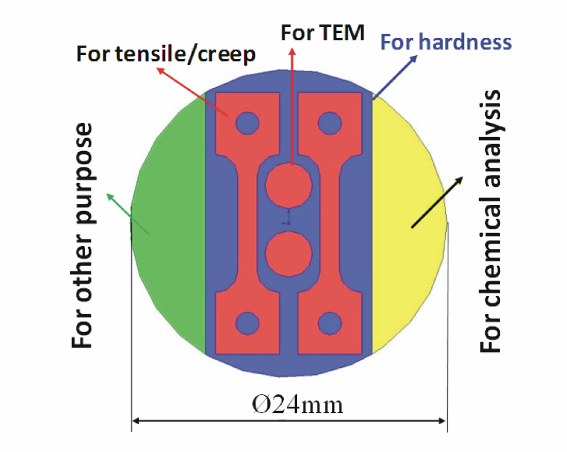

Fig. 6-3 Arrangement of samples in the capsule

Fig. 6-4 Design of HIPing capsule

In order to compact the powders, a cold press tool (Fig. 6-5 (a)) is designed based on a precise vise (Fig. 6-5 (b)). With this tool and two spacers also made of SS400 in the capsule, the prepared powders are cold-pressed at first to avoid large shrinkage on the capsule during HIPing. Thus, more samples can be obtained.

The canned capsules are kept in a vacuum container as shown in Fig. 6-6 in order to be transported to electric beam (EB) welding chamber. This design aims to let the vacuum container open automatically when suitable vacuum has been achieved in EB welding chamber. Pumping for vacuum is carried out in glove box so that it can avoid impurities from the air, such as O, N and so on.

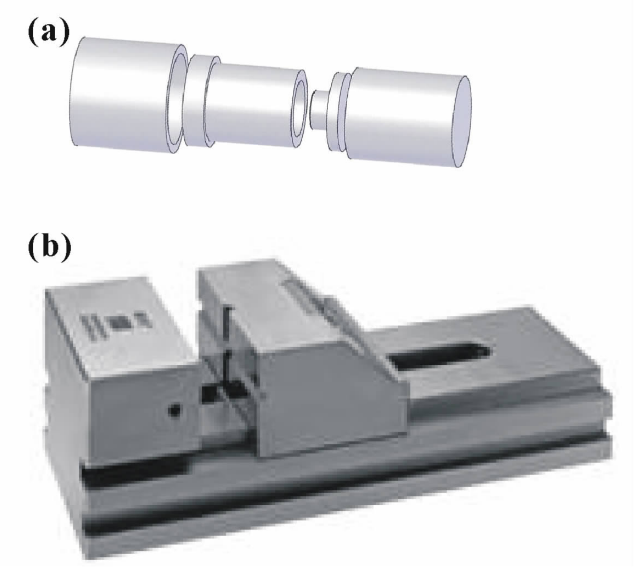

Fig. 6-5 Design of cold-press tool and the vise

Fig. 6-6 Vacuum container for transporting packed capsules

The welded capsules as shown in Fig. 6-7 are then transferred for hot iso-static pressing (HIP).

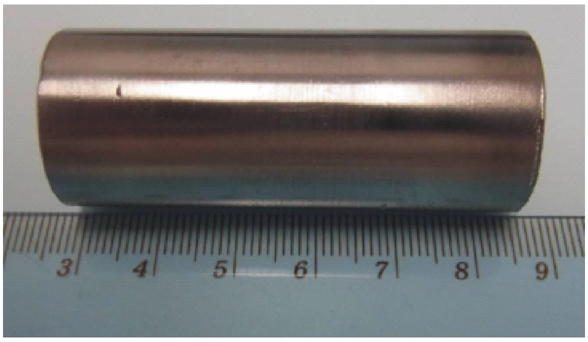

Fig. 6-7 Capsule before HIPing

The HIPing process is carried out in Ar atmosphere under 191MPa at 1000℃ for 3 hrs. The temperature and pressure are increased in parallel with a heating speed of 300℃ per hour. After HIPing, the furnace was cooled down in about 2 hrs. The sketch map of HIPing device and the HIPing history in the present study can be found in Fig. 6-8.

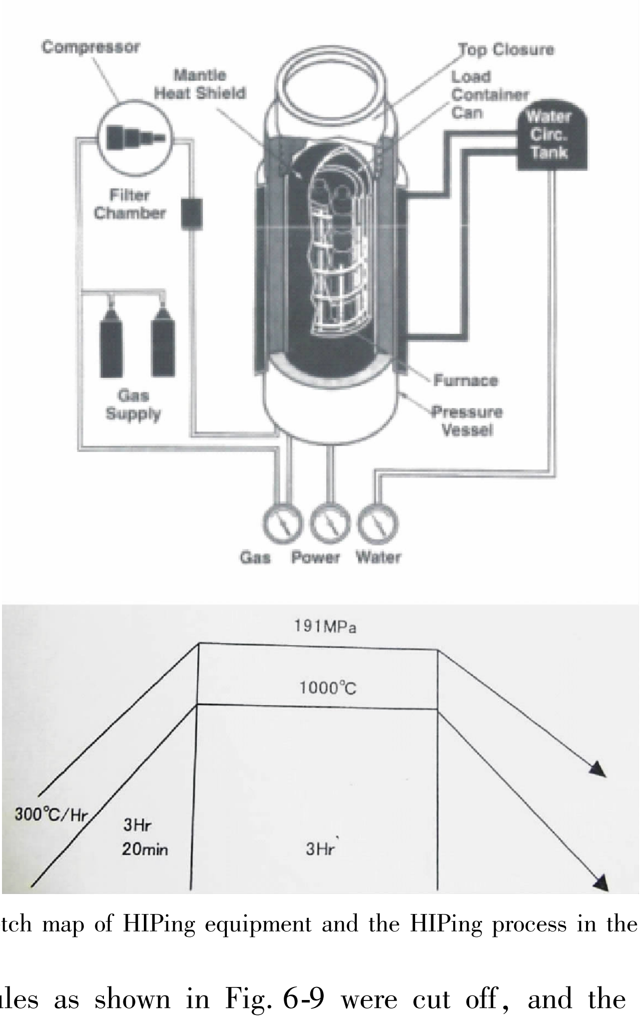

Fig. 6-8 Sketch map of HIPing equipment and the HIPing process in the present study

The HIPed capsules as shown in Fig. 6-9 were cut off, and the alloy bulks were then peeled out from the capsules.

Tensile specimens and TEM specimens are machined by wire cutting at first, and then be polished to remove the oxidized layer from the surface. An annealing is carried out at 1200℃

for 1hour in a vacuum better than 1 × 10^{-6} Torr. Hardness is measured for the as-HIPed samples and the annealed samples, high temperature tensile properties are tested at 750℃ for the 2 ~ 4-hour-milled alloys, and creep tests for "-TiC, 40hr" after annealing are performed at 700℃ with stresses of 100MPa and 280MPa.

Successful post-treatments and characterizations for all the specimens are shown in Table 6-6 below.

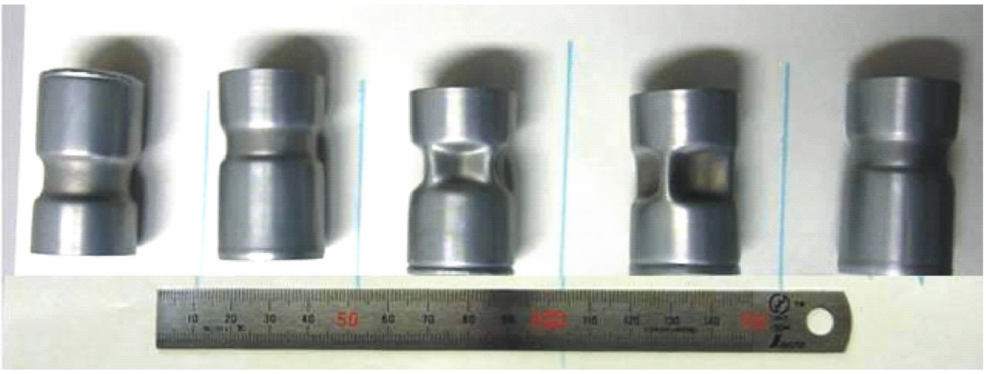

Fig. 6-9 Example of HIPed capsules

Table 6-6 Arrangements of post-treatments and characterizations for MA samples

Material	**As-HIPed**	**1200℃ ×1hr**
-TiC, 2hr	Hardness, 750℃ tensile test	Hardness, 750℃ tensile test
-TiC, 4hr	Hardness, 750℃ tensile test, SEM (to observe grain), TEM/EDX (for nanoparticles)	Hardness, 750℃ tensile test, SEM (to observe grain), TEM/EDX (for nanoparticles)
-SiC, 4hr	Hardness, 750℃ tensile test, SEM (to observe grain)	Hardness, 750℃ tensile test, SEM (to observe grain), TEM (for nanoparticles)
-Ti_3SiC_2, 4hr	Hardness, 750℃ tensile test, SEM (to observe grain)	Hardness, 750℃ tensile test, SEM (to observe grain) TEM (for nanoparticles)
-TiC, 10hr	Hardness,	Hardness,
-TiC, 20hr	Hardness,	Hardness,
-TiC, 40hr	Hardness, TEM/EDX (for grains and nanoparticles)	Hardness, 700℃ creep test (100-280MPa), TEM/EDX (for grains and nanoparticles)
-Ti_3SiC_2, 10hr	Hardness,	Hardness,
-Ti_3SiC_2, 40hr	Hardness,	Hardness,
-TiC, Si_3N_4, 4hr	Hardness, 750℃ tensile test	Hardness, 750℃ tensile test

6.3 Mechanical Alloying Process

6.3.1 Evaluation of Milling Balls

During the milling process for V powders with Si_3N_4 balls, the starting powders gain weight all the time due to weight-loss of the balls. Figure 6-10 (a) shows the weight ratio of ball loss to V powders during MA process under different milling conditions. The loss of ball weight generally increases linearly with increasing process time. In detail, when the rotation speed is the same, lower "ball + powder to vessel volume ratio" leads to more weight loss. When the "ball + powder to vessel volume ratio" is the same, higher rotation speed leads to more weight loss. The lost part of the Si_3N_4 balls is considered to be mixed into V powders. Among all the test conditions using Si_3N_4 balls, the one with "ball + powder to vessel volume ratio" of 2:3, ball to material weight ratio of 5:1 at 650rpm gains relatively acceptable production of alloy powders, and has higher collision energy and comparatively lower contamination, but which is still as high as 1.36%.

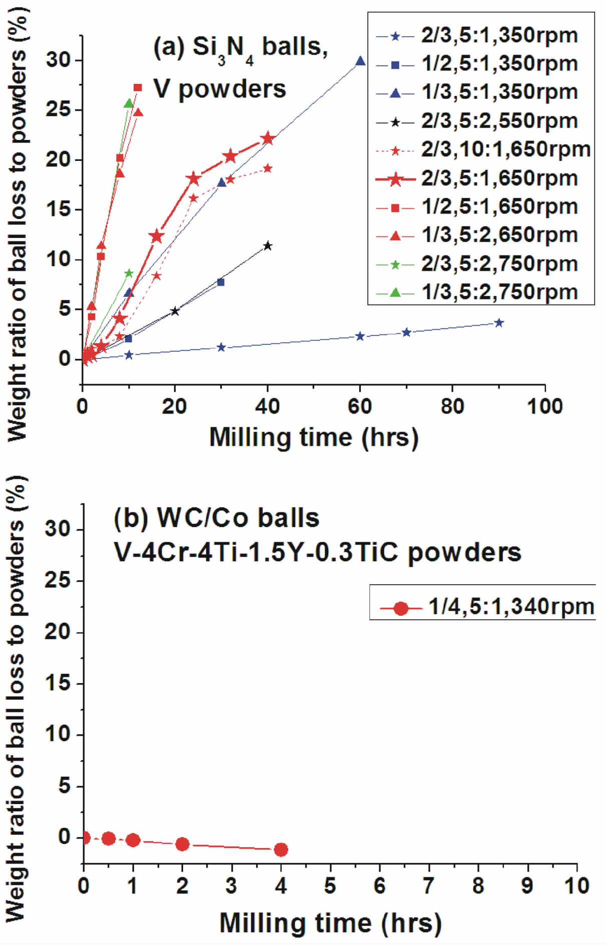

Fig. 6-10 Weight ratio of ball loss to starting powders during MA for (a) V powder and Si_3N_4 ball system, and (b) V-4Cr-4Ti-1.5Y-0.3TiC with WC/Co ball system

In the case of milling with WC/Co balls, the starting powders are changed to be V-4Cr-4Ti-1.5Y-0.3TiC. Unlike the case of Si_3N_4 balls, the WC/Co balls gain weight instead, as shown in Fig. 6-10 (b), which is from the starting powders. Alloying occurs obviously in the present MA condition with WC/Co balls. Cold welding of starting powders happens on the surfaces of the WC/Co balls, which results in paste.

6.3.2 Characterization of Alloying Elements

Figure 6-11 shows the element distribution of Y, Cr and Ti in V matrix analyzed with EDX line scan after different MA time. Fig. 6-11 (a), Fig. 6-11 (b) and Fig. 6-11 (c) are for V-4Cr-4Ti-1.5Y-0.3TiC powder system with 0hr-MA, 2hr-MA and 4hr-MA, respectively. Fig. 6-11 (d) is for V-4Cr-4Ti with10hr-MA. At 0 hour (Fig. 6-11 (a)), peaks exist for all Cr, Ti and Y. Till 2hr (Fig. 6-11 (b)), Y peaks almost disappeared, indicating Y dissolves in V powders the fastest. Till 4 hr (Fig. 6-11 (c)), Cr peaks almost disappeared, with Ti peak existing alone, indicating that the Cr dissolves into V powders faster than Ti. This dissolution sequence of Cr followed by Ti seems not affected by the absence of Y as shown in Fig. 6-11(d). Though high Ti concentration area has been shrunk after 10hr-MA, the time for complete disappearance of Ti peak is expected to be longer than 10 hrs.

On the other hand, in the area mapping for Y, Cr and Ti distributions in V matrix of V-4Cr-4Ti-1.5Y-0.3TiC system with the same MA and HIPing conditions, as shown in Fig. 6-12, complete dissolution of Cr and Ti have been extended to 20 hrs and 40 hrs, respectively. Still, it shows that Y dissolves faster than Cr, and Cr dissolves faster than Ti.

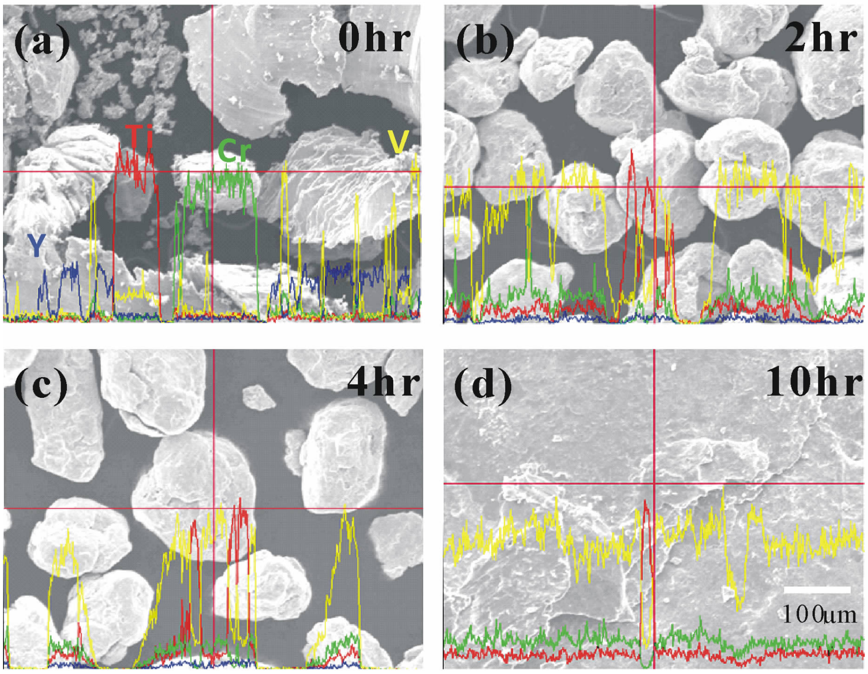

Fig. 6-11 Element distributions of Y, Cr, Ti in V powder in EDX ling scanning, with the MA time of (a) 0hr, (b) 2hrs, (c) 4hrs for V-4Cr-4Ti-1.5Y-0.3TiC powder system, and (d) 10hrs for V-4Cr-4Ti powder system

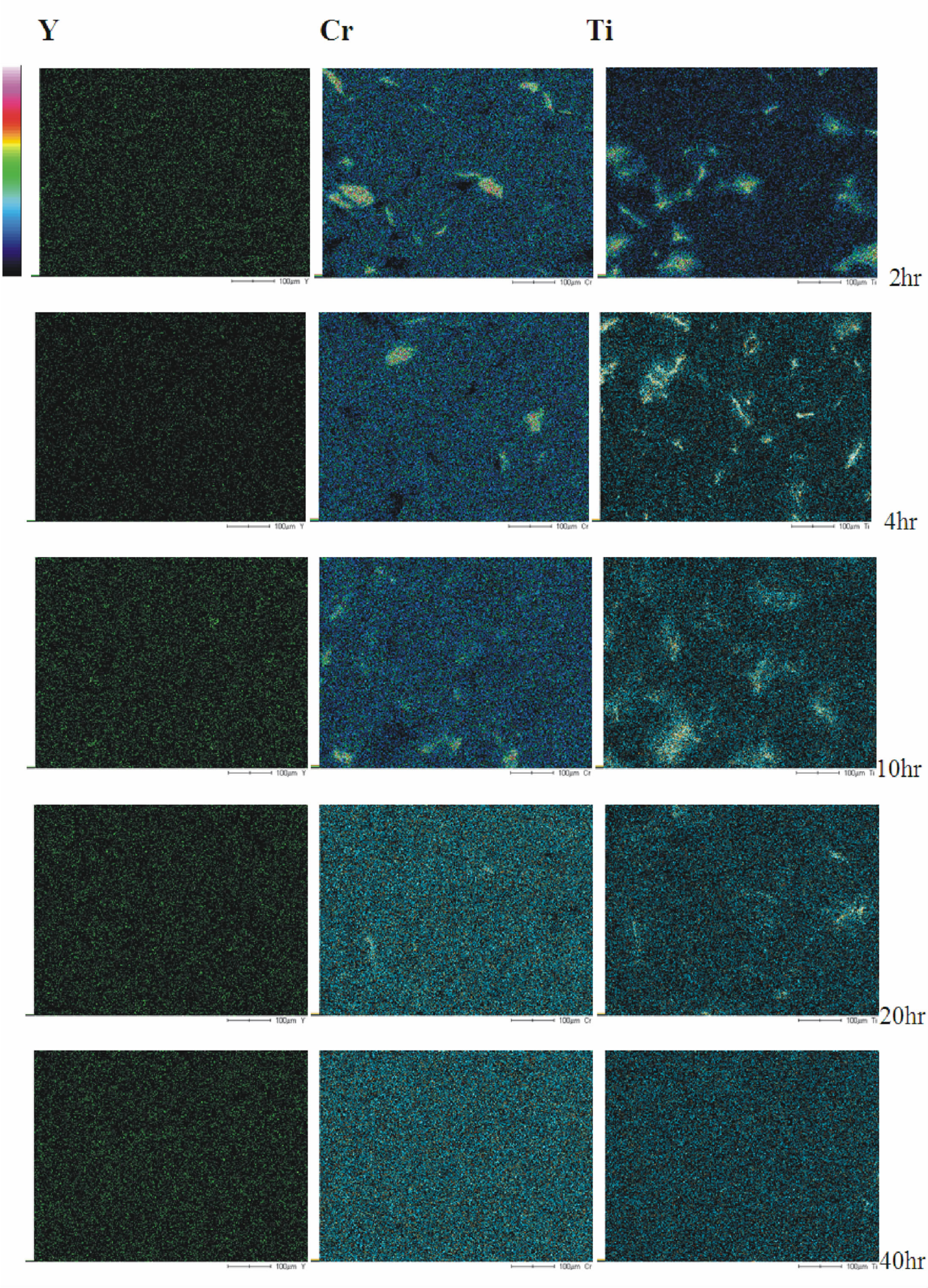

Fig. 6-12 Element distributions of Y, Cr and Ti in V matrix after MA and HIPing for V-4Cr-4Ti-1.5Y-0.3TiC system in EDX mapping, with the MA time of (a) 2hrs, (b) 4hrs, (c) 10hrs, (d) 20hrs, and (e) 40hrs

6.3.3 Characterization of V Lattice.

Figure 6-13 shows the shift of V (1 1 0) peak of V-4Cr-4Ti-1.5Y-0.3TiC system in X-ray Diffraction (XRD) analysis. Samples are taken during MA process with a processing time of 0 hr, 1hr, 2hrs, 4hrs and 40hrs. V-4Cr-4Ti-1.5Y-0.3Ti_3SiC_2 powders milled for 10 hrs are also used, because the V-4Cr-4Ti-1.5Y-0.3TiC powders are lack. Note the powders with 1 hr milling is fetched halfway during the 2-hour milling process. From 0hr to 1hr, the peak shifts toward lower angle. Then at 2hr, the peak shifts back to higher angle. However, from 2hr to 40hr, the peak keeps shifting to lower angle continuously. This shift has been converted into lattice change of V matrix by applying the Bragg relationship, as shown in equation (6-3).

$$2d'' \times \sin\theta = n\lambda \tag{6-3}$$

Where, d'' is the lattice distance of (110) plane of V matrix. The converted change in lattice parameter, which is $d''/\sqrt{1^2+1^2+0^2}$, has been plotted in Fig. 6-14 below.

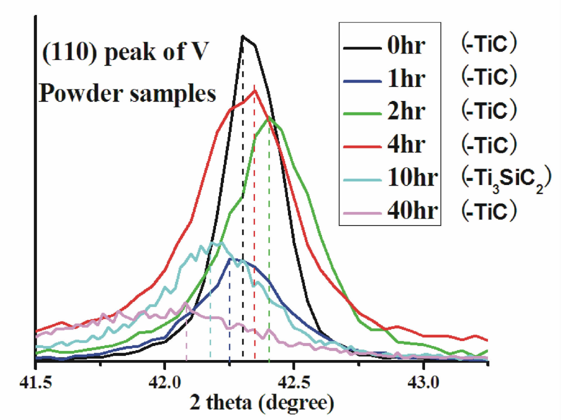

Fig. 6-13 The shift of V (100) peak during MA process

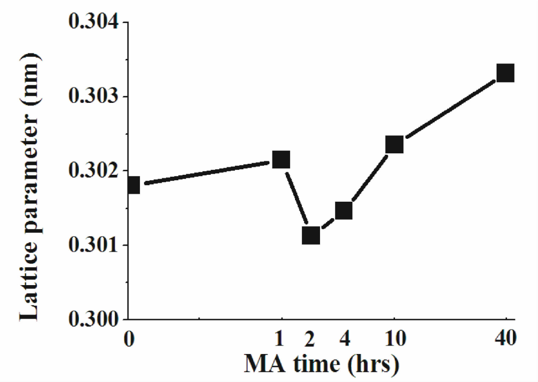

Fig. 6-14 Change of lattice parameter of V matrix during MA process from 0hr to 40hrs

The trend shows that from 0hr to 1hr, the lattice parameter has an expansion by 3.5×10^{-4} nm; from 1hr to 2hr, there is a lattice shrinkage by 10.2×10^{-4} nm; and from 2hr to 40hr, a cumulative value of the continuous lattice expansion by 21.8×10^{-4} nm is obtained. Unfortunately, the starting point value is smaller than the value from the vanadium database because of setting failure of the XRD equipment. However, the trend of lattice change is not affected by this failure. Thus the value for lattice change can still be used to evaluate the lattice change in the MA process.

6.3.4 Phase Evolution

Figure 6-15 shows the phase evolution of as-HIPed V-4Cr-4Ti-1.5Y-0.3TiC (a) and as-HIPed V-4Cr-4Ti-1.5Y-0.3Ti_3SiC_2 (b) with different MA time. From 4hr, Y_2O_3 peaks and TiN peaks are the main peaks that exist for the rest of the time. Cr and Ti peaks are weakened in MA process. There are some contaminations detected such as W and Co from the milling balls. Comparing with TiC, Ti_3SiC_2 survives even after 40hrs of MA, seeming to have higher stability.

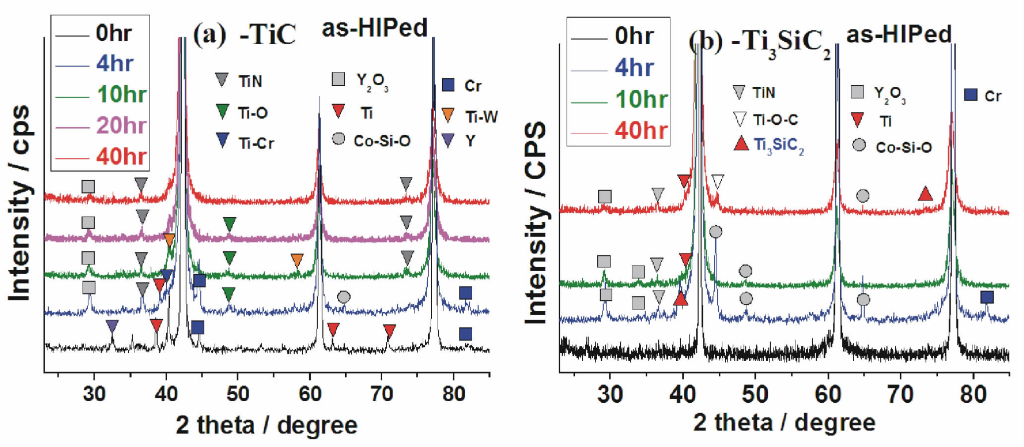

Fig. 6-15 Phase evolution of (a) HIPed V-4Cr-4Ti-1.5Y-0.3TiC and (b) V-4Cr-4Ti-1.5Y-0.3Ti_3SiC_2 alloys with different MA time

6.4 Chemical Analysis

Table 6-7 shows chemical compositions of all mechanically alloyed V-4Cr-4Ti alloys with Y and carbide additions after HIPing. Weight percent change of common contaminants such as O, N and C and the main contaminants from the milling balls such as Si and W are plotted in Fig. 6-16 for WC/Co-ball-milled alloys. In the alloys milled for 2-4 hrs, the concentrations of alloying elements such as Ti and Y are close to the designed values, while the Cr concentrations are much lower than the designed value. The reason is unknown yet.

Table 6-7 Chemical compositions of mechanically-alloyed V-4Cr-4Ti with Y additions after HIP

ID	Chemical Composition (wt%)									
	V	Cr	Ti	Y	W	Co	Si	O	N	C
-SiC, WC, 4hr	Bal.	1.87	3.95	1.43	0.09	<0.02	–	0.46	0.088	0.14
-TiC, WC, 2hr	Bal.	1.74	4.15	1.43	<0.02	<0.02	–	0.44	0.053	0.12
-TiC, WC, 4hr	Bal.	2.09	4.17	1.48	0.02	<0.02	–	0.50	0.11	0.09
-TiC, WC, 10hr	Bal.				1.13	0.01	0.03	0.36	0.12	0.15
-TiC, WC, 20hr	Bal.				1.12	0.03	0.04	0.39	0.16	0.16
-TiC, WC, 40hr	Bal.				1.11	0.08	0.05	0.46	0.23	0.23
-Ti_3SiC_2, WC, 4hr	Bal.	1.22	4.23	1.49	<0.02	<0.02	–	0.043	0.045	0.11
-Ti_3SiC_2, WC, 10hr	Bal.				0.03	0.05	0.06	0.35	0.12	0.10
-Ti_3SiC_2, WC, 40hr	Bal.				0.66	–	0.09	0.44	0.33	0.17
-TiC, Si_3N_4, 4hr	Bal.	1.35	4.05	1.46	–	–	–	0.79	0.65	0.10

It is worth noting that the high W concentrations up to 0.66-1.13% may mainly come from W powders which are used to polish the paste on milling balls. Some of the W powders remained on the balls after polishing, and then, they can be mixed into the next alloy powders. Data show that the concentration of Co increases with the increasing MA time, Si concentration for the alloy milled by Si_3N_4 balls is not available, however there is an apparent increase of N for this alloy, which indicates an increase in Si concentration can be due to the loss of Si_3N_4 balls.

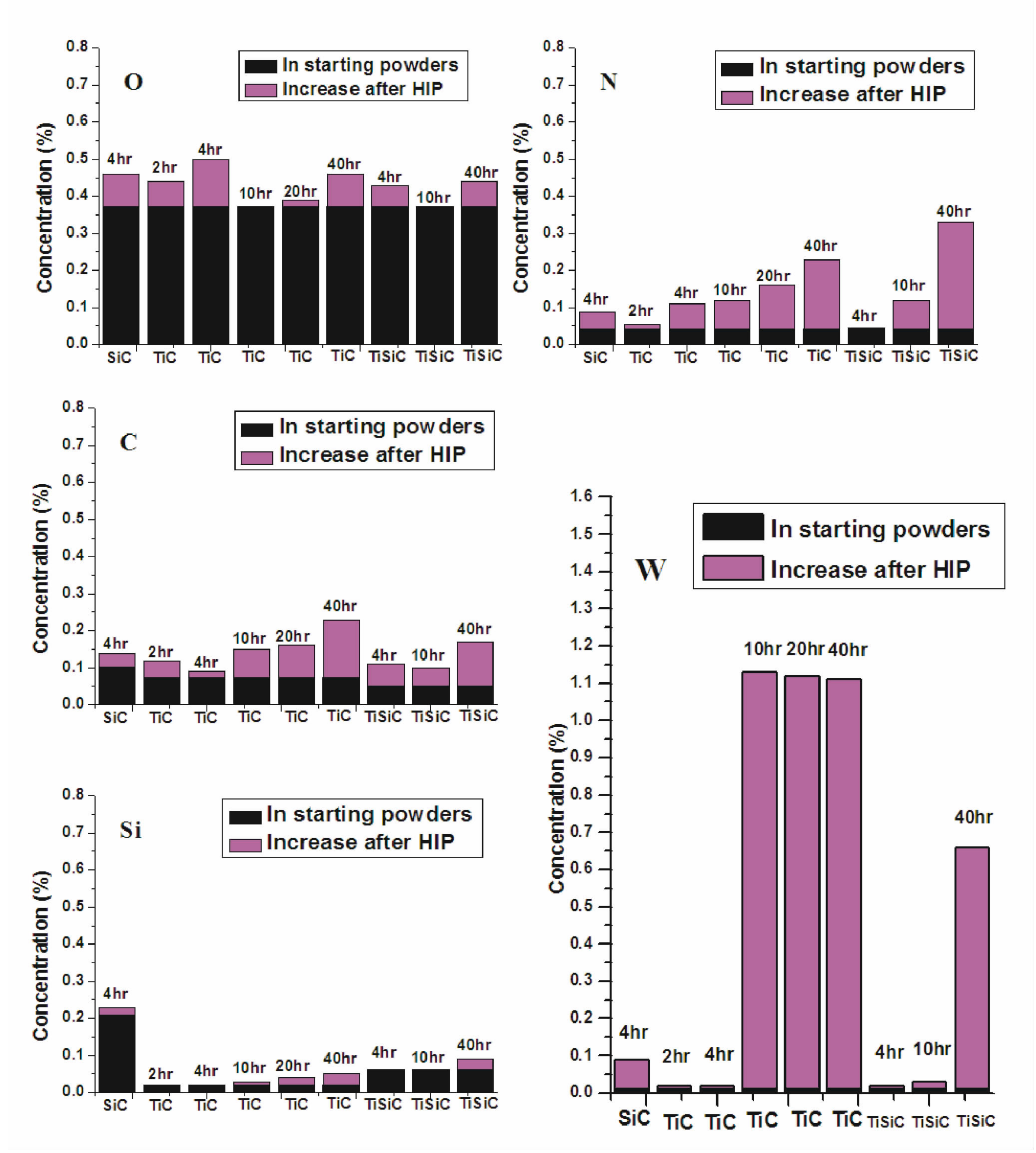

Fig. 6-16 Change in impurity concentrations in the vanadium alloys fabricated with MA process and with WC/Co balls

6.5 Mechanical Properties

6.5.1 Hardness

Hardness data for all mechanically alloyed V-alloys in as-HIPed state and after annealing at 1200℃ for 1hr are plotted in Fig. 6-17. Generally speaking, annealing leads to softening of the alloys, and especially for the alloys with a milling time over 10 hrs. The V-4Cr-4Ti-1.5Y-0.3TiC alloy milled by Si_3N_4 balls for 4 hrs shows very high hardness of up to 332.5Hv in as-HIPed state and 301Hv after annealing. In contrast, the alloys with SiC, TiC and Ti_3SiC_2 additions under same milling condition (340rpm for 4hrs) with WC/Co balls have much lower hardness. The dependence of milling time on hardness shows that, taking V-4Cr-4Ti-1.5Y-0.3TiC system as an example, the hardness increases with increasing milling time, especially from 10hr. Similar situation is fit for all the V-4Cr-4Ti-1.5Y-0.3Ti_3SiC_2 alloys. On the other hand, the Ti_3SiC_2-added alloys always have remarkably lower hardness than the TiC-added alloys under same milling conditions.

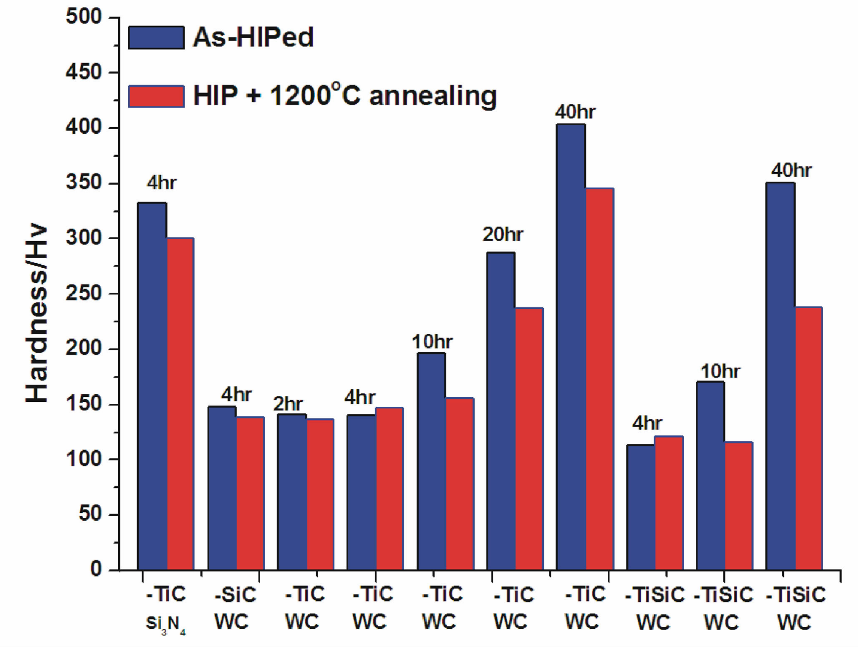

Fig. 6-17 Hardness of all the mechanically alloyed V-alloys in as-HIPed state and after annealing at 1200℃ for 1hr

6.5.2 Tensile Properties

Figure 6-18 and Fig. 6-19 show 750℃ tensile properties of the V-alloys milled for 2-4 hrs in as-HIPed state and after 1200℃ × 1hr annealing. Unlike the trend of hardness, the strength of the TiC, SiC or Ti_3SiC_2 added alloys with 2-4hrs milling by WC/Co and Si_3N_4 balls is increased by the annealing. The V-4Cr-4Ti-1.5Y-0.3TiC alloy milled by Si_3N_4 has the highest yield strength of 301.5MPa, but the poorest uniform elongation of 0.96% after annealing. The tensile curves of WC/Co ball milled alloys exhibit inhomogeneous deformation before the fracture happens, in both as-HIPed state and after annealing. Tensile fracture morphologies of these alloys after being tested at 750℃ are shown in Fig. 6-20. Dimple patterns can be observed, however the dimples are not uniformly distributed, which again indicates that 4hrs is not enough for complete MA of the present V-4Cr-4Ti alloy with Y and carbide additions.

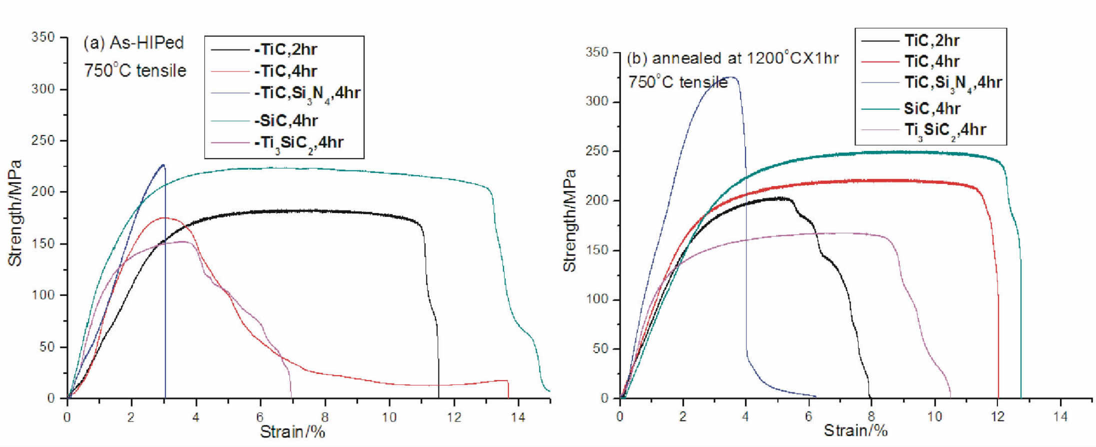

Fig. 6-18 Tensile properties of V-alloys milled for 2-4 hrs in (a) as-HIPed state and (b) after annealing at 1200℃ for1hr

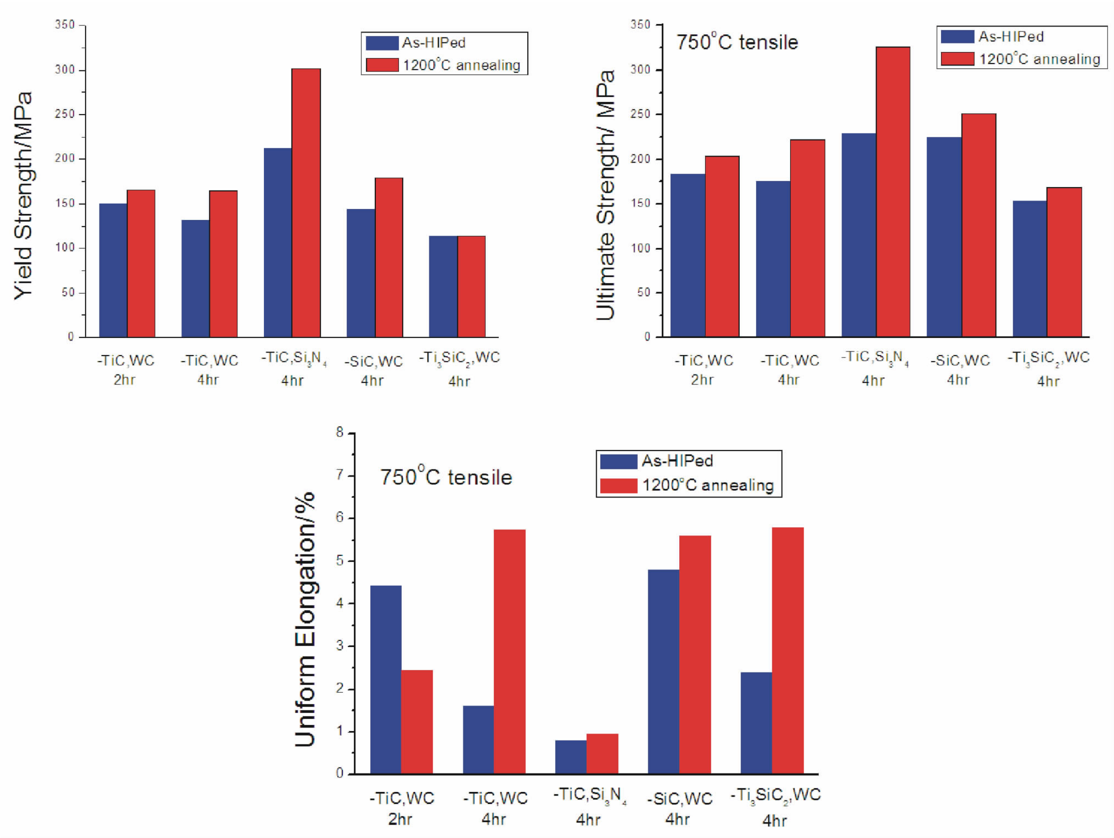

Fig. 6-19 750℃ tensile properties of V-alloys milled for 2-4 hrs in as-HIPed state and after annealing at 1200℃ for 1hr

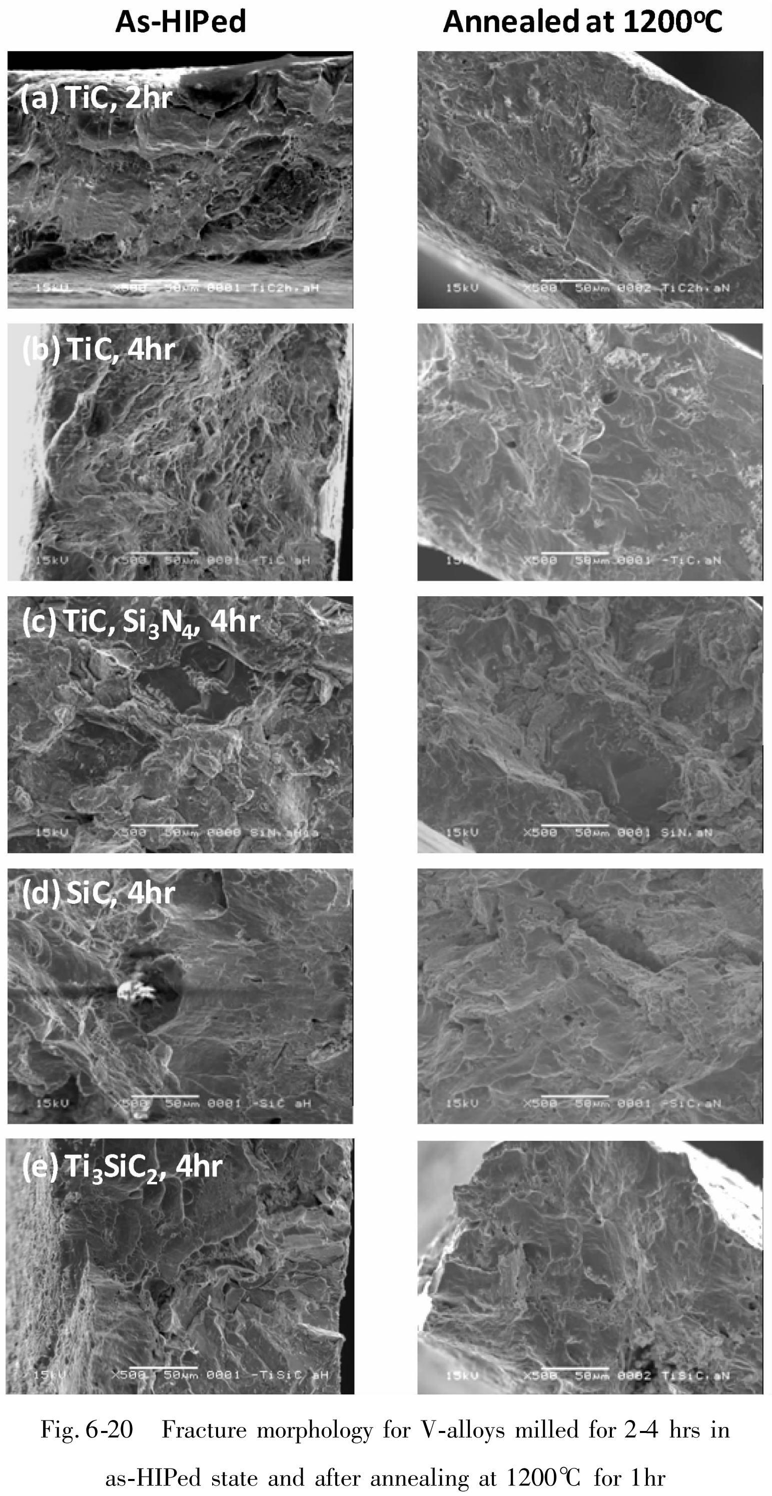

Fig. 6-20　Fracture morphology for V-alloys milled for 2-4 hrs in as-HIPed state and after annealing at 1200℃ for 1hr

Though the annealing at 1200℃ for 1hr has improved high-temperature ductility of the alloys milled with WC/Co balls for 4hrs, alloys under same milling condition but longer time such as 40hrs still appear to be brittle at room temperature (RT). Fig. 6-21 shows RT tensile curve of annealed V-4Cr-4Ti-1.5Y-0.3Ti_3SiC_2 alloy with 40hrs of milling. The yield strength of this alloy is about 530MPa while its uniform elongation is only 1.9%.

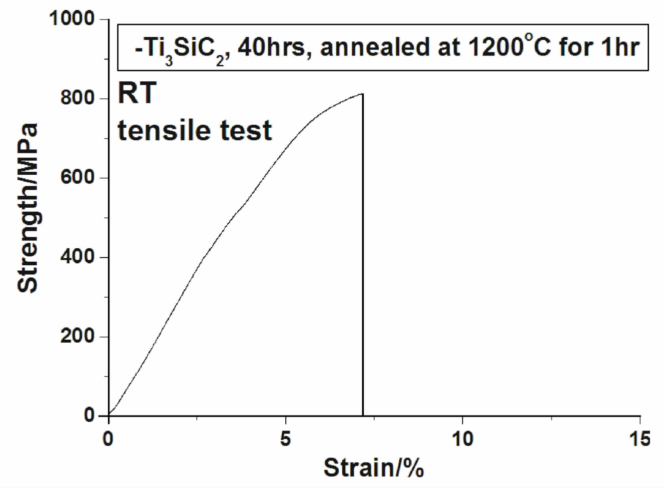

Fig. 6-21 Room temperature tensile curve of V-4Cr-4Ti-1.5Y-0.3Ti_3SiC_2 alloy milled for 40hrs

6.5.3 Creep Properties

Creep tests are performed at 700℃, the creep curves of V-4Cr-4Ti-1.5Y-0.3TiC alloy with 1200℃ ×1hr annealing are used to compare with those of the NIFS-HEAT-2. The comparisons are among "TiC, 40hr", STD and SACWA under 280MPa (Fig. 6-22 (a)) and 100MPa (Fig. 6-22 (b)), because SACWA and STD show the best creep resistance at high and low stress, respectively. The minimum creep rate for every sample under 280MPa is determined by the minimum average creep rate taken in a duration of every 0.2 rupture time. In the case of 100MPa, the curves have periodicity undulation. SACWA has obvious creep stages as shown in Fig. 3-10. Its minimum creep rate is estimated in the same manner as the ones under 280MPa. While for STD and "TiC, 40hr", the minimum creep rates are determined by the average creep rates of the data after 15000min.

Unfortunately, the running condition of the creep machine was not stable during the first 370hrs for "TiC, 40hr" under 100MPa. It seems that the region of minimum creep rate comes after this duration. In addition, the creep test for STD was stopped soon after the third stage creep started. The obvious shift to stage III creep region is not well distinguished in the present study.

The available data of the test at 700℃ under 280MPa show that creep rupture for the annealed "TiC, 40hr" comes much earlier than SACWA, and the minimum creep rate of "TiC, 40hr" is about 30 times higher than SACWA and 7 times higher than STD, respectively. While, for the comparison at 700℃ under 100MPa, "TiC, 40hr" owns a minimum creep rate of about 2.5 times lower than or similar to that of STD, and about 9.5 times lower than that of SACWA. Lifetime of 1% strain at minimum creep rate for the annealed "TiC, 40hr" is 6456hrs at 700℃ under 100MPa.

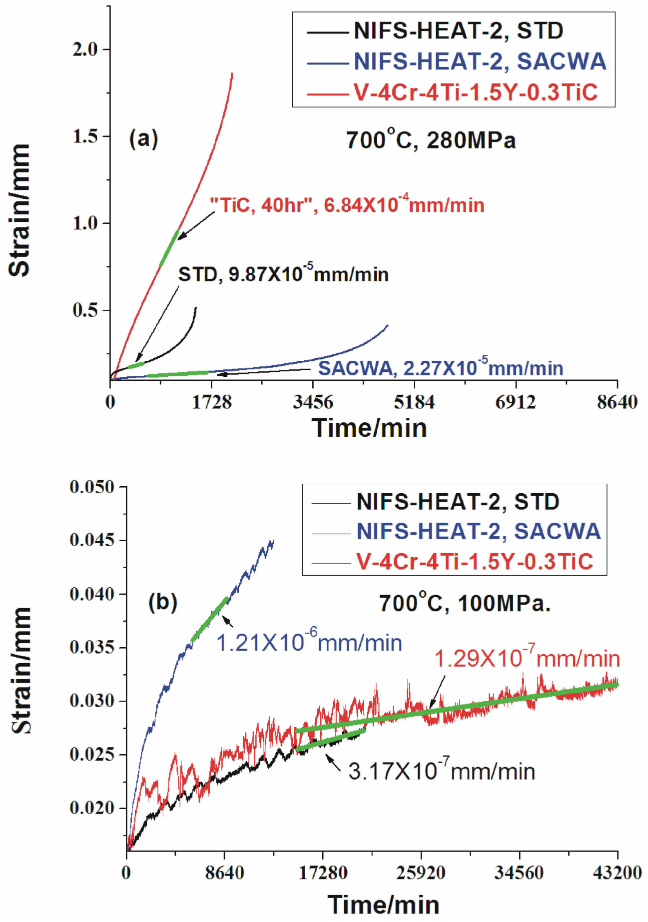

Fig. 6-22 700℃ creep curves of annealed "TiC, 40hr" compared with those of NIFS-HEAT-2 in STD and SACWA states at (a) 280MPa, and (b) 100MPa

6.6 Microstructures

6.6.1 Grains

Typical grain sizes of the V-4Cr-4Ti-1.5Y-0.3TiC alloy milled for 4hrs and 40hrs are different. Where, the alloy milled for 4hrs has larger grain sizes and the other one milled for 40hrs has smaller grain sizes.

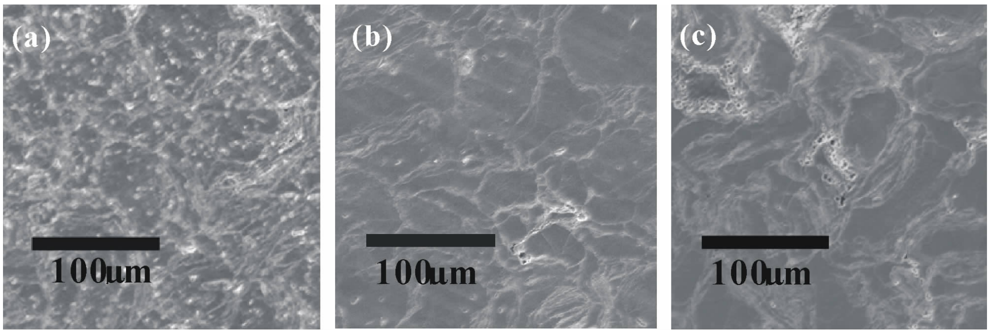

Fig. 6-23 The grain sizes of (a) V-4Cr-4Ti-1.5Y-0.3SiC, (b) V-4Cr-4Ti-1.5Y-0.3Ti_3SiC_2, and (c) V-4Cr-4Ti-1.5Y-0.3TiC alloys with 4hrs milling and annealing at 1200℃ for 1hr

The alloys milled under the same conditions for shorter time have larger grains, which can be observed in SEM. Fig. 6-23 shows the grain sizes of V-4Cr-4Ti-1.5Y-0.3SiC (a), V-4Cr-4Ti-1.5Y-0.3Ti_3SiC_2(b), and V-4Cr-4Ti-1.5Y-0.3TiC (c) alloys with 4hrs milling and after annealing at 1200℃ for 1hr. The non-dissolved Ti is etched by HF in the etching solution, which causes crack-shape area at some grain boundaries. Their average grain sizes are measured to be 47.5μm, 45.5μm and 49μm, respectively.

Figure 6-24 shows the electron diffraction pattern of V-4Cr-4Ti-1.5Y-0.3TiC alloy milled for 40hrs and annealed at 1200℃ in TEM. Numerous grains are detected. For more accurate measurements, only grains which have the same orientation with the one marked with a red circle (See Fig. 6-24 below) are shown with highlighted contrast in Fig. 6-25 (a). The grain size observation for this alloy in as-HIPed state is performed in the same way, and the dark field TEM image for grains is shown in Fig. 6-25 (b). Thus the average grain size of the annealed V-4Cr-4Ti-1.5Y-0.3TiC alloy is measured to be 0.37μm, while that of the as-HIPed V-4Cr-4Ti-1.5Y-0.3TiC alloy is measured to be 0.29μm. Thus, it is clear that the annealing at 1200℃ for 1hr has caused remarkable coarsening of grains in V-4Cr-4Ti-1.5Y-0.3TiC alloy with 40hrs milling.

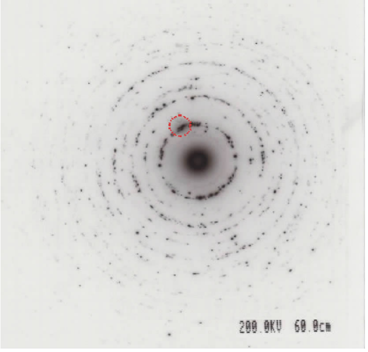

Fig. 6-24 Diffraction pattern of V-4Cr-4Ti-1.5Y-0.3TiC alloy milled for 40hrs and after annealed at 1200℃

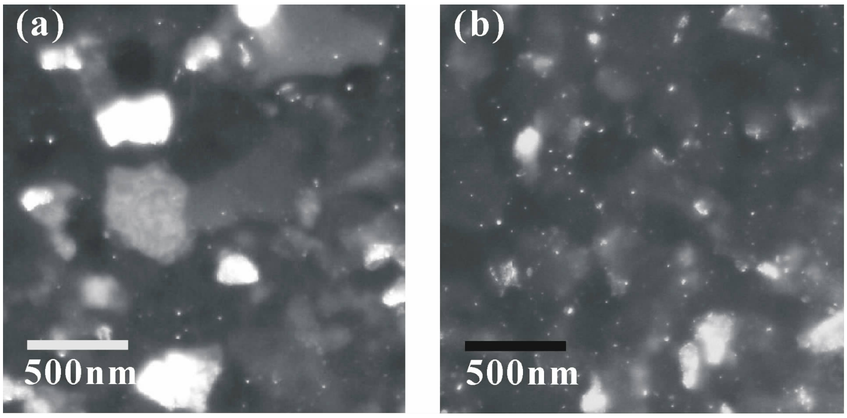

Fig. 6-25 Grain morphology of V-4Cr-4Ti-1.5Y-0.3TiC alloy milled for 40hrs in (a) annealed state and (b) as-HIPed state

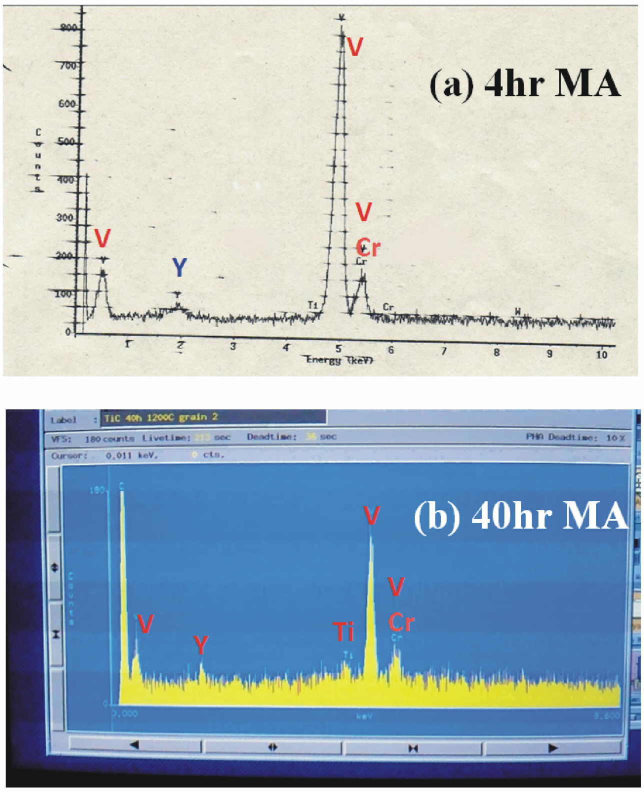

Fig. 6-26 EDX analysis for grains of annealed V-4Cr-4Ti-1.5Y-0.3TiC alloy milled for (a) 4hrs and (b) 40hrs

Figure 6-26 below shows the EDX analysis for the grains of V-4Cr-4Ti-1.5Y-0.3TiC alloy milled for 4hrs and 40hrs. Both of the two samples are HIPed and annealed at 1200℃. In the case of 4hr MA, the grain size is 49μm, V and Y seem to be the main elements in the grain. Since Cr peak is overlapped by V peak, whether or not Cr exists is unclear. The lack of Ti peak indicates that the Ti is far from complete dissolution. While in the case of 40hrs, the grain size is only 0.37μm, though Cr peak is still overlapped, Y and Ti peaks are clearly shown.

6.6.2 Nanoparticles

Figure 6-27 shows TEM images of the nanoparticles in (a) V-4Cr-4Ti-1.5Y-0.3SiC, (b) V-4Cr-4Ti-1.5Y-0.3Ti_3SiC_2, (c) V-4Cr-4Ti-1.5Y-0.3TiC alloys with 4hrs milling and being annealed at 1200℃ for 1hr. V-4Cr-4Ti-1.5Y-0.3TiC alloy with 4hrs milling in as-HIPed state (d) is also shown. The size distributions and volume number densities of the nanoparticles are plotted below the TEM images. The main sizes of the nanoparticles in these three alloys are all within 5-10nm range in the present TEM observation which has an accuracy of about 5nm. This study consider 10nm to be the reference scale for classifying small size and medium size. 30nm, as the beam spot size, is considered to be the reference scale for classifying medium size and large size.

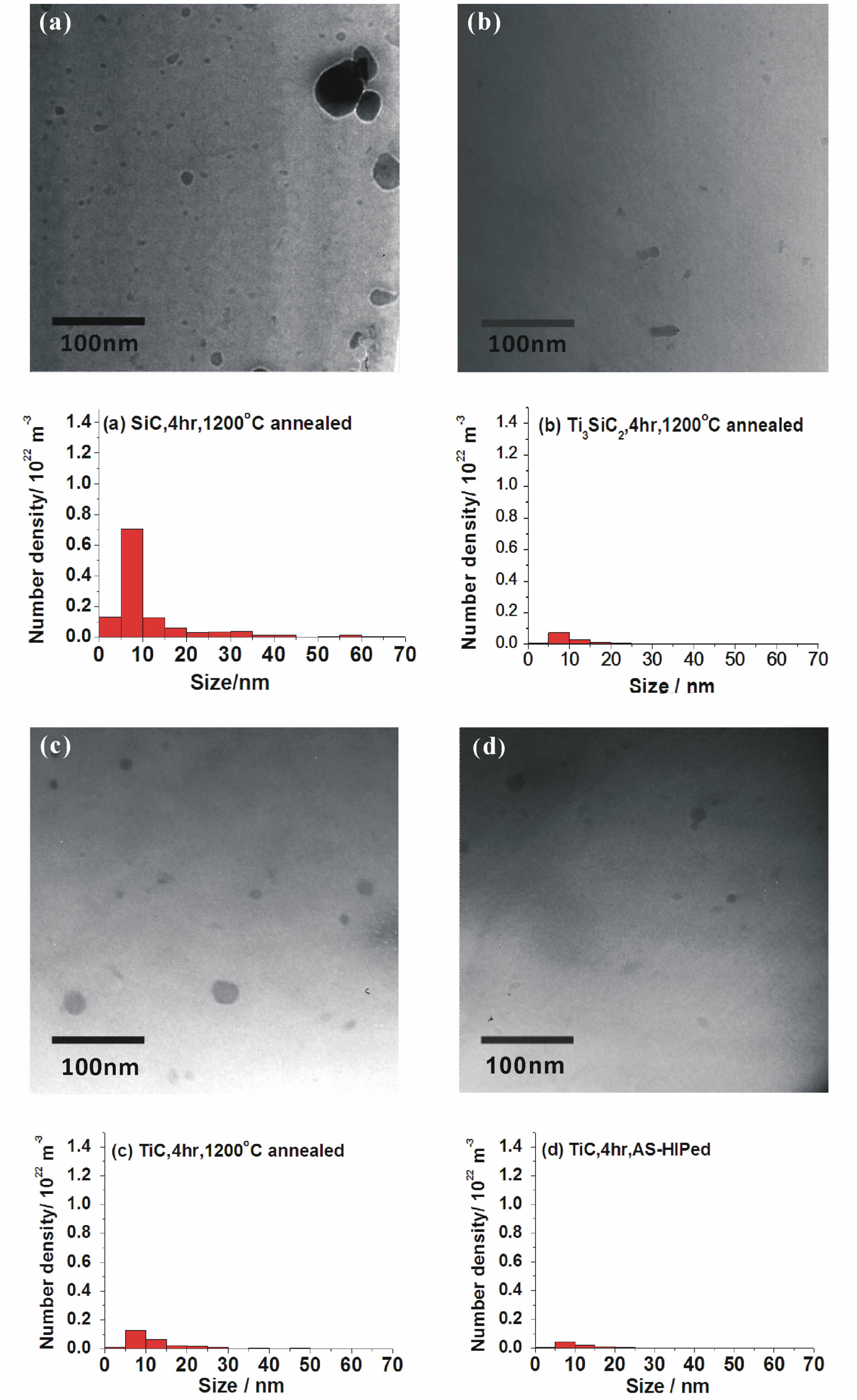

Fig. 6-27 TEM images and size distributions of nanoparticles in 4hr-milled

(a) V-4Cr-4Ti-1.5Y-0.3SiC with annealing, (b) V-4Cr-4Ti-1.5Y-0.3Ti_3SiC_2 with annealing,

(c) V-4Cr-4Ti-1.5Y-0.3TiC with annealing and (d) V-4Cr-4Ti-1.5Y-0.3TiC in as-HIPed state

For a quantitative comparison, the annealed V-4Cr-4Ti-1.5Y-0.3SiC alloy has small nanopartilces with average size of 6.1nm and a large number density of $9.74\times10^{21}/\text{m}^3$; the annealed V-4Cr-4Ti-1.5Y-0.3Ti_3SiC_2 alloy has small nanopartilces with average size of 7.6nm and a small number density of $1.03\times10^{21}/\text{m}^3$; the annealed V-4Cr-4Ti-1.5Y-0.3TiC alloy has small nanopartilces with average size of 8.4nm and a small number density of $2.66\times10^{21}/\text{m}^3$; while, the as-HIPed V-4Cr-4Ti-1.5Y-0.3TiC alloy has small nanopartilces with average size of 9.2nm and a small number density of $9.11\times10^{20}/\text{m}^3$. Among them, few nanoparticles of medium size are also observed.

In order to indicate the evolution of nanoparticles caused by annealing, larger number density of nanoparticles are favored. Morphology and distribution of nanoparticles in V-4Cr-4Ti-1.5Y-0.3TiC alloy with 40hrs milling was analyzed in as-HIPed state and annealed state, as shown in Fig. 6-28. The number density of this alloy is high, which is $1.73\times10^{22}/\text{m}^3$ for the as-HIPed state, and up to $2.92\times10^{22}/\text{m}^3$ for the annealed state (some small ones are invisible in the present contrast condition). This shows the new formation of nanoparticles was caused by annealing. There is coexistence of small and medium size nanoparticles. However, medium size nanoparticles (10-30nm) largely reduced after the annealing, and small size nanoparticles with size smaller than 10nm and especially smaller than 5nm are produced in high number density.

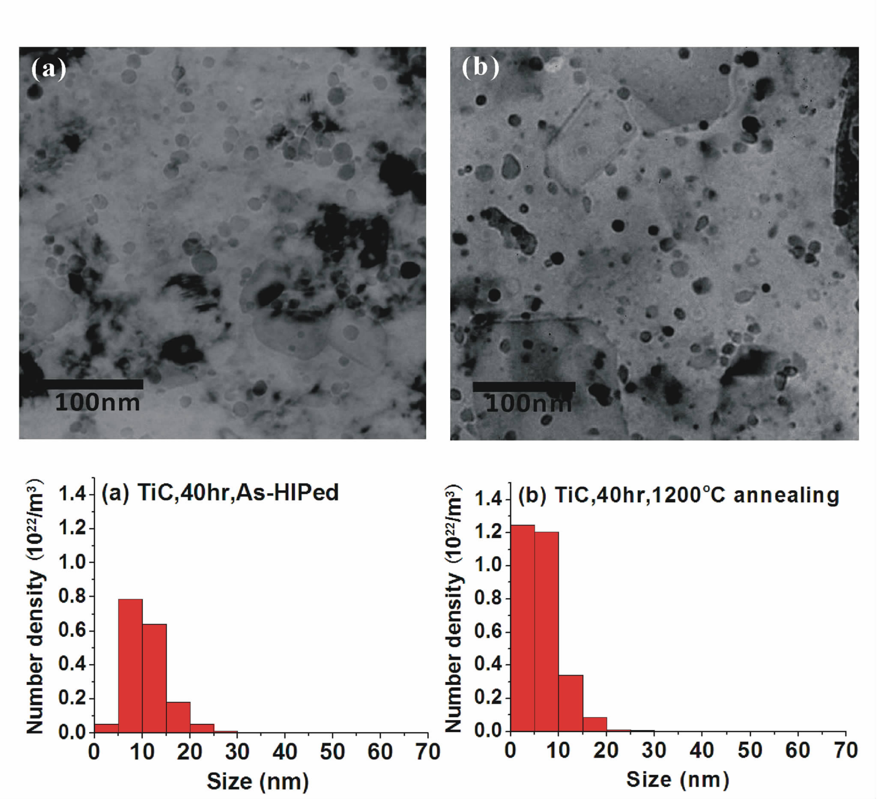

Fig. 6-28 TEM images for nanoparticles of V-4Cr-4Ti-1.5Y-0.3TiC alloy in (a) as-HIPed state and (b) annealed state

The EDX analysis for nanoparticle species has been applied on two particles of around 100nm (large size) and around 20nm (medium size) in V-4Cr-4Ti-1.5Y-0.3TiC alloy after annealing, as shown in Fig. 6-29. Result shows that the large nanoparticles are Ti-rich, with small amount of Y being detected, While, the medium size nanoparticles are rich in Y. The V peaks are considered to be from the surrounding matrix, as the electron beam spot is 30nm, which is larger than the particle detected, thus information of V is included in this EDX analysis. According to the XRD analysis as shown in Fig. 6-15, large nanoparticles are considered to be TiN, and the medium nanoparticles detected are considered to be Y_2O_3.

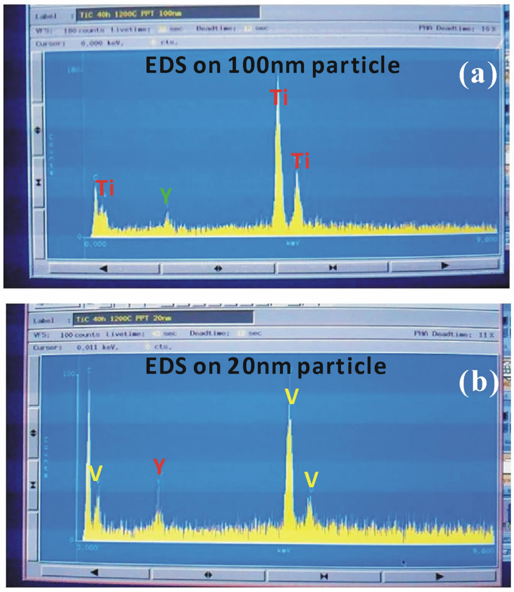

Fig. 6-29 EDX analysis for nanoparticles with large size (100nm) (a) and small size (20nm) (b) in the annealed V-4Cr-4Ti-1.5Y-0.3TiC alloy

Further XRD analysis in Fig. 6-30 below shows that there is TiC peak newly appeared after annealing, compared with the situation in the as-HIPed alloys adding either TiC or Ti_3SiC_2. It is unclear whether the TiC peak of "TiC, 40hrs" is from its starting powders or be produced by the annealing. However, TiC peak in the annealed "Ti_3SiC_2, 4hrs" is generally considered to be formed during the annealing process, as shown in Fig. 6-30 (b).

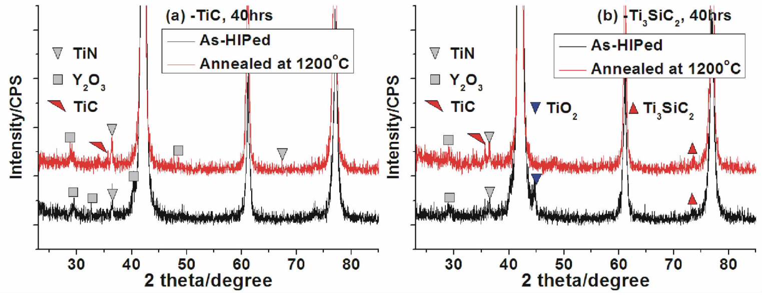

Fig. 6-30 Phase evolution of (a) TiC-added and (b) Ti_3SiC_2-added V-4Cr-4Ti alloys with Y addition after 1200℃ annealing

6.7 Discussions

6.7.1 Mechanical Alloying Process

For application of every structural material, the homogeneity of its chemical compositions is one of the most important requirements, because it determines the homogeneity of microstructures and thus mechanical properties of the material. Accordingly, the dissolution of alloying elements into alloy matrix and the uniform solid solution are key factors that contribute to homogeneity of the compositions, for either melting and or MA. However, currently, there is no theory that can directly predict the dissolution behavior in a MA process [148]. The elemental distributions observed by SEM-EDX and the peak shift detected by XRD analysis can roughly indicate the dissolution behavior of the alloying elements. From the line scanning analysis for the powder samples, we know that the distribution of alloying element during the MA process from 0hr to 10hrs (See Fig. 6-11) becomes more uniform with the increasing MA time, which can be found from the change of element distribution. In this case, Y distribution becomes almost uniform within 2hrs, while for Cr and Ti under similar dissolution condition, it takes about 4hrs and more than 10hrs, respectively. It seems that the collision-induced dissolution rate of Y is higher than that of Cr, and the collision-induced dissolution rate of Cr is higher than that of Ti in the present study. The dissolution behavior of these three elements also agrees with the lattice parameter change in V matrix as characterized by XRD analysis. Atoms larger than V, such as Y and Ti, expand the V lattice, on the other hand, smaller atoms such as Cr causes shrinkage of the lattice. The data of atomic radius of V, Cr, Ti and Y, and their effects on V lattice are shown in Table 6-8 below.

Table 6-8 Atomic radius of V, Cr, Ti and Y atoms and their effects on V lattice

Element	Atomic radius (nm)	Effects on V lattice
Cr	0.125	Shrinkage
V	0.132	—
Ti	0.143	Expansion
Y	0.181	Expansion

Line scanning and XRD analysis show that Y solutes induce lattice expansion of V matrix during the 2hr-MA process, and show most prominently at 1hr. Then, lattice shrinkage caused by Cr dissolution overwhelms the expansion caused by Y atoms, and this shrinkage appears obviously at the end of the 2hrs period when Y dissolution almost ends. Similarly, when the dissolution of Cr into V matrix almost ends at the end of the 4hr, Ti remains as the main element which expands the V lattice monotonously till more than 10hrs. However, the line scan in Fig. 6-11 above was performed on powder samples, the dissolution information is very local, thus the an area scan performed on HIPed bulk samples (See Fig. 6-12) appears to be more convincing to indicate the story. Then, of course it is reasonable that the time required for complete dissolution of each element differs from that in line scanning. However, the sequence of dissolution does not change. It is still that Y dissolves (in 2hrs) faster than Cr (in 20hrs), and Cr dissolves (in 20hrs) faster than Ti (in 40hrs) into the V matrix under the present MA condition. A possible dissolution history of Y, Cr and Ti is illustrated in following Fig. 6-31, where the SEM-EDX is just for area scanning.

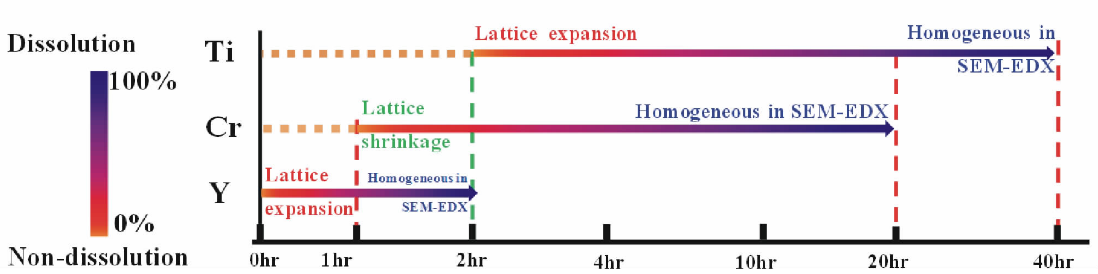

Fig. 6-31 Possible dissolution history of Ti, Cr and Y into V matrix

According to the experimental data, the time required for a complete MA process of the present V-4Cr-4Ti alloys with Y and carbide additions depends on the dissolution of Ti. As in this study (with WC/Co balls of 5mm in diameter; volume ratio of ball + material to vessel to be 1:4; ball to material weight ratio to be 5:1, and rotation speed of 340rpm), a complete MA process needs 40hrs approximately. Therefore, after HIPing, the alloys with 2-4hrs milling are incompletely alloyed powders with simple bonding.

Assuming a certain percent of kinetic energy of milling balls has been converted to collision energy, the collision energy can be described with following equation (6-4):

$$E = k'' \cdot mv^2 \tag{6-4}$$

Where k'' is a constant relating to the milling system; m is the weight of each milling ball (0.20g for a Si_3N_4 ball, and 1.0g for a WC/Co ball); v is the rotation speed (650rpm for Si_3N_4 milling, and 340rpm for WC/Co milling). Accordingly, the energy of each collision by a Si_3N_4 ball is $8.57 \times 10^4 (k'' \cdot g \cdot rpm^2)$, which is less than that by a WC/Co ball, of $1.11 \times 10^5 (k'' \cdot g \cdot rpm^2)$. Moreover, the weight loss of Si_3N_4 ball causes a reduce in the collision energy, and the mixed Si_3N_4 powders may further exhaust the collision energy. So it is reasonable to consider that the MA with Si_3N_4 balls (e.g. "TiC, Si_3N_4, 4hr") is even more incomplete compared with the case of WC/Co balls with the same milling parameters. Thus WC/Co balls are more favored than Si_3N_4 balls in MA of V-4Cr-4Ti alloy with Y and carbide additions, and worth to be used in long time MA for complete alloying.

The reason why different metals dissolve into V matrix in different rates may be that these elements have different diffusivity. After all, mechanical alloying is a solid-state processing method and it is only due to solid-state diffusion that alloying will occur. Of course, diffusion occurs faster during mechanical alloying because of several reasons. However, the most important of them would be the presence of a high density of crystal defects such as dislocations and grain boundaries [148].

6.7.2 Dissolution of Nonmetallic Particles

Si_3N_4 is the only possible source of Si in MA process and during HIPing for the "-TiC, Si_3N_4, 4hr" alloy. Because Si_3N_4 was easily ground into the alloy powders, parts of the resulted Si_3N_4 powders are thought to have dissolved as Si and N impurities into the V matrix. In addition, increase of O (see Table 6-7) in this alloy is remarkable. Thus, the increase in Si, N and O levels can partly account for the hardening of the "-TiC, Si_3N_4, 4hr" alloy through the formation of precipitates, interstitial atoms, or matrix of a possible composite material.

As to the dissolution effect of dispersion particles, hardening caused by solid solution can also be identified in Fig. 6-15. Gibbs free energy for the formation of TiN is about -309.2kJ/mol, which is less than that of TiC, of -180.5kJ/mol. Therefore, the formation of TiN is easier than that of TiC. Based on this, TiN may form and coarsen in MA, HIPing and the following annealing as shown in Fig. 6-15 (a). On the other hand, the chemical analysis result in Fig. 6-16 shows that the "-Ti_3SiC_2, 4hr" alloy has lower Si concentration than the expected average value for the whole sample. Refer to the XRD spectrums of this alloy in Fig. 6-15 (b), it can be found that Ti_3SiC_2 peaks have been existing for 40 hrs all along the MA process. It seems that the Ti_3SiC_2 might have poor dissolution, and this poor solid-solution may have caused low hardness in the as-HIPed "-Ti_3SiC_2, 4hr" alloy.

After HIPing, the post annealing at 1200℃ for 1hr seems to have strengthened the vanadium alloys fabricated via MA, as shown in Fig. 6-18 and Fig. 6-19, where the strength of these alloys have been increased by the annealing. This can be explained as more efficient precipitation hardening. The change of nanoparticle number density before and after annealing at 1200℃ results in an estimated hardening of 11Hv for "TiC, 4hr" according to equation (6-3), which shows that TiC may be easier than Ti_3SiC_2 to dissolve and then form again.

The variation of grain sizes for the alloys with 4hr MA is considered not to result in remarkable change in hardness, because the size of the indentation is typically 50-60 μm in the hardness test. However, annealing at 1200℃ for 1hr has increased the number density of nanoparticles. Therefore, more suitable annealing is expected to obtain larger number density of nanoparticles and benefits obvious hardening for the alloys.

Based on the above discussion, when MA time is short, hardness change caused by precipitation condition and grain size seems negligible for WC/Co-milled alloys. Poor dissolution of Ti_3SiC_2 in "-Ti_3SiC_2, WC, 4hr" may account for lower hardness of this alloy. With this consideration, MA with longer time or high collision intensity is expected to dissolve the Ti_3SiC_2 particles more completely.

6.7.3 Mechanical alloying strengthening of V-4Cr-4Ti alloys with Y and carbide additions

MA strengthening mainly comprises grain-size refining and nanoparticle dispersion strengthening. In some cases, if the starting material contains high concentration of interstitial impurities, a considerable solid solution hardening with these interstitial impurities is also expected.

It is clear that after 10hrs milling, the resulted alloys have apparent increase in hardness, for both TiC and Ti_3SiC_2 added alloys, as shown in Fig. 6-17. The average grain size of the 4hrs milled alloys is measured to be 45-50μm in as-HIPed state and after annealing. While the average grain size of the V-4Cr-4Ti-1.5Y-0.3TiC alloy with 40hrs milling is 0.29μm in as-HIPed state and 0.37μm after annealing. Accordingly, the change in hardness can be estimated with the Hall-Petch equation (6-2). Since the Hall-Petch slope k' is determined by the material matrix, k' of materials with similar compositions can be taken as a reference data for rough estimation. According to previous study on MA for vanadium alloys[100, 102], as shown in Fig. 6-32, the average k' value is estimated to be 105 (Hv · $\mu m^{-1/2}$).

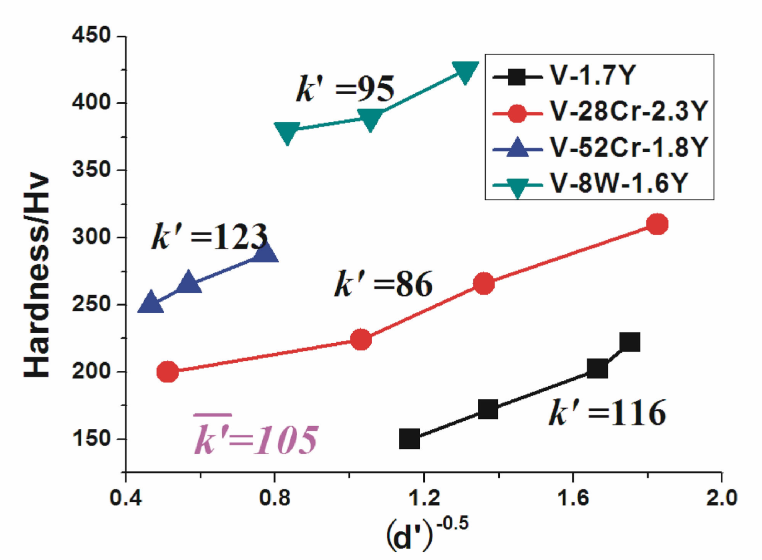

Fig. 6-32 Estimation of k' value in Hall-Petch equation for hardening calculation

Hardening caused by nanoparticles can be calculated with equation (4-5). Table 6-9 below shows the hardening caused by grain size, nanoparticles, solid solution and so on for each alloy fabricated via MA.

The contribution to hardening by grain size, nanoparticles, solid solution and so on is plotted in Fig. 6-33 below. Pure vanadium, NIFS-HEAT-2 in initial STD state and after Li exposure at 650℃ for about 250hrs are used as reference materials to show the strengthening induced by MA. Contribution to hardening from Cr together with Ti is estimated by comparing the hardness of initial pure V with that of STD. In the case of incomplete MA, solid solution hardening caused by Cr and Ti is unclear, therefore it is not shown in this figure.

Table 6-9　Contributions of all possible hardening mechanisms to the hardening of some V-4Cr-4Ti alloys with Y and carbide additions.

Hardening source		**Ti_3SiC_2, 4hr, Annealed**	**SiC, 4hr, Annealed**	**TiC, 4hr, Annealed**	**TiC, 4hr, As-HIPed**	**TiC, 40hr, Annealed**	**TiC, 40hr, As-HIPed**
Hardness measured		121	138	147	140	346	404
Estimation from Nanoparticles	Size (nm)	7.9	6.1	8.4	9.2	4.9	9.7
	Density /m^3	1.03×10^{21}	9.74×10^{21}	2.66×10^{21}	9.11×10^{20}	2.92×10^{22}	1.73×10^{22}
	Hardening (Hv)	10	26	16	10	40	43
Estimation from Grain	Size (μm)	45.5	47.5	49	45	0.37	0.29
	Hardening (Hv)	15	15	15	15.5	173	195
Cr and Ti solid solution						55	55
Basic hardness		53.5	53.5	53.5	53.5	53.5	53.5
Other		42.5	43.5	62.5	61	24.5	57.5

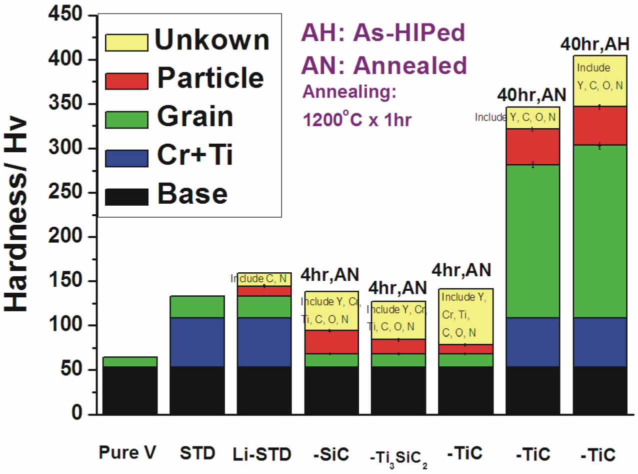

Fig. 6-33　Contribution of all possible hardening mechanisms to the hardening of V-4Cr-4Ti alloys with Y and carbide additions, pure vanadium and NIFS-HEAT-2

The as-HIPed V-4Cr-4Ti-1.5Y-0.3TiC alloy with 40hrs MA has a calculated hardening of 195Hv due to small grain size, while in the case of 4hrs, the hardening is around 15Hv. Therefore, most increase in hardness of V-4Cr-4Ti-1.5Y-0.3TiC alloys milled for 10hrs and 20hrs is also expected to be caused by the gradually refined grains with increasing MA time. For V-4Cr-4Ti-1.5Y-0.3Ti_3SiC_2 alloys, situation is considered to be similar. In contrast, particle dispersion strengthening is smaller than the strengthening contributed by grain size refining. For completely alloyed materials (Pure V, STD, Li-STD, "TiC, 40hr" in as-HIPed state and annealed state), hardening contribution from the solid solution of C, N, O interstitial impurities and Y substitutional atoms are included in the unknown part. While for the alloys being milled for 4hrs, all solid solution of Y, Cr, Ti beside of C, N and O are also included in the unknown parts.

It is worth noting that for the materials with 40hrs MA, contribution to hardening from the grain size refining is much larger than that from nanoparticle dispersion strengthening. Thus a more suitable annealing is expected to produce high number density of nanoparticles and coarsened grains for a tradeoff between grain sizes coarsening and nanoparticle dispersion strengthening, and improve creep resistance. Moreover, the simple estimation of the hardening is just for roughly showing the contribution to hardening.

As thermal stability is a key property to determine more suitable annealing conditions, the classification of nanoparticle species is necessary. Fig. 6-28 shows the nanoparticles with medium size of 10-30nm largely decreases because of coarsening, and abundant new nanoparticles with size as small as about 5nm are produced in annealing. Thus the annealing seems to be accompanied with the shift of size distribution in which more small-size nanoparticles are produced.

It is considered that MA brought the coexistence of medium and large Ti-rich particles (almost TiN) along with the coexistence of small and medium size Y-rich particles (almost Y_2O_3). Then, TiN nanoparticles almost all dissolved into the V matrix during the annealing at 1200℃, while new Y_2O_3 nanoparticles formed. So, finally, the nanoparticles left to be found are almost Y_2O_3 of small and medium sizes. Considering that the coarsening of Y_2O_3 nanoparticles can occur in annealing, it is reasonable to consider that the medium size nanoparticles analyzed with EDX in Fig. 6-29 (b) are coarsened Y_2O_3, according to the evolution of size distribution as shown in Fig. 6-28.

In consequence, Y-rich nanoparticles are more thermally stable than Ti-rich nanoparticles. So, to control the formation of Y_2O_3 nanoparticles is expected to be a core concern in the optimization of MA strengthening for V-4Cr-4Ti alloys in future research.

6.7.4 Creep Mechanism

Though mechanical alloying can strengthen V-4Cr-4Ti alloy with Y and carbide additions from the aspect of hardness and tensile strength, creep resistance is only improved at low stress level in the present study. Ref [109] showed that V-1.4Y-7W-9Mo-0.7TiC alloy has improved creep resistance relative to STD state NIFS-HEAT-2 in at 800℃ under high stress of 250MPa, and the improvement increases with increasing annealing temperature from 1200℃ to 1500℃. However, this improvement may come from two factors: (1) V-1.4Y-7W-9Mo-0.7TiC contains different alloying element from STD (NIFS-HEAT-2); (2) the fabrication methods used such as MA and melting are different. It is well known that W and Mo have high melting points (2617℃ and 3410℃, respectively) than V (1890℃) has. Moreover, the diffusion rate of Mo ($6.2\times10^{-22}m^2/s$) in V matrix is slower than that of Cr and Ti ($2.8\times10^{-21}m^2/s$ and $4.9\times10^{-21}m^2/s$, respectively), and is also slower than the self-diffusion rate of V ($5.4\times10^{-18}m^2/s$) [143, 144]. The slower diffusion rate of 9% Mo can decrease the dislocation climbing rate which is based on atom diffusion in V matrix remarkably. The diffusion data of W into V are not available at present. However, it is considered that W diffuses even lower than Mo according to the data in Ref [143]. Thus the dislocation climbing creep is reduced by the 7% W and 9% Mo rather than by the 4% Cr and 4% Ti. So, the strengthening mechanism may not be clarified only based on the comparison between V-1.4Y-7W-9Mo-0.7TiC and NIFS-HEAT-2.

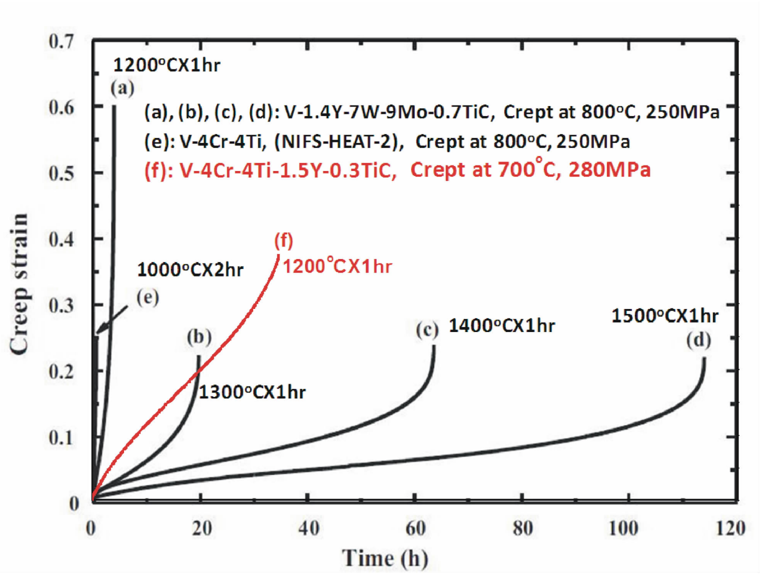

Fig. 6-34 Comparison of creep curves for "TiC, 40hr" tested at 700℃ under 280MPa with V-1.4Y-7W-9Mo-0.7TiC and NIFS-HEAT-2 tested at 800℃ under 250MPa [109]

If compare alloys with same MA method, the V-1.4Y-7W-9Mo-0.7TiC alloy with annealing at temperature above 1300℃ and tested at 800℃ has higher creep resistance than V-4Cr-4Ti-1.5Y-0.3TiC tested at 700℃, as shown in Fig. 6-34. However, V-1.4Y-7W-9Mo-0.7TiC has higher TiC content rather than V-4Cr-4Ti-1.5Y-0.3TiC has, and the W and Mo in V-1.4Y-7W-9Mo-0.7TiC also has slower diffusion rate than that of Cr and Ti in V-4Cr-4Ti-1.5Y-0.3TiC. Moreover, the grain size of V-1.4Y-7W-9Mo-0.7TiC annealed at 1200℃ is 0.58μm, while the grain size of V-4Cr-4Ti-1.5Y-0.3TiC annealed at 1200℃ is only 0.37μm. Among the above possible reasons, the reason of grain size is the most important one.

An important message from Ref [109] is that the coarsening of grain size contributes mainly to the further improvement of creep resistance for the V-1.4Y-7W-9Mo-0.7TiC alloy at

250MPa. This trend is usually common for all mechanically alloyed metals, because larger grains reduce grain boundary deformation.

According to Ref [143, 144], for almost all solid metals (unfortunately, data for vanadium are not sufficient.), the activation energy of self-diffusion at grain-boundary is much lower than that of the self-diffusion in matrix, and the diffusion rate of grain boundary is over 5 orders higher than that of the matrix. So, when grain sizes are too small, creep deformation will largely be dominated by grain-boundary sliding. That may be the reason why "TiC, 40hr" has higher creep rate than STD and SACWA at 280MPa, where, STD has dislocation-glide creep mechanism and SACWA has dislocation climbing creep mechanism.

Under lower stress level such as 100MPa, V-4Cr-4Ti-1.5Y-0.3TiC has improved creep resistance than STD and SACWA has. This improvement probably comes from the existing of a high number density of nanoparticles in the alloy, because 100MPa locates near the dislocation creep region according to the deformation map for vanadium alloys [149].

6.7.5 Position of Present MA Work for Vanadium Alloys and Further Proposal

Fig. 6-35 shows the current achievement of V-4Cr-4Ti-1.5Y-0.3TiC alloy ("TiC, 40hr") relative to other vanadium alloys and the design criteria for vanadium alloys in fusion reactors. The reference materials are NIFS-HEAT-2 in STD state, mechanically alloyed V-1.6Y-8W-0.8TiC alloy [102] and mechanically alloyed V-1.4Y-7W-9Mo-0.7TiC alloy [102]. Actually, the V-1.6Y-8W-0.8TiC alloy and V-1.4Y-7W-9Mo-0.7TiC alloy are the same material, but designated with different names in different research groups. V-1.4Y-7W-9Mo-0.7TiC was designated because V-1.6Y-8W-0.8TiC gained Mo from TZM (Mo-0.5% Ti-0.1% Zr) vessels and balls [102]. The V-1.6Y-8W-0.8TiC alloy was annealed at 1400℃ for 1hr with grain size of 1.45μm, and the V-1.4Y-7W-9Mo-0.7TiC alloy was annealed at

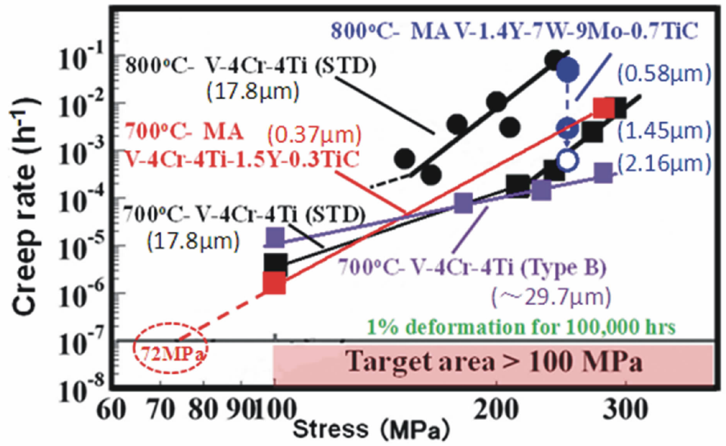

Fig. 6-35 Creep rate of mechanically alloyed V-4Cr-4Ti-1.5Y-0.3TiC (0.37μm) with V-1.6Y-8W-0.8TiC (1.45μm) [102], V-1.4Y-7W-9Mo-0.7TiC (0.58μm and 2.16μm) [109] and V-4Cr-4Ti alloy (NIFS-HEAT-2 in STD state, 17.8μm) tested at 700-800℃ relative to the design criteria

1500℃ for 1hr with grain size of 2.16μm. They have the highest creep resistance in the relevant articles (See Ref. [102] and Ref. [109]), respectively. The solid lines in the figure are for measured results, and the dashed lines are for results or expected targets.

Actually, real trend may not go as the dashed line shows, because creep mechanism may change according to stress level. Only "TiC, 40hr" alloy in the present study and NIFS-HEAT-2 (in STD and SACWA states) have creep data at 100MPa.

According to the comparison as shown in the above picture, "TiC, 40hr" seems to have the poorest creep resistance at 280MPa, because STD has lower creep rate than "TiC, 40hr" at the same temperature of 700℃. V-1.6Y-8W-0.8TiC and V-1.4Y-7W-9Mo-0.7TiC can have much lower creep rate than "TiC, 40hr" at even higher temperature such as 800℃ when its grains grow to larger size. However, this may partly be due to lower concentration of alloying elements and especially due to the smaller grain size in "TiC, 40hr". Take V-1.4Y-7W-9Mo-0.7TiC for example, its creep rate at 800℃ under 250MPa of the 1500℃ annealed sample (2.16μm) is 67 times lower than that of the1200℃ annealed sample (0.58μm). If same decrease in creep rate happens to "TiC, 40hr" under 100MPa when the alloy is annealed at 1500℃, the creep rate of "TiC, 40hr" will exceed the design criteria requirement for Li/V blanket which is 1% deformation for 100,000hrs under 100MPa.

Currently, it is not clear how much change will "TiC, 40hr" have in the creep rate when be annealed at 1500℃, as the grain size and precipitation conditions would both be changed. However, at least the effect of grain size on creep rate is clear now. According to the previous study on creep behaviors of mechanically alloyed vanadium alloys [109], the dependence of steady-state creep rate on grain sizes is clear, as shown in Fig. 6-36. The slope of the logarithmic curve on the chart for steady creep rate with reciprocal grain size makes it possible to estimate the creep rate of vanadium alloy with a certain grain size. The dependence of creep rate on grain size has often been reported for the fine or refined grain structures in which grain boundary sliding dominates the deformation [150].

Considering that the grain size of the crept "TiC, 40hr" is 0.37μm, a growth of grain size over 1μm is expected to meet the requirement of blanket design (1% deformation for 100,000hrs running at 700℃ under 100MPa at its minimum creep rate). However, this estimation is based on two assumptions. One is that for "TiC, 40hr", there is still dependence of creep rate on grain size as shown in Fig. 6-36. The other assumption is that the "TiC, 40hr" with coarsened grains has the same trend in creep rate as the one marked with red blocks in Fig. 6-35 above.

Of course, experimental data are needed to show the real trend for "TiC, 40hrs", because the improvement of creep resistance by grain size growth is based on grain boundary sliding mechanism at high stress level. Under 100MPa, the improvement of creep resistance due to grain growth may be different from the above estimation because the creep may not only be dominated by grain boundary sliding. Nevertheless, the above estimation directs an optimistic prospect for the strengthening of "TiC, 40hr" by increasing its grain size. On the other hand, based on some previous report [151], grain sizes have a limiting value which is effective to change the creep resistance of a metal or alloy. This is common for almost all metals and alloys. As to nanoparticles, in Fig. 6-28(b), more and smaller Y_2O_3 nanoparticles are formed after annealing at 1200℃ due to their high thermal stability. With more suitable annealing, nanoparticles such as Y_2O_3, possible TiC and other carbide nanoparticles are expected to be formed with larger number density and enhances the dispersion strengthening.

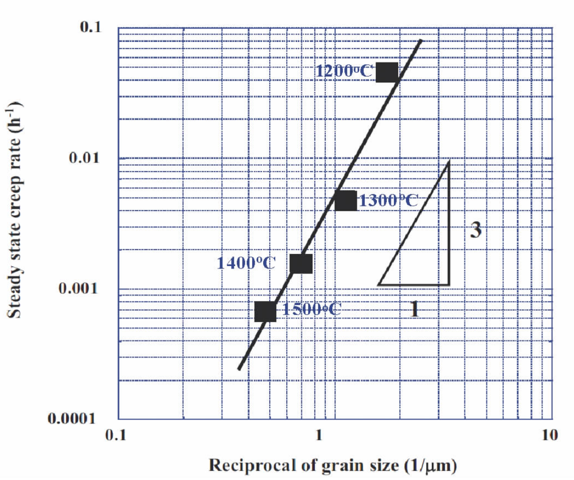

Fig. 6-36 Dependence of steady state creep rate on the reciprocal of grain size for V-1.4Y-7W-9Mo-0.7TiC tested at 800℃ and 250 MPa [109]

Bellowing discusses the effects of nanoparticles on creep resistance. Some data from Li exposure work of NIFS-HEAT-2 are included, such as the data of Li-exposed STD and Li-exposed SAA. Table 6-10 lists the nanoparticle/precipitate conditions and creep rate at 700℃ under 100MPa to indicate the main factors in improving creep resistance in dislocation climbing region. Note that the precipitates in SACWA are difficult to observe due to poor resolution of TEM in the present study. Since the precipitate density in STD is negligible, the values such as volume fraction, volume number density, and size all are set to be 0.

The comparisons of each item of nanoparticle/precipitate conditions and creep rates are listed in Table 6-11 below. Considering the current creep rate of ◇4 ("TiC, 40hr") is mostly increased by the refined grains, the decrease in creep rate caused by nanoparticles in ◇4 is considered to be more effective compared with the other 3 samples with much larger grains. This improvement may be confirmed when largely coarsened grains in ◇4 are obtained in the future. Accordingly, it seems that the volume number density has closer relation with the creep rate, which is, higher volume number density of nanoparticles/precipitates leads to lower creep rate. The value of "$f^{0.5} \cdot d^{-1}$" or "$N_v \cdot d$" does not have remarkable difference for ⟨2⟩ and ⟨3⟩. Considering that the TEM observation may have at most 5nm underestimation with the nanoparticle/precipitate size in average, the contribution of nanoparticles /precipitates is underestimated too much, because the sizes measured range from 5nm to 20nm. So, if the volume number density remains unchanged, another factor that causes the reduce in creep rate is larger nanoparticle/precipitate size. However, the most important factor is to increase the volume number density of the nanoparticles or precipitates for an as-receive V-alloy.

Table 6-10 Nanoparticle/precipitate conditions and creep rate of V-4Cr-4Ti alloys at 700℃ and 100MPa

ID	Material	Volume fraction $((f/\frac{\pi}{6}))^{0.5}$	Particle size (d/m)	Volume number density (N_v/m^3)	$(f^{0.5} \cdot d^{-1})$ / $(\frac{\pi}{6})^{0.5}$	$N_v \cdot d$(/m^2)	Creep rate at 700℃, 100MPa(/s)
⟨1⟩	STD	0	0	0	0	0	1.06×10^{-9}
⟨2⟩	Li-STD	0.070	1×10^{-8}	4.90×10^{21}	7.00×10^{6}	4.90×10^{13}	2.16×10^{-10}
⟨3⟩	Li-SAA	0.135	2×10^{-8}	2.28×10^{21}	6.75×10^{6}	4.56×10^{13}	5.42×10^{-10}
⟨4⟩	"TiC, 40hr"	0.060	5×10^{-9}	2.92×10^{22}	1.21×10^{7}	1.46×10^{14}	3.14×10^{-11}

Table 6-11 Order of nano-particle/precipitate conditions and creep rates of V-4Cr-4Ti alloys at 700℃ and 100MPa

Item	Order
$f^{0.5}$	⟨3⟩ > ⟨2⟩ ≥ ⟨4⟩ > ⟨1⟩
d	⟨3⟩ > ⟨2⟩ > ⟨4⟩ > ⟨1⟩
N_v	⟨4⟩ > ⟨2⟩ > ⟨3⟩ > ⟨1⟩
$f^{0.5} \cdot d^{-1}$	⟨4⟩ > ⟨2⟩ ≥ ⟨3⟩ > ⟨1⟩
$N_v \cdot d$	⟨4⟩ > ⟨2⟩ ≥ ⟨3⟩ > ⟨1⟩
Current creep rate order	⟨1⟩ > ⟨4⟩ > ⟨3⟩ > ⟨2⟩
Expected creep rate order in the future	⟨1⟩ > ⟨3⟩ > ⟨2⟩ > ⟨4⟩

Further, nanoparticles can potentially resist grain boundary sliding. Some previous work [152-155] showed that the nanoparticles can suppress grain boundary sliding through internal stress. In addition, the boundaries can be changed to be isotropic and the slide will be almost in the same rate. In such cases, the most important way to enhance the creep resistance of a metal or alloy, such as "TiC, 40hr", appears to be optimizing nanoparticle dispersion conditions both in interior of grains and on grain boundaries. Therefore, further research on the creep rate of "TiC, 40hr" with coarsened grains by higher temperature annealing should be given the first priority.

6.8 Summary

With TiC, SiC and Ti_3SiC_2 as dispersion particles, WC/Co and Si_3N_4 as milling ball materials, a mechanical alloying (MA) process of particle-dispersion V-4Cr-4Ti alloys with Y addition has been studied with different milling time. The dissolution behavior of alloying elements in V matrix and dissolution effects of milling balls as well as dispersion carbides on alloy hardness are discussed. With understanding of the MA process, a complete MA for V-4Cr-4Ti alloys with Y and carbide additions was obtained. MA strengthening with grain size refining and nanoparticle dispersion strengthening for these alloys was studied. Based on the above study, following conclusions are obtained:

(1) Si_3N_4 balls can be easily ground into V matrix and contaminate the alloy during MA process. Dissolution of Si_3N_4 can cause hardening of vanadium alloy due to the dissolution of Si and N. The mixed Si_3N_4 is also expected to act as a possible matrix of a V/Si_3N_4 composite material which has dramatic hardening. However, the new material will have poor ductility, and the fabrication of V-4Cr-4Ti alloys with Y and carbide additions using Si_3N_4 balls is not recommended.

(2) Ti_3SiC_2 is more stable than TiC and SiC to be decomposed in the present MA. The poor dissolution of Ti_3SiC_2 particles retards the solid solution hardening of vanadium alloy. Higher collision intensity and longer MA time is necessary to dissolve the Ti_3SiC_2 particles more completely.

(3) The dissolution of Y into V matrix is faster than that of Cr, and the dissolution of Cr is faster than that of Ti under the present MA conditions. Therefore, the successful MA process for V-4Cr-4Ti system with Y addition depends on the dissolution of Ti.

(4) For MA with present milling parameters and WC/Co balls, a process time of about 40hrs is necessary for a complete alloying process of V-4Cr-4Ti alloys with Y and TiC additions.

(5) The V-4Cr-4Ti alloys with Y and carbide additions are strengthened with long time MA for up to 40hrs. Grain sizes of these alloys are refined by MA. Large number density of new nanoparticles are produced by MA and the following HIPing processes.

(6) TiN and Y_2O_3 may be the main nanoparticles in V-4Cr-4Ti alloy with Y and carbide additions.

(7) TiN is less thermally stable than Y_2O_3, and the sizes of TiN particles are generally larger than those of Y_2O_3 particles. TiN particles can get coarsened in the annealing at 1200℃ for 1hr, while new Y_2O_3 particles can form in extremely fine size smaller than 10nm.

(8) The formation and effects of TiC, SiC and Ti_3SiC_2 on mechanical properties of the V-4Cr-4Ti alloys via MA are unclear in the present study. However, to control the formation and coarsening of Y_2O_3 particles could be one of good ideas to strengthen V-4Cr-4Ti alloys with Y additions and finally obtain enhanced creep resistance at 100MPa and even higher stresses.

(9) Annealing at 1200℃ for 1hr causes coarsening of the refined grains and formation of larger number density of nanoparticles for vanadium alloys with complete MA. More suitable annealing is further desirable to cause more growth of the grains and to increase the number density of nanoparticles.

(10) The V-4Cr-4Ti alloy with Y and TiC additions under 100MPa has higher creep rate than NIFS-HEAT-2 in STD and SACWA states under 280MPa. However small grain sizes lead to grain boundary sliding in creep deformation.

(11) Large number density of nanoparticles is a major reason in improving the creep resistance of V-4Cr-4Ti-1.5Y-0.3TiC under 100MPa.

Finally, to increase the number density of nanoparticles with coarsened grains could be a guiding principle for strengthening V-4Cr-4Ti alloy via MA. So, in future research on strengthening V-4Cr-4Ti alloy, to obtain nanoparticles with high thermal stability at elevated temperatures should be given the first priority.

CHAPTER 7

Conclusions

The present study seeks to strengthen the V-4Cr-4Ti alloy for application in the Li/V blanket of fusion reactors. Possible strengthening mechanisms include (1) solid-solution hardening, (2) work hardening, (3) precipitation hardening (usually has (1) as the pre-treatment), (4) nanoparticle-dispersion hardening, and (5) grain-size refinement for strengthening metal and alloys. Of these, the present study used two combined mechanisms to strengthen the V-4Cr-4Ti alloy: (1) work hardening followed by precipitation hardening and (2) nanoparticle-dispersion hardening coupled with grain-size refinement. The purpose is to improve creep resistance for the V-4Cr-4Ti alloy. The initial idea is to increase the yield stress to resist dislocation motion. Li exposure is applied to evaluate the effects of mass transfer and thermal aging on the thermal stability of the strengthening agents.

Various treatments for V-4Cr-4Ti alloy have been applied for comparison. Cold rolling was performed to introduce high-density dislocations. Heat treatment was used to achieve the evolution of microstructures, including precipitation formation/coarsening and dislocation annihilation. Room-temperature (RT) and high-temperature (HT) tensile strength as well as thermal creep were evaluated to define the mechanical properties. Chemical analysis was applied to determine the chemical compositions in the alloy matrix and to estimate the solid-solution hardening. TEM observation was performed to determine the precipitate/nanoparticle sizes, precipitate/nanoparticle number densities, dislocation number density, dislocation type, and size of small grains. Surface morphology, element distribution of materials, and large grain sizes were characterized by SEM/EDX. Changes in the V lattice parameter during MA were detected by EDX and XRD.

Based on the above experiments, we have reached the following conclusions:

Thermo-mechanical strengthening

(1) Both SAACW and SACWA can strengthen the V-4Cr-4Ti alloy at RT and HT. The strengthening results from both work hardening and precipitation hardening. Combining the strengthening methods in either order improves yield stress to resist deformation of the alloy. In perspective of the increase in hardness and tensile strength, the order of work hardening and precipitation hardening does not significantly influence strengthening.

(2) The creep of SACWA differs from that of SAACW. SACWA has a higher creep rate than SAACW at stresses below 180MPa, but a lower creep rate than SAACW at stresses above 180MPa. The difference is assumed to be due to different interactions of precipitates with dislocations. The precipitates and dislocations in SAACW are independently distributed. As a result, dislocations are not closely decorated by precipitates, and type a<1 0 0> dislocations seem to disappear during creep. Dislocation glide is assumed to occur above 180MPa. SAACW has the creep mechanism of dislocation climbing only at stresses below 180MPa. In contrast, precipitates in SACWA are assumed to locate on the dislocations. SACWA may re-

tain type a < 1 0 0 > dislocations because of the close decoration of dislocations by precipitates. The decoration is strong enough to overcome the dislocation glide. Accordingly, SACWA keeps dislocation climbing dominated creep mechanism in all stress regions.

(3) STD has a creep mechanism similar to that of SAACW, with most type a < 1 0 0 > dislocations immediately disappearing when creep deformation starts. Thus for STD, dislocation glide is assumed to occur above 180MPa, and dislocation climbing occurs at stresses below 180MPa.

(4) The precipitates and dislocations in SACWA enhance thermal stability for one another. The strong decoration makes dislocation motion more difficult, and dislocations disappear more slowly. Strong decoration also makes the coarsening of precipitates more difficult.

(5) STD and SACWA have better creep resistance at lower and higher stress regions relative to 180MPa, respectively. The criteria for blanket material indicate limiting stresses of 51MPa for STD and 16MPa for SACWA at 700℃ for 100,000hrs at their minimum creep rates. For SAACW, the related maximum stress is 31MPa.

(6) More impurities can cause higher creep resistance by forming more precipitates.

Li exposure.

(7) Li exposure for V-4Cr-4Ti alloys produces mass transfer and thermal aging effects. Mass transfer leads to more precipitate formation, while aging causes precipitate growth and dislocation loss.

(8) Diffusion of C, O, and N is based on their chemical affinity with alloying elements competing with Li. At 650℃, C and N transfer from Li to the V matrix due to stronger affinity with Ti, while O transfers from V matrix due to stronger affinity with Li.

(9) Li exposure strengthens V-4Cr-4Ti alloy. The creep mechanisms do not change in the present study. However, stress exponent, n, decreases with more precipitates formed due to mass transfer. Thus, a possible shift of dislocation climbing mechanism towards higher stress regions is expected for Li-exposed V-4Cr-4Ti alloy.

(10) New precipitates formed due to trapping of impurities in SACWA are also assumed to be distributed along dislocations and to resist the disappearance of dislocations.

Mechanical alloying.

(11) Si_3N_4 can be ground into V powders; thus, Si_3N_4 vessels and balls may not be suitable for milling V-4Cr-4Ti alloy with Y and carbide additions in mechanical alloying.

(12) Using the milling parameter " , , rotation speed of 340rpm, pauses every other minute for cooling" is suitable for fabricating V-4Cr-4Ti alloys with Y and carbide additions using 5mm WC/Co balls in MA.

(13) With the above parameters, 40hrs is enough for complete MA of V-4Cr-4Ti alloys with Y and TiC additions.

(14) In the present MA, the dissolution of Y into V matrix is faster than that of Cr, and the dissolution of Cr into V matrix is faster than that of Ti.

(15) The dissolution rates of SiC and TiC are similar, and faster than that of Ti_3SiC_2 into V matrix.

(16) MA followed by HIPing at 1000℃ can introduce the high number density of TiN and Y_2O_3 nanoparticles in the V-4Cr-4Ti alloy matrix.

(17) Annealing at 1200℃ coarsens TiN nanoparticles and decreases the number density of TiN nanoparticles. However, this annealing leads to new formation of extremely fine Y_2O_3 nanoparticles with high number density. Thus, the Y_2O_3 nanoparticles may have better thermal stability in strengthening V-4Cr-4Ti alloys for high-temperature application in the present alloy systems.

(18) Present MA and HIPing produce small grains some hundreds of nanometers in diameter. Annealing at 1200℃ can cause grain growth. In order to obtain higher creep resistance, it is necessary to coarsen the grains further at higher temperatures. In addition, there should be a suitable balance between grain coarsening with a decrease in the number density of nanoparticles.

(19) High number density of nanoparticles in V-4Cr-4Ti alloy with Y and carbides added via MA is the main reason for improved creep resistance at low stress. Refined grain size is the main reason for degradation in creep resistance for mechanically alloyed V-4Cr-4Ti alloy at high stress.

Those phenomena mostly agree with established theories or experience. Nevertheless, the following new findings are noteworthy:

(a) Work hardening followed by precipitation hardening (SACWA) yields small precipitates along dislocations. This special distribution leads to high stability of both dislocation structure and precipitate size. Indeed, these precipitate-decorated dislocations do not improve creep resistance, but creep strength in high-stress regions has been improved. Mass gain increases strengthening in this mechanism. Therefore, SACWA has strong adaptability in heat and a mass transfer environment. Extension of the low-stress region for SACWA to have an advantage over other strengthening in resisting creep deformation is expected if use more suitable aging.

(b) The remarkable hardening area in a cross-section of V-4Cr-4Ti alloy agrees with the diffusion range of C and especially N, providing visible evidence of mass transfer affecting the mechanical properties of V-4Cr-4Ti alloy. The capability of each impurity to affect the mechanical properties of V-4Cr-4Ti alloy can be clarified. In particular, C-rich, O-rich, or N-rich precipitates can more easily be distinguished using TEM morphology via observation in different diffusion ranges. It is worth noting that the study of direct Li exposure for V-4Cr-4Ti alloy seeks to support the multilayered blanket concept. The strengthening of the alloy foil may not result in a stronger main structure. For a 5mm V-4Cr-4Ti wall, which is the typical design in the blanket structure, complete strengthening by trapping N at 650℃ requires more than 100 years, and that at 700℃ requires more than 40 years. Thus, it is not rational to rely on mass transfer in Li exposure to strengthen V-4Cr-4Ti alloy.

(c) The present study is the first to describe the dissolution order of Y, Cr, and Ti into V matrix in mechanical alloying. To our knowledge, similar phenomena have not been reported in other material systems produced by mechanical alloying. This finding can provide a way for optimizing MA process time. Moreover, the kinetics of nonequilibrium thermodynamics systems like MA is far from mature. The present finding is expected to provide such study with some helpful access. Further research on dissolution in the V matrix is expected to help clarify collision-induced diffusion in solids.

References

[1] William S. Humphrey and Joe Stanislaw, Economic growth and energy consumption in the UK, 1700 – 1975, Energy Policy 7 (1979) 29 – 42.

[2] Putnam, "Energy in the Future", 1953; J. Laherrere, "Peak Oil and other Peaks", CERN 2005.

[3] http://www.eia.gov/

[4] Assembled from data published on the The World Bank website.

[5] BP – Statistical Review 2008.

[6] H. Schaefer, Der Kumulierte Energie und Massenaufwand von Kraftwerken, Mu¨nchen, 1994. Energie und Massenaufwand.

[7] H. Katheder et al., Plant Layout and Design, SEAFP/RM11/(95).

[8] Yu. D. Baranaev, V. V. Dolgov, Yu. A. Sergeev, Activities in the field of small nuclear power reactors, Nuclear Engineering and Design 173 (1997) 159 – 166.

[9] W. F. Vogelsang, H. Y. Khater, The impact of D – ^{3}He fusion reactors on waste disposal. Fusion Engineering and Design 5 (1988) 367 – 377

[10] Jorma V. Sandberg, On the feasibility of multicomponent activation detectors for fusion reactor neutronics measurements. Nuclear Instruments and Methods 206 (1983) 227 – 234.,

[11] Dan Finkenthal, Rick lee, Steve Rodecker, John Ray, Dave Schissel, Pete Taylor, Fusion-Nature's Fundamental Energy Source, General Atomics, 1996.

[12] B. M. Oliver, Harry Farrar, M. M. Bretscher, Tritium half – life measured by helium – 3 growth, Appl. Radial. Isot. Vol. 38, No. 11, pp. 959 – 965, 1987.

[13] D. Fasel, M. Q. Tran, Availability of lithium in the context of future D – T fusion reactors, Fusion Engineering and Design 75 – 79 (2005) 1163 – 1168.

[14] Budzanowski, A. et al, Experimental study of the $p + {}^6\mathrm{Li} \rightarrow \eta + {}^7\mathrm{Be}$ reaction 11.3 MeV above threshold, Physical Review C, vol. 82, Issue 4, id. 041001.

[15] H. E. Rafelski, et al. Muon reactivation in muon – catalyzed D – T fusion, Progress in Particle and Nuclear Physics, 22 (1989) 279 – 338.

[16] M. Gasparotto, Present Status of Fusion Research: the Next Step Tokamak (ITER) and the Demonstration Reactor (DEMO), Appl. Radiat. lsot. Vol. 46, No. 6/7, pp. 531 – 536, 1995.

[17] D. J. Ward, The contribution of fusion to sustainable development, Fusion Engineering and Design 82 (2007) 528 – 533.

[18] H. – W. Bartels, et al. ITER reference accidents, Fusion Engineering and Design 42 (1998) 13 – 19.

[19] Y. Shimomura, ITER towards the construction, Fusion Engineering and Design 74 (2005) 9 – 16.

[20] Satoshi Konishi, et al. DEMO plant design beyond ITER, Fusion Engineering and Design 63 – 64 (2002) 11 – 17.

[21] O. Motojima, New Status of ITER, 26th Symposium on Fusion Technology, Porto, 28 September 2010.

[22] John Poole, Safety at ITER, JP Scientific (Nantwich) Ltd, June 2011.

[23] Charles C. Baker, Robert W. Conn, Farrokh Najmabadi, Mark S. Tillack, Status and prospects for fusion energy from magnetically confined plasmas, 23 (7/8) 1998 649 –694.

[24] A Iiyoshi, S Imagawa, LHD group, Design, construction and the first plasma experiments in the Large Helical Device, Fusion Engineering and Design 46 (1999) 323 –335.

[25] A. Sagara, Conceptual design activities and key issues on HD – type reactor FFHR, Fusion Engineering and Design, 81 (2006) 2703 –2712.

[26] Demonstration Fusion Reactors. Fusion for Energy. European Joint Undertaking for ITER and the Development of Fusion Energy.

[27] R. Bünde, The potential net energy gain from DT fusion power plants, Nuclear Engineering and Design. Fusion, 3 (1985) 1 –36

[28] Satoshi Konishi, et al. DEMO plant design beyond ITER, Fusion Engineering and Design 63 –64 (2002) 11 –17.

[29] K. Ehrlich, International strategy for fusion materials development, Journal of Nuclear Materials. 283 –287 (2000) 79 –88.

[30] Y. Kohzaki et al. Engineering aspects of fusion engineering test facility based on mirror confinement (FEF), Fusion Engineering and Design, 8 –10 (1989) 27 –32

[31] J. A. Maniscalco, D. H. Berwald, The material implications of design and system studies for inertial confinement fusion systems, Journal of Nuclear Materials, 85 –86 (1979) 37 –46.

[32] S. Nakai a and H. Nakashima, Nuclear aspects and design of an inertial confinement fusion reactor, Fusion Engineering and Design 16 (1991) 173 –182.

[33] Edward I. Moses, Advances in inertial confinement fusion at the National Ignition Facility (NIF), Fusion Engineering and Design, 85 (2010) 983 –986.

[34] S. J Zinkle, N. M Ghoniem, Operating temperature windows for fusion reactor structural materials, Fusion Engineering and Design 51 –52 (2000) 55 –71.

[35] Karl Ehrlich, Materials research towards a fusion reactor, Fusion Engineering and Design 56 –57 (2001) 71 –82.

[36] B. van der Schaaf, Structural materials requirements for in – vessel components of fusion power plants, Fusion Engineering and Design 51 –52 (2000) 43 –54.

[37] T. Muroga, T. Nagasaka, Overview of NIFS program for vanadium alloy development, July, 2009.

[38] M. L Grossbeck et al, Analysis of V – Cr – Ti alloys in terms of activation of impurities, Journal of Nuclear Materials 258 –263 (1998) 1778 –1783.

[39] S. J. Piet, E. T. Cheng, L. J. Porter, Fus. Technol. 17 (1990) 636.

[40] D. R. Harries, G. J. Butterworth, A. Hishinuma, F. W. Wiffen, Evaluation of reduced – activation options for fusion materials development, Journal of Nuclear Materials 191 –194 (1992) 92.

[41] E. E. Bloom et al. Materials to deliver the promise of fusion power – progress and challenges, Journal of Nuclear Materials 329 –333 (2004) 12 –19.

[42] Karl Ehrlich, E. E. Bloom, T. Kondo, International strategy for fusion materials development, Journal of Nuclear Materials 283 –287 (2000) 79 –88.

[43] R. F. Mattas et al. Results of R&D for lithium:vanadium breeding blanket design, Fusion Engineering and Design 39 –40 (1998) 659 –668.

[44] I. R. Kirillov, RF DEMO team, Lithium cooled blanket of RF DEMO reactor, Fusion Engineering and Design 49 – 50 (2000) 457 – 465.

[45] Y. Gohar, S. Majumdar, D. Smith, Y. Gohar, S. Majumdar, D. Smith, Fusion Engineering and Design 49 – 50 (2000) 551 – 558.

[46] S. Mori, S. Yamazaki, J. Adachi T. Kobayashi, Blanket and divertor design for the Steady State Tokamak Reactor (SSTR), Fusion Engineering and Design 18 (1991) 249 – 258.

[47] T. Tanaka, Design studies on three – dimensional issues for liquid blanket systems in helical reactor FFHR, Fusion Engineering and Design (in press).

[48] A. Sagara et al, Materials design and related R&D issues for the force – free helical reactor (FFHR), Journal of Nuclear Materials 258 – 263 (1998) 2079 – 2082.

[49] S. Nishio, et al. Prototype tokamak fusion reactor based on SiC/SiC composite material focusing on easy maintenance, Fusion Engineering and Design 48 (2000) 271 – 279.

[50] Farrokh Najmabadi et al, Overview of the ARIES – RS reversed – shear tokamak power plant study, Fusion Engineering and Design 38 (1997) 3 – 25.

[51] A. R. Raffray et al, High performance blanket for ARIES – AT power plant, Fusion Engineering and Design 58 – 59 (2001) 549 – 553.

[52] A. R. Raffray et al. Breeding blanket concepts for fusion and materials requirements. Journal of Nuclear Materials 307 – 311 (2002) 21 – 30.

[53] K. Ehrlich et al. International strategy for fusion materials development. Journal of Nuclear Materials 283 – 287 (2000) 79 – 88.

[54] R. L. Klueh , M. A. Sokolov, Mechanical properties of irradiated 9Cr – 2WVTa steelwith and without nickel, Journal of Nuclear Materials 367 – 370 (2007) 102 – 106.

[55] B. van der Schaaf et al, The development of EUROFER reduced activation steel, Fusion Engineering and Design 69 (2003) 197 – /203.

[56] R. Sch aublin, P. Sp atig, M. Victoria, Microstructure assessment of the low activation ferritic/martensitic steel F82H, Journal of Nuclear Materials 258 – 263 (1998) 1178 – 1182.

[57] A. Kohyama, Production of low activation steel; JLF – 1, large heats – Current status and future plan, Journal of Nuclear Materials 258 – 263 (1998) 1319 – 1323.

[58] Q. Huang, C. Li, Y. Li et al, Progress in development of China Low Activation Martensitic steel for fusion application, Journal of Nuclear Materials 367 – 370 (2007) 142 – 146.

[59] J. M. Chen et al, Materials development for ITER shielding and test blanket in China, Journal of Nuclear Materials 417 (2011) 81 – 84.

[60] A. Kimura et al, Ferritic steel – blanket systems integration R&D—Compatibility assessment, Fusion Engineering and Design 81 (2006) 909 – 916.

[61] N. Yamamoto, Y. Murase, J. Nagakawa, An evaluation of helium embrittlement resistance of reduced activation martensitic steels, Fusion Engineering and Design 81 (2006) 1085 – 1090.

[62] M. Kikuchi et al, Blanket – plasma interaction in tokamaks Implication from JT – 60U, JFT – 2M and reactor studies, Fusion Engineering and Design 81 (2006) 1589 – 1598.

[63] P. Fenici, A. J. Frias Rebolo, R. H. Jones, A. Kohyama, L. L. Snead, Journal of Nuclear Materials 258 – 263 (1998) 215.

[64] F. J. Perez et al, Chemical compatibility of SiC composite structures with fusion reactor helium coolant at

high temperatures, Fusion Engineering and Design 22 (1993) 415 –426.

[65] R. H. Jones, C. H. Henager, Jr., Fusion reactor application issues for low activation SiC/SiC composites, Journal of Nuclear Materials 219 (1995) 55 –62.

[66] M. Tamura, H. Hayakawa, A. Yoshitake, A. Hishinuma and T. Kondo, Development of potential low activation ferritic and austenitic steels, Journal of Nuclear Materials 141 –143 (1986) 1067.

[67] T Muroga, T Nagasaka, A Iiyoshi, A Kawabata, S Sakurai, M Sakata, NIFS program for large ingot production of a V –Cr –Ti alloy, Journal of Nuclear Materials, 283 –287, (2000) 711 –715.

[68] Shigeru Tanaka, R Matera, G Kalinin, V Barabash, K Mohri, ITER Materials R&D Data Bank, Journal of Nuclear Materials, 271 –272, (1999) 478 –485.

[69] G. J. Butterworth, Fus. Technol. 21 (1992) 1994.

[70] D. L Smith, J Konys, T Muroga, V Evitkhin., Development of coatings for fusion power applications, Journal of Nuclear Materials, 307 –311 (2002) 1314 –1322.

[71] D. N. Braski, The effect of neutron irradiation on vanadium alloys, Journal of Nuclear Materials 141 –143 (1986) 1125 –1131.

[72] L. A. El –Guebaly, Potential coatings for Li/V system: Nuclear performance and design issues Fusion Engineering and Design 81 (2006) 1327 –1331.

[73] R. J. Kurtz et al. Recent progress on development of vanadium alloys for fusion, Journal of Nuclear Materials 329 –333 (2004) 47 –55.

[74] B. A. Loomis, D. L. Smith, F. A. Garner, Swelling of neutron –irradiated vanadium alloys, Journal of Nuclear Materials 179 –181 (1991) 771 –774.

[75] T. L. Hughes, International Metals Reviews, 25 (1980) 163 –222.

[76] H. M. Chung, B. A. Loomis, D. L. Smith, Development and testing of vanadium alloys for fusion applications, Journal of Nuclear Materials 239 (1996) 139 –156.

[77] D. L. Smith, Progress in vanadium alloy development for fusion applications, Fusion Engineering and Design, 41 (1998) 7 –14.

[78] B. A. Loomis, Effects of neutron irradiation and hydrogen on DBTT of V –Cr –Ti alloys, Sixth International Conference on Fusion Reactor Materials, 1993.

[79] K Sakai et al, Mechanical properties and microstructures of high –chromium V –Cr –Ti type alloys, Journal of Nuclear Materials, 329 –333 (2004) 457 –461.

[80] M. M. Potapenko et al, Manufacture of semifinished items of alloys V –4Ti –4Cr and V – 10Ti –5Cr for use as a structural material in fusion applications, Journal of Nuclear Materials 233 237 (1996) 438 –441.

[81] H. Y. Fu, J. M. Chen, P. F. Zheng, T. Nagasaka, T. Muroga, Fabrication using Electron Beam Melting of a V –4Cr –4Ti Alloy and Its Heat Treatment Study, Journal of Nuclear Materials , (these proceedings).

[82] Vincent Duquesnes, Thomas Guilbert, Marion Le Flem, French investigation of a new V –4Cr –4Ti grade: CEA –J57 – Fabrication and microstructure, Journal of Nuclear Materials, 426 (2012) 96 –101.

[83] M. L. Grossbeck et al, Analysis of V –Cr –Ti alloys in terms of activation of impurities, Journal of Nuclear Materials 258 –263 (1998) 1778 –1783.

[84] W. R. Johnson, J. P. Smith, Fabrication of a 1200 kg ingot of V –4Cr –4Ti alloy for the DIII –D radiative divertor program, Journal of Nuclear Materials 258 –263 (1998) 1425 –1430.

[85] T. Muroga et al, Vanadium alloys – overview and recent results, Journal of Nuclear Materials 307 –311 (2002) 547 –554.

[86] J. M. Chen, T. Muroga, T. Nagasaka, Y. Xu, C. Li, S. Y. Qiu, Y. Chen, Precipitation behavior in V－6W－4Ti, V－4Ti and V－4Cr－4Ti alloys, Journal of Nuclear Materials 334 (2004) 159－165.

[87] A. Kimura, R. Kasada et al, Development of Al added high－Cr ODS steels for fuel cladding of next generation nuclear systems, Journal of Nuclear Materials 417 (2011) 176－179.

[88] Ceri A. Williams et al, Nanoscale characterisation of ODS－Eurofer 97 steel: An atom－probe tomography study, Journal of Nuclear Materials, 400 (2010) 37－45.

[89] A. A. Nikitina, V. S. Ageev, A. P. Chukanov, V. V. Tsvelev, N. P. Porezanov, O. A. Kruglov, R&D of ferritic－martensitic steel EP450 ODS for fuel pin claddings of prospective fast reactors, Journal of Nuclear Materials, 428 (2012) 117－124.

[90] R. Schäublin, A. Ramar, N. Baluc, V. de Castro, M. A. Monge, T. Leguey, N. Schmid, C. Bonjour, Microstructural development under irradiation in European ODS ferritic/martensitic steels, Journal of Nuclear Materials, 351 (2006) 247－260.

[91] Z. Oksiuta, P. Olier, Y. de Carlan, N. Baluc, Development and characterisation of a new ODS ferritic steel for fusion reactor application, Journal of Nuclear Materials, 393 (2009) 114－119.

[92] Y. de Carlan et al, CEA developments of new ferritic ODS alloys for nuclear applications, Journal of Nuclear Materials, 386－388 (2009) 430－432.

[93] L. Toualbi et al, Assessment of a new fabrication route for Fe－9Cr－1W ODS cladding tubes, Journal of Nuclear Materials, 428 (2012) 47－53.

[94] S. Ohtsuka et al, Nano－mesoscopic structural characterization of 9Cr－ODS martensitic steel for improving creep strength, Journal of Nuclear Materials, 367－370 (2007) 160－165.

[95] N. Baluc et al, Review on the EFDA work programme on nano－structured ODS RAF steels, Journal of Nuclear Materials, 417 (2011) 149－153.

[96] Volker Piotter et al, Development of a powder metallurgy process for tungsten components, Fusion Engineering and Design, 83 (2008) 1517－1520.

[97] Y Ishijima et al, Current status of ductile tungsten alloy development by mechanical alloying, Journal of Nuclear Materials, 329－333 (2004) 775－779.

[98] H. Kurishita, T. Kuwabara, M. Hasegawa, Development of ultra－fine grained V－W－Y alloys with superior mechanical properties by effective usage of WC debris introduced during mechanical alloying, Materials Science and Engineering A 432 (2006) 245－252.

[99] T. Kuwabara, H. Kurishita, M. Hasegawa, Development of an ultra－fine grained V－1.7 mass% Y alloy dispersed with yttrium compounds having superior ductility and high strength, Materials Science and Engineering A 417 (2006) 16－23.

[100] H. Kurishita, T. Kuwabara, M. Hasegawa, Development of fine－grained V－28Cr－2.3Y and V－52Cr－1.8Y alloys with superior mechanical properties, Materials Science and Engineering A 433 (2006) 32－38.

[101] H. Kurishita, Effect of 2 wt% Ti addition on high－temperature strength of fine－grained, particle dispersed V－Y alloys, Journal of Nuclear Materials 367－370 (2007) 848－852.

[102] T. Furuno, H. Kurishita, T. Nagasaka, A. Nishimura, T. Muroga, T. Sakamoto, S. Kobayashi, K. Nakai, S. Matsuo, H. Arakawa, Effects of grain size on high temperature creep of fine grained, solution and dispersion hardened V－1.6Y－8W－0.8TiC, Journal of Nuclear Materials 417 (2011) 299－302.

[103] T. Sakamoto, High temperature deformation of V－1.6Y－8.5W－(0.08, 0.15)C alloys, Journal of Nu-

clear Materials 386 – 388 (2009) 602 – 605.

[104] S. Oda, High temperature strength of fine – grained particle – dispersed V – (1.7 – 2.4) wt% Y alloys with different grain sizes and particle densities, Journal of Nuclear Materials, 329 – 333 (2004) 462 – 466.

[105] H. Kurishita, Intrinsic martensite formation in neutron irradiated V – 1.6% Y alloys with fine – grained structure of highly pure matrix, Journal of Nuclear Materials 358 (2006) 217 – 226.

[106] Kiyomichi Nakai et al, Mechanical alloying process of vanadium powder with 1.7 wt. % Y addition, Journal of Nuclear Materials 386 – 388 (2009) 587 – 590.

[107] H. Kurishita, T. Kuwabara, Microstructural control to improve the resistance to radiation embrittlement in vanadium, Journal of Nuclear Materials 343 (2005) 318 – 324.

[108] T. Kuwabara, Microstructure control to improve mechanical properties of vanadium alloys for fusion applications, Journal of Nuclear Materials 283 – 287 (2000) 611 – 615.

[109] T. Sakamoto et al, Uniaxial creep behavior of nanostructured, solution and dispersion hardened V – 1.4Y – 7W – 9Mo – 0.7TiC with different grain sizes, Materials Science and Engineering: A, 528 (2011) 7843 – 7850.

[110] T. Muroga, Overview of the TITAN project, Fusion Engineering and Design, (in press).

[111] D.K. Sze, M.C. Billone, T.Q. Hua, M. Tillack, F. Najmabadi, X. Wang et al. The ARIES – RS fusion power core – recent development in Li/V design, Fusion Engineering and Design, 41 (1998) 371.

[112] S. Malang, M.S. Tillack (Eds.), Development of Self – Cooled Liquid Metal Blankets, FZK report, FZKA 558, 1995.

[113] M.S. Tillack et al, Configuration and engineering design of the ARIES – RS tokamak power plant, Fusion Engineering and Design 38 (1997) 87 – 113.

[114] A. Sagara, Optimization activities on design studies of LHD – type reactor FFHR, Fusion Engineering and Design, 83 (2008) 1690 – 1695.

[115] B. A. Pint, Operation of a V – 4Cr – 4Ti thermal convection loop with Li at 700°C, Volume 42, Semiannual Progress Report, Oka Ridge, June 30, 2007.

[116] S.N. Votinov, Prospects and problems using vanadium alloys as a structural material of the first wall and blanket of fusion reactors, Journal of Nuclear Materials 233 – 237 (1996) 370 – 375.

[117] D.L. Smith, T. Muroga, J. Konys, V. Evtikhin, Development of coatings for fusion power applications, Journal of Nuclear Materials 307 – 311 (2007) 1314 – 1322.

[118] H.U. Borgstedt, G. Drechsler, G. Frees, Z. Peric, A vanadium alloy for the application in a liquid metal blanket of a fusion reactor, Journal of Nuclear Materials. 155 – 157 (1988) 690 – 693.

[119] B.A. Pint, J.L. Moser, A. Jankowski, J. Hayes, Compatibility of multi – layer, electrically insulating coatings for vanadium – lithium blankets, Journal of Nuclear Materials, 367 – 370 (2007) 1165 – 1169.

[120] T. Terai, T. Yoneoka, H. Tanaka, A. Suzuki, S. Tanaka, M. Nakamichi, H. Kawamura, K. Miyajima, Y. Harada, Compatibility of yttria (Y_2O_3) with liquid lithium, J. Nucl. Mater. 233 – 237 (1996) 1421.

[121] B.A. Pint, J.L. Moser, P.F. Tortorelli, Liquid metal compatibility issues for test blanket modules, Fusion Engineering and Design 8 – 14 (2006) 901 – 908.

[122] R.F. Mattas et al, EVOLVE—an advanced first wall/blanket system, Fusion Engineering and Design 49 – 50 (2000) 613 – 620.

[123] A. Sagara et al, Design and development of the Flibe blanket for helical – type fusion reactor FFHR, Fusion Engineering and Design 49 – 50 (2000) 661 – 666.

[124] Satoshi FUKADA, A design for recovery of tritium from Flibe loop in FFHR – 2, Fusion Power Plants and Related Advanced Technologies, Feb. 5, 2007.

[125] T. Nagasaka, T. Murogaa, M. M. Li et al, Tensile property of low activation vanadium alloy after liquid lithium exposure, Fusion Engineering and Design 81 (2006) 307 – 313.

[126] M. M. Li, T. Nagasaka et al, Biaxial thermal creep of two heats of V4Cr4Ti at 700 and 800 °C in a liquid lithium environment, Journal of Nuclear Materials 367 – 370 (2007) 788 – 793.

[127] M. M. Li, D. T. Hoelzer, M. L. Grossbeck, The Influence of lithium environment on tensile behavior and microstructure of V – 4Cr – 4Ti, Journal of Nuclear Materials 392 (2009) 364 – 370.

[128] Maity, S. K.; Ballal, N. B.; Kawalla, R., Ironmaking & Steelmaking, 34 (2007) 332 – 342.

[129] T. Muroga and T. Nagasaka, Development of Manufacturing echnology for High Purity Low Activation Vanadium Alloys. Research report // National Institute for Fusion Science Volume 646, Research report NIFS series.

[130] P. F. Zheng, T. Nagasaka, T. Muroga et al, Creep properties of V – 4Cr – 4Ti strengthened by cold working and aging, Fusion Engineering and Design 86 (2011) 2561 – 2564.

[131] J. M. Chen, T. Nagasaka, T. Muroga, et al., Mechanical properties of V – 4Cr – 4Ti strengthened by precipitation and cold rolling, Journal of Nuclear Materials 374 (2008) 298 – 303.

[132] W Decker, J. R Groza, J. C Gibeling, Creep properties of an extruded copper – 8% chromium – 4% niobium alloy, Materials Science and Engineering: A 369 (2004) 101 – 111.

[133] K. Natesan, W. K. Soppet, A. Purohit, Uniaxial creep behavior of V – 4Cr – 4Ti alloy, J. Nucl. Mater. 307 – 311 (2002) 585 – 590.

[134] D. L. Harrod and R. E. Gold, Mechanical properties of vanadium and vanadium – base alloys, Int. Met. Rev. 4 (1980) 163 – 221.

[135] Binary Alloy Phase Diagrams

[136] N. J. Heo, T. Nagasaka, T. Muroga and H. Matsui, Effect of impurity levels on precipitation behavior in the low – activation V – 4Cr – 4Ti alloys, Journal of Nuclear Materials 307 – 311 (2002) 620 – 624.

[137] T. Muroga, T. Nagasaka, P. F. Zheng. Y. F. Li and H. Watanabe, Dislocation evolution during thermal creep deformation in V – 4Cr – 4Ti with various thermal and mechanical reatments, ICFRM proceeding

[138] F. R. Larson and J. Miller, Trans, ASTM, 74(1952) 765

[139] B. A. Pint, K. L. More, H. M. Meyer, J. R. DiStefano, Recent progress addressing compatibility issues relevant to fusion environment, Fusion Sci. Technol. 47 (2005) 851 – 855.

[140] Y. Gohar, D. L. Smith, Multiplier, moderator, and reflector materials for advanced lithium – vanadium fusion blankets, Journal of Nuclear Materials 283 – 287 (2000) 1370 – 374.

[141] V. Tsisar, M. Kondo, Q. Xu, T. Muroga, T. Nagasaka, O. Yeliseyeva, Effect of nitrogen on the corrosion behavior of RAFM JLF – 1 steel in lithium, Journal of Nuclear Materials, 417 (2011), 1205 – 1209

[142] Paul G. Shewmon, Diffusion in solids, 1963, McGraw – Hill.

[143] E. A Brandes, G. B Brook. Smithels Metals Reference Book (Edition 7), 1998 Elsevier, Linacre House, Jordan Hill, Oxford OX2 8DP.

[144] Gerhard Neumann, Cornelis Tuijn. Self – diffusion and impurity diffusion in pure metals: Handbook of experimental data, Pergamon Materials Series 14. 2009, Elsevier, Linacre House, Jordan Hill, Oxford OX2 8DP.

[145] C. Suryanarayana, Mechanical alloying and milling, Progress in Materials Science 46 (2001) 1 – 184

[146] Hall, E. O. The deformation and ageing of mild steel: III Discussion of results. Proc. Phys. Soc. Lond. B 64, 747 -753 (1951).

[147] Petch, N. J. The cleavage of polycrystals. J. Iron Steel Inst. 174, 25 -28 (1953).

[148] Suryanarayana (Discussion via private email)

[149] S. J. Zinkle, G. E. Lucas, deformation and fracture mechanisms in irradiated fcc and bcc metals, Volume 34, Semiannual Progress Report, Oka Ridge, June 30, 2003, pp 101 -125.

[150] T. G. Nieh, J. Wadwirth, O. D. Sherby, Superplasticity in Metals and Ceramics, Cambridge University Press, 1997, p. 40.

[151] Barrett C R, Lytton J K, Sherby O D. Effect of grain size and annealing treatment on steady state creep of copper. Trans. AIME, 1967, 239 (1): 170 -186.

[152] R. Raj and M. F. Ashby, Grain boundary sliding, and the effects of particles on its rate, Metallurgical and Materials Transactions B, 3 (1972) 1937 -1942.

[153] T. Mori, M. Koda, R. Monzen, Particle blocking in grain boundary sliding and associated internal friction, Acta Metallurgica, 31 (1983) 275 -283.

[154] J. S. Zhang, P. E. Li, W. X. Chen and J. Z. Jin, Grain boundary precipitation strengthening in high temperature creep of Fe -15Cr -25Ni alloys, Scripta Metallurgica. 23 (1989) 547 -551.

[155] J. S. ZHANG, P. E. Li and J. Z. JIN, Combined matrix/boundary precipitation strengthening in creep of Fe -15Cr -25Ni alloys. Acta metall, mater. 39 (1991) 3063 -3070.

List of published papers

1. P. F. Zheng, T. Nagasaka, T. Muroga, J. M. Chen, Y. F. Li, Creep properties of V - 4Cr - 4Ti strengthened by cold working and aging, Fusion Engineering and Design. 86 (2011) 2561 - 2564

2. P. F. Zheng, T. Nagasaka, T. Muroga, M. Kondo, J. M. Chen, Mechanical properties of V - 4Cr - 4Ti after exposure in static lithium at 650℃. Plasma and Fusion Research Special Issue. 6, (2011) 2405121.

3. P. F. Zheng, T. Nagasaka, T. Muroga, J. M. Chen, Investigation on mechanical alloying process for vanadium alloys. (under review in Journal of Nuclear Materials)

List of presentations

1. AESJ 2010 Annual Meeting. September 15 – 17, 2010, Sapporo, Japan.
2. 26th Symposium on Fusion Technology (SOFT2010), September 27 – October 1, 2010. Porto, Portugal.
3. Tenth Japan – China Symposium (JCS – 10) on Materials for Advanced Energy Systems and Fission & Fusion Engineering, October 19 – 22, 2010, Kyoto, Japan.
4. 20th International Toki Conference (ITC – 20), December 7 – 10, 2010, Toki, Japan.
5. 15th International Conference on Fusion Reactor Materials (ICFRM – 15), October 16 – 22, 2011, Charleston, USA.
6. AESJ 2012 Annual Meeting. March 19 – 22, 2012, Fukui, Japan.
7. Eleventh China – Japan Symposium (CJS – 11) on Materials for Advanced Energy Systems and Fission & Fusion Engineering, September 11 – 14, 2012, Chengdu, Sichuan, China.

Acknowledgments

This study has been administrated by the Graduate University for Advanced Studies (SOKENDAI) and implemented at the National Institute for Fusion Science (NIFS). The author thanks those who have supported the budget for the research project, provided research guidelines, assisted in experiments, and supported the accomplishment of this study with help in any form.

Profs. Takuya Nagasaka and Takeo Muroga are the author's supervisors. They have provided much assistance in this study by sharing scientific ideas, teaching experiment and analysis techniques, arranging cooperation with outside institutions, guiding the preparation of this thesis, and supervising the research work. The author thanks them for all they have done to help complete this study.

Prof. Jiming Chen at the Southwestern Institute of Physics (SWIP) has also provided much assistance and advice, and his previous study supplied convincing reference data to this study. The author thanks him for his contributions. The author is also grateful to Prof. Akio Sagara at NIFS for fruitful discussions and helpful comments.

This study received support from the JSPS – CAS Core University Program, YUKWAI, and NIFS budget (Code: NIFS GGFF001).

The author thanks Dr. Kondo at NIFS (now at Tokai University) and Dr. Tsisar at the Physical – Mechanical Institute of National Academy of Sciences of Ukraine for their help in lithium – exposure experiments.

Experiments in this study were carried out at a wide range of institutions, and various help from related companies has been received. The author is grateful to Prof. Hideo Watanabe at Kyushu University for his assistance in TEM observation and Prof. Ken – ichi Fukumoto at Fukui University for his fruitful discussion on the design of lithium – related devices. Thanks to TYK Corporation for their help in lithium disposal.

Dr. Iikubo at Daido Steel Co., Ltd., helped with the chemical analyses. Mr. Kitami and Mr. Sato at S. F. C. Co., and Mr. Izuta at H. M. Co. helped with electron – beam welding and fabrication of related devices. Mr. Kagawa at Metal Technology Co. , Ltd. , helped with HIPing. Mr. Kuroki at Miyakojima Seisakusyo Co. , Ltd. , helped machine test samples. Ms. Hamaguchi at Fritsch Japan Co. , Ltd. , supplied helpful information for solving technical problems. Many others who provided help or service are also appreciated.

The author is thankful to Dr. Yanfen Li, Dr. Takashi Watanabe, and Mr. Takeshi Miyazawa at SOKEDAI for assistance in this study. Other colleagues and friends who shared happy time with the author are also included in this acknowledgement.

Last, the most gratitude is bestowed on my family for their love and encouragement. Faith that my family supports my aspirations compels me to move forward.